Chair of Materials Physics

Master's Thesis

Effects of alloying and fluxing treatment on thermal, magnetic and structural properties of Fe-(Ni,Co)-P-C metallic glass ribbons

Eray Yüce

September 2019

EIDESSTATTLICHE ERKLÄRUNG

Ich erkläre an Eides statt, dass ich diese Arbeit selbständig verfasst, andere als die angegebenen Quellen und Hilfsmittel nicht benutzt, und mich auch sonst keiner unerlaubten Hilfsmittel bedient habe.

Ich erkläre, dass ich die Richtlinien des Senats der Montanuniversität Leoben zu "Gute wissenschaftliche Praxis" gelesen, verstanden und befolgt habe.

Weiters erkläre ich, dass die elektronische und gedruckte Version der eingereichten wissenschaftlichen Abschlussarbeit formal und inhaltlich identisch sind.

Datum 25.09.2019

Unterschrift Verfasser/in
Eray, Yüce
Matrikelnummer: 01135575

Affidavit

I declare in lieu of oath, that I wrote this thesis and performed the associated research myself using only literature cited in this volume.

Leoben, September 2019 Eray Yüce

Acknowledgements

Foremost, I would like to express my deepest gratitude and regards to my supervisor Prof. Jürgen Eckert, head of the Erich-Schmid-Institute of materials science, for giving me the opportunity to write my master thesis at his group and for his strong support during the whole course of this study.

I would like to express my sincerest appreciation and regards to Dr. Baran Sarac, whose unique vision and genuine directions assisted me utmost throughout my thesis.

I am also highly obliged to Dr. Parthiban Ramasamy, Dr. Sergey Ketov, Dr. Florian Spiekermann, and all other staff at Erich-Schmid-Institute Leoben.

Special thanks to my family and friends for their love and support.

Abstract

This study focusses on cost-effective and high-throughput production of ferromagnetic $Fe_{80}P_{13}C_7$ iron based metallic glass ribbons and their alloys with cobalt and nickel. Starting from the basic composition of $Fe_{80}P_{13}C_7$ amorphous ribbon, an alloy series of $Fe_{(80-x-y)}Ni_xCo_yP_{13}C_7$ (x = 0, 5, 10, 15, 20 at.%, y = 0, 5, 10, 15, 20 at.%, x + y = 20 or 0) has been synthesized, using the melt spinning technique of rapid solidification processing. Using the fixed number of metalloids of $P_{13}C_7$, three novel alloys, namely, $Fe_{60}Ni_{10}Co_{10}P_{13}C_7$, $Fe_{60}Ni_{15}Co_5P_{13}C_7$ and $Fe_{60}Co_{15}P_{13}C_7$ have been amorphized for the first time. In the preparation of the alloy ingots, only commercial raw materials have been used, and all the melt-spun ribbons were produced under low vacuum conditions and high purity argon atmosphere. All of the investigated alloys were subjected to fluxing purification process, in order to observe the possible effects of the fluxing treatment on glass forming ability, crystallization behavior and thermal properties of the melt-spun glassy ribbons. Nine selected samples from synthesized ribbons (including three fluxed ribbons) were further investigated for their glass forming abilities, thermal and magnetic properties. The as-spun ribbons were subjected to non-isothermal annealing at different temperatures according to their crystallization behavior. The annealed samples were investigated via X-ray diffraction, and the findings were interpreted together with their differential scanning calorimetry results. The room temperature magnetic polarization values of the as-spun samples were ascertained with a physical property measurement system (PPMS), operating in vibrating sample magnetometer mode.

Contents

1. Theoretical Background of Metallic Glasses

1.1 Metallic glasses

Glass is generally considered as a transparent, hard and brittle material, which is used very commonly in everyday life for windows, bottles, electronics etc. Common glass is mostly made up from silica (SiO_2) and other oxides of metals like Al, Ca, Mg, K, Na etc. The molten mixture of silica and the metal oxides is rapidly cooled down to lower temperatures, in order to prevent the crystallization. During this fast transition from liquid to solid state, the atoms cannot find enough time to rearrange themselves into their energetically ideal periodic three-dimensional positions, in other words, they do not form a crystal [2, 3]. For this reason, this frozen-like random atomic structure of a glass can be considered as a ''Super-cooled Liquid'', hence it possesses the same composition and randomness of atoms as its liquid state [1, 25]. Technically, the glass is referred to as non-crystalline material, which lacks the long-range periodicity and translational symmetry, having a random arrangement of its constituent atoms [1].

In nature, metals and alloys are traditionally considered crystalline. That is, their atoms are arranged in a regular and periodic manner in three dimensions [1]. Metallic glasses are quite the opposite. By definition, "Metallic glass" is an amorphous (glassy, non-crystalline) metallic alloy, an advanced material, which is processed through a non-equilibrium processing technique (i.e. rapid solidification, mechanical alloying, plasma processing, spray forming, laser processing and vapor deposition methods) [1, 23]. Among these techniques, rapid solidification (continuous cooling from the liquid state) is the most widely used one, just like the case in traditional silicate or oxide glasses. In this work, the term of metallic glass refers to a rapidly solidified alloy.

The first metallic glass was produced by Pol Duwez [24] in 1960 at the California Institute of Technology, Pasadena, USA, using the gun technique. The metallic liquid of Au–25 at-%Si composition was solidified at the rates of 10^6K/s by propelling a small droplet onto a highly conducting copper substrate, enabling the liquid to be spread out in the form of a thin foil [1-4]. Since then it has become a very interesting topic for researchers to investigate these novel materials all around world. Because of their promising properties in comparison to their crystalline counterparts, they became quickly attractive novel materials and they are of both scientific and technological interest.

A very large number of alloy compositions in different alloy systems were synthesized in the glassy state using different rapid solidification methods. However, the requirement of very high cooling rates (10^5–10^6 K/s) have restricted the geometry of metallic glasses to thin ribbons, foils and powders [1-4, 17]. Since the latent heat of solidification is too high for metals, the required cooling rate for metallic glass production was also too high [3]. During quenching, the nucleation and growth of crystalline phases are suppressed, resulting the structural configuration to an amorphous liquid-like structure [2].

The technique of melt spinning [26] has been the most commonly used method to produce long and continuous rapidly solidified ribbons, wires, and filaments [1]. In this method, the molten alloy is ejected onto the surface of a very high-speed rotating copper wheel, allowing the production of thin amorphous alloys with a cooling rate of 10^6 K/s. The earliest technique applied for the fabrication of metallic glasses in the shape of wires or tapes for the technical application was reported by Chen and Miller in 1970 [26]. These techniques have been widely used for industrial manufacturing as well as for

research laboratory, allowing continuous production of glassy ribbons with 20-100 μm thickness and a width of centimeter scale [3].

A large variety of metallic glasses have been developed during the last 50-plus years. These could be broadly classified into metal–metalloid or metal–metal types. In a typical metal–metalloid-type (i.e. $Pd_{80}Si_{20}$, $Pd_{77}Cu_6Si_{17}$, $Fe_{80}B_{20}$, $Fe_{40}Ni_{40}B_{20}$, $Ni_{75}Si_8B_{17}$, $Fe_{40}Ni_{40}P_{14}B_6$, $Fe_{70}Cr_{10}P_{13}C_7$) glass, the metal atoms constitute about 80 at.% and the metalloid atoms (typically B, C, P, and Si) about 20 at.%. The metal atoms may be of one type or a combination of different metals, but the total amount of the metal atoms is about 80 at.%. Similarly, the metalloid component may be of one type or a combination of different metalloid atoms, whereas the total amount of the metalloid atoms is about 20 at.% [1]. In the metal–metal type (i.e. $Ni_{60}Nb_{40}$, $Cu_{57}Zr_{43}$, $Mg_{70}Zn_{30}$, $La_{80}Au_{20}$, $Fe_{90}Zr_{10}$) of metallic glasses, only metal-type atoms are involved. Unlike the metal–metalloid type, there is no compositional restriction in the case of metal-metal type metallic glasses [1].

Geometrical limitations on the section thickness (one dimension should be in micrometer scale in order to achieve such high cooling rates) of metallic glasses has prevented their application as structural or functional materials. For example, glassy alloys in sheet or wire form in the Fe–Si–B and Co–Fe–Si–B systems have been used as soft magnetic materials [27], but there have not been many reports regarding applications of these novel materials in other fields [4].

Traditional Fe-based metallic glasses are also formed as ribbons, powders or wires, because of the necessity of a high cooling rate of almost 10^6 K/s for the formation of an amorphous phase [3, 29]. The first Fe-based metallic glass had been introduced by Pol Duwez and his co-workers in 1967, when they have invented amorphous Fe-P-C alloys [28, 29]. The preparation of Fe-based metallic glass with good soft-magnetic properties from Fe-metalloid systems was first reported by Fujimori et al. [87] and O'Handley et al. [68]. In comparison to conventional silicon steels, these Fe-based metallic glasses revealed great application potential because of their cheaper production cost, higher saturation magnetization, lower coercive force, and lower core loss, which became appealing candidates to fulfill the increasing requirements of high-performance soft magnetic materials for energy saving [29]. As a result, several alloys with excellent magnetic properties have been developed up to date, such as; Fe-P-B [30], (Fe, Co, Ni)-Si-B [31], (Fe, Co, Ni)-Mo-C [32] and (Fe, Co, Ni)-M-B (M=Zr, Hf, Nb) [33]. Some of them are commercialized under the names of FINEMET, NANOPERM and HITPERM alloys and have been used widely in industry due to their outstanding soft magnetic properties [29].

BMGs are those metallic glasses that have a section thickness of at least 1 millimeter. The synthesis of first bulk metallic glass (BMG) with geometrical dimensions larger than 1mm was reported by Chen in 1974 [88]. He has synthesized 1–3 mm in diameter and several centimeters long Pd- and Pt-based alloys by water quenching at a significantly lower cooling rate of 10^3 K/s [1]. In 1982, Drehman et al. [89] were able to produce glasses that were 5–6 mm in diameter, by subjecting the $Pd_{40}Ni_{40}P_{20}$ specimens to surface etching followed by a succession of heating and cooling cycles [1]. Drehman's work clearly showed that the elimination of heterogenous nucleation sites was very helpful in decreasing the cooling rates needed to achieve glassy structure, resulting in bigger specimen dimensions. Later in 1984, Kui et al. [90] has used B_2O_3 fluxing agent to remove impurities from the molten alloy and suppress the crystallization. With this technique, they were able produce $Pd_{40}Ni_{40}P_{20}$ BMGs with 10 mm section thickness by immersing the molten alloy in molten B_2O_3 [1]. However, because of the high price of Pd, this achievement draw interest only in academic field [34].

Since the late 1980s, Akihisa Inoue and his group from Institute of Materials Research (IMR) Sendai, Japan, have found new multicomponent alloy systems with low critical cooling rates in the Mg-, Ln-, Zr-, Fe- , (Pd-Cu)-, (Pd-Fe)-, Ti- and Ni-based alloys through the stabilization phenomenon of the supercooled liquid [35]. This finding made it possible to use other preparation techniques like copper

mold casting [3]. Accordingly, in order to improve the glass forming ability (GFA) of alloys (consequently the critical diameters), alloy design principles based on the atomic sizes of the constituent elements, chemical interactions between the elements, and phase diagram considerations have been successfully used and the lowest critical cooling rate of 0.06 K/s [36] and the largest thickness for glass formation as large as 80 mm [37] have been reported [1, 38].

In recent years Fe-based BMGs have gained considerable interest due to their excellent soft magnetic properties with high saturation magnetization, high electrical resistivity, very good corrosion resistance, low materials cost, extremely high mechanical strength and hardness. In 1995, Inoue [39] has reported a distinct glass transition before crystallization in $Fe_{72}Al_5Ga_2P_{11}C_6B_4$ rapidly solidified alloy. Shortly after, the first Fe-based BMG synthesized through the stabilization of supercooled liquid in a $Fe_{73}Al_5Ga_2P_{11}C_5B_4$ system [40] had also been reported by him. Subsequently, a variety of Fe-based ferromagnetic BMGs have been developed because of their potential magnetic applications [38, 41]. Since then, a very large number of Fe based BMGs including Fe-, Fe–Co-, Fe–Ni- and Fe–Co–Ni-based alloy systems have been developed [4]. Despite their relatively complicated chemical compositions, the low price of the constituent elements, as well as the possibility to use industrial pre-alloys, make the Fe-based BMGs very attractive for industrial applications [2, 3].

1.2 Formation of metallic glasses

A glass is an amorphous solid structure, which is formed by continuous cooling from the liquid state. Metallic glasses are basically same of those traditional oxide or silicate glasses or organic polymers [1]. Therefore, they may be considered as a solid with a frozen-in liquid structure and can be referred to as "super-cooled liquid" [25]. During quenching, this supercooled liquid competes with the crystalline phase(s) [22, 24]. Figure 1.1 shows the variation of specific volume with temperature for a liquid metal. Upon cooling from the liquid state, the volume decreases steadily up to the freezing/melting point, T_m. If the rate of cooling is slow and the nuclei are present, crystallization occurs at the freezing temperature and a sudden drop is observed in the specific volume of the metal. This sudden decrease continues until

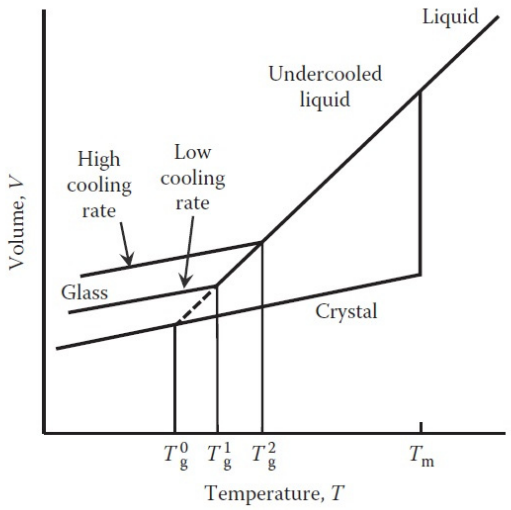

Figure 1.1: Variation of specific volume with temperature [1].

it reaches the characteristic value of the solid crystalline metal. With further decrease in temperature below T_m, the solid contracts slowly, depending on its coefficient of thermal expansion [1-3]. A liquid normally undercools (or supercools) before the crystallization. It maintains its liquid state without solidification below the melting temperature. This results from an activation energy barrier that needs to be overcome before solid nuclei can form in the melt, and this activation barrier is smaller the larger the value of undercooling. Generally, the amount of undercooling in metals is at best only a few tens of degrees. In the case of glass forming metals, the liquid can be significantly undercooled. Its volume continues to decrease with the same slop in liquid state, and the viscosity increases. At a temperature well below T_m, the viscosity becomes so high that the supercooled liquid gets frozen-in. This frozen-in liquid like solid is referred to as glass. The temperature at which the viscosity of the undercooled liquid reaches a value of 10^{12} Pa s is traditionally designated as the glass transition temperature, T_g (see Fig. 1.1). This glass transition is strictly kinetic, and its value depends on the imposed cooling rate. Higher the rate of cooling, higher is the T_g [1]. Since it is not a thermodynamically defined fixed temperature, it is appropriate to call it a transformation range [42]. With further decrease in temperature, below T_g, the specific volume of the metal decreases almost with the same slope as the crystalline form [2, 3].

Figure 1.2 shows the variations of specific heat, C_p, and the viscosity, η, with temperature. With decreasing temperature, the C_p of the undercooled liquid increases until T_g. The difference between the specific heats of the undercooled liquid and the glass grows till T_g, then a sudden drop is observed, which is a clear indication of fewer degrees of freedom as a result of supercooled liquid becoming solid glass. After the glass transition, there is very little difference in C_p between the glass and the crystal [1].

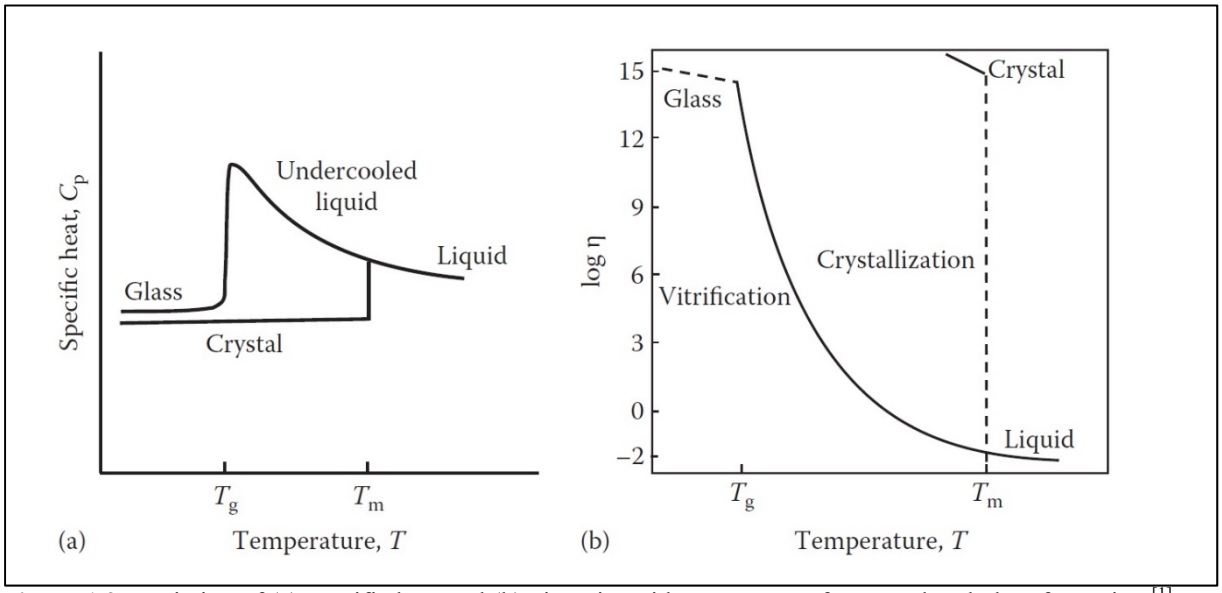

Figure 1.2: Variation of (a) specific heat and (b) viscosity with temperature for crystal and glass formation [1].

Upon cooling from the liquid state, the viscosity of a metallic liquid increases slowly with decreasing temperature. At T_m, the viscosity of the material increases suddenly by about 15 orders of magnitude. However, in the case of glass forming metal, the viscosity increases gradually even below the freezing/melting temperature T_m, in the supercooled liquid state. The rate of increase gets more rapid with further decrease in temperature. At T_g the viscosity becomes so high that there is practically no more flow of the liquid and thus the material is considered solid glass [1].

Unlike ordinary (crystalline) solids, there is no unique structure for a given glass. The structure depends on the temperature, at which departure from configurational equilibrium takes place and this temperature
is a function of the cooling rate. Like other types of glasses, glass ↔ liquid transition at T_g is reversible. Upon heating, metallic glasses can revert to supercooled liquid at T_g without crystallization. Further increase in temperature results in crystallization at T_x, which is higher than T_g. After the crystallization, they melt at T_m like ordinary solids. However, it shuld be noted that, T_x is not a thermodynamic parameter like the melting temperature of a metal. It depends on the applied heating rate and higher the rate of heating, higher is the T_x. Therefore, if sufficent time provided, metallic glasses can also crystallize at the temperatures lower than T_x [1]. The temperature interval between T_x and T_g is referred to as the width of the supercooled liquid region, that is, $\Delta T_x = T_x - T_g$. This temperature interval is usually large in the case of BMGs and it is taken as an indication of the thermal stability of the glass against crystallization. However, in the case of rapidly solidified thin ribbons, ΔT_x is usually very small and it is common that it cannot be observed at all, since most of the melt-spun ribbons do not show T_g on their DSC plots [1].

1.2.1 Thermodynamic considerations for glass formation

Metallic glasses are, just like the other glasses, not in an themodynamically stable state. It means that, since they are in an excited state, when they are provided sufficent amount of time at any given temperature, they will relax and eventually transform to their crystalline state. However, this time scale varies from a couple of minutes to thousands of years. From this fact rises the question, how can the thermodynamic equations be applicable to a system that not in an equilibrium state. According to Johnson [42] and Leuzzi and Nieuwenhuizen [43], when the system is an undercooled liquid, it is possible to do so. Turnbull [44] has showed that, metallic liquids can be undercooled for extended periods of time, since the critical size of the nucleus to form the crystalline phase is infinetly large at the melting temperature, T_m. In other words, the time required for the nucleation of the crystalline phase is extremely large at T_m and it decreases with increasing amount of undercooling. When the timescale for nucleation is sufficiently long, the undercooled liquid can be considered in a metastable state, for which the thermodynamic principles are applicable [1].

The thermodynamic stability of a system at constant temperature and pressure is determined by its Gibbs free energy, G, defined as

$$G = H - TS \tag{1.1}$$

Where, H is the enthalpy, T is the absolute temperature, S is the entropy. If a system is in stable equilibrium, which means it will not transform into any other phase(s) at given temperature and pressure, its must have attained the lowest possible value of the Gibbs free energy. According to Equation 1.1, a system can be made more stable at any given temperature, either by increasing its entropy or decreasing its enthalpy, or both. Crystalline solids have strongest atomic bondings and therefore the lowest enthalpy, H, at lower temperatures. As a result, solids are the most stable phases at low temperatures. However, with increasing temperature the frequency of lattice vibrations also increases and therefore the entropy becomes high at elevated temperatures. As a result, with increasing temperature and entropy, the value of the $-TS$ term dominates at elevated temperatures. For this reason, liquids and gases become more stable at elevated tempetatures, because these phases possess more freedom of atomic movement [45, 46].

A crystalline phase normally has a lower free energy than the glassy phase [4]. However, when a glassy phase has the lower free energy compared to the competing crystalline phase(s), the glass becomes more "stable". It means that, the change in the free energy, $\Delta G = (G_{glass} - G_{crystal})$, becomes negative.

Mathematically it can be expressed as:

$$\Delta G = \Delta H_f - T\Delta S_f \quad (1.2)$$

where the Δ symbol represents the change in these quantities between the final and initial states, H_f and S_f represents the enthalpy of fusion and entropy of fusion, respectively. The system becomes stable when the value of G is at its the lowest, or ΔG is negative. A negative value of ΔG can be obtained either by decreasing the value of ΔH_f or increasing the value of ΔS_f, or both. Since entropy is a measure of the different arrangement possibilities of the constituent atoms (microscopic states), it will increase with increasing number of components in the alloy system. Thus, even if ΔH_f remains constant, the free energy will be lower because of the increased entropy when the alloys system consists of many components. However, the value of ΔH_f will also not stay constant resulting from the chemical interaction between the constituent elements [1, 2].

The free energy of the system at a constant temperature can also be decreased, in cases of low chemical potential due to low enthalpy, and large interfacial energy between the liquid and solid phases. Since it will be difficult to intentionally control these parameters in an alloy system, the easiest way to decrease the free energy would be to increase ΔS_f by increasing the number of components in the alloy system. This is why it has been easier to synthesize glassy phases in ternary and higher-order alloy systems than in binary alloy systems [2, 35]. In 1993 A.L. Greer [47] explained this behavior in a simpler and concise way: the alloy has a low chance to select a crystalline structure when a wide variety of elements is present in its composition, it is "too confused to crystallize", because more components in an alloy system will retard the formation of competing crystalline phases during cooling [3, 29]. Obviously, it will be much easier to produce the glassy phases in alloys containing a large number of components, that is, in multicomponent alloy systems. BMGs, which can be produced in the glassy state at very slow solidification rates, are typically multicomponent alloy systems. Increases in ΔS_f also result in an increase in the degree of dense random packing of atoms, which leads to a decrease in ΔH_f and, consequently, an increase in the solid/liquid interfacial energy, σ. Both these factors contribute to a decrease in the free energy of the system [1, 2].

1.2.2 Kinetics of glass formation

Kinetic criteria for glass formation deals with the rate of cooling relative to the crystallization kinetics, that is, crystal nucletion and growth [4]. As stated by the free-volume model [48] and the entropy model [49], it is expected that every liquid will undergo a glass transition, provided that the crystal nucleation and/or growth is bypassed or avoided. In other words, whether a glass forms or not is related to the rapidity with which the liquid can be cooled and also to the kinetic constants. Therefore, glass transition phenomenon turns out to be purely kinetic in nature [1, 3].

Volmer and Weber [91] made the first attempt to describe the nucleation process by considering the condensation of supersaturated vapour [3, 52]. Later Becker and Döring extended the same model [92]. Fisher and Turnbull applied the basic concepts of this theory to the liquid-solid phase transition [93]. According to Turnbull [22], the crystallization of a fluid occurs by the formation, called "nucleation", of

crystallization centers (nuclei) and the growth of these at the expense of the adjacent fluid. Hence, it is confined entirely to the interfaces where the crystal and fluid meet. This means that, at any time, only a minute part of the material is able to crystallize. In contrast, a glass forms homogeneously by the kinetic freezing of atoms throughout the entire liquid but the the extraction of heat which usually motivates glass formation is normally through the external surfaces of the liquid [22].
The crystallization rate of an undercooled liquid is specified by the rate of crystal nucleation, I and by the speed U, with which the crystal-liquid interface advances. Both of these rates are strongly dependent on the reduced temperature T_r and the reduced undercooling ΔT_r, which are defined as [22]:

$$T_r = \frac{T}{T_m} \qquad \Delta T_r = \frac{T_m - T}{T_m} \tag{1.3}$$

where T_m and T are the melting temperature and the actual temperature, respectively.

Nucleation in an undercooled liquid occurs almost always heterogeneously (because the nucleation barrier is smaller in the case of heterogeneous nucleation) on seeds which are either present accidentally in the system, or intentionally injected into it. These seeds might be crystals of the same material or other solid materials, such as the container walls or suspended particles in the liquid. At a given cooling rate, the necessary undercooling for heterogeneous nucleation changes widely with composition and structure of the seed material [22]. Nucleation, which takes place without the help of seeds is called homogeneous. Experimentally it is difficult to avoid the effects of seeds and thereby reveal homogeneous nucleation behaviour. Liquids usually contain 10^5 to 10^6 suspended particles per cm^3. When the liquid is undercooled, nucleation will first occur on the most effective seed and then, unless the crystal growth rate is very small, recalescence will break off the possibility of any further independent nucleation either on other seeds or homogenously [22].

Upon phase transitions, such as solidification, the transformation process cannot occur at any arbitrarily small undercooling. The reason for this is the small curvature of the interface related with a crystal of atomic dimension. This curvature lowers the equilibrium temperature so that, the smaller the crystal, the lower is its melting point. Accordingly, the smaller the difference (undercooling) between the melting point and the temperature of the melt, the larger will be the critical size of the crystal. In liquid metals, random fluctuations may create tiny crystalline regions (clusters, embryos) even at temperatures above the melting point, but these will not be stable and thus remelt. They will remain metastable also just below the melting point because of the relatively large excess energy required for surface formation, which tends to weight the energy balance against their survival when they are small [94]. As a result, nearly all of these fluctuations will decay before reaching critical size, since it is very unprobably for such a large number of atoms to arrange themselves on the sites of the corresponding solid crystal lattice, when the undercooling is not large enough [22, 94]. Once the nucleation barrier is exceeded and a stable nucleus is formed, it will continue to grow spontaneously. In the case of heterogeneous nucleation, the number of atoms in the critical nucleus is smaller than that for homogeneous nucleation as a consequence of the catalytic substrate. Through the partially replacement of the solid/liquid interface by an area of low-energy solid/solid interface (catalytic substrate), the activation energy required for nucleation and the number of atoms in a critical nucleus decreases [22, 94]. This is the reason why the heterogeneous nucleation takes place before the homogeneous nucleation starts [3].

Based on simple nucleation theory, the homogeneous nucleation rate I, for the formation of crystalline nuclei from a supercooled melt (in a liquid free of nuclei or heterogeneous nucleation sites) can be expressed as [22]:

$$I = \frac{k_n}{\eta(T)} \exp\left[-\frac{b\alpha^3\beta}{T_r(\Delta T_r)^2}\right] \tag{1.4}$$

where k_n is a kinetic constant, b is a shape factor (=16π/3 for a spherical nucleus), $\eta(T)$ is the shear viscosity of the liquid at temperature T, and α and β are dimensionless parameters related to the liquid/solid interfacial energy σ and to the molar entropy of fusion ΔS_f, defined as [22]:

$$\alpha = \frac{\left(N_A \overline{V}^2\right)^{1/3} \sigma}{\Delta H_f} \tag{1.5}$$

$$\beta = \frac{\Delta H_f}{RT_m} = \frac{\Delta S_f}{R} \tag{1.6}$$

where N_A is Avogadro's number, $\overline{V}$ is the molar volume of the crystal, H_f is the molar heat of fusion and R is the universal gas constant. The principal resistance of a fluid to nucleation is limited to α, which is proportional to the liquid-crystal interfacial energy σ. Physically α is the number of monolayers/area of a crystal, which would be melted at T_m by an enthalpy ΔH equal to σ [3, 22]. It is clear from Equation 1.4 that for a given temperature and η, as $\alpha\beta^{1/3}$ increases, the nucleation rate I decreases very steeply. Increasing α and β means an increase in σ and ΔS_f and/or a decrease in ΔH_f, indicating again an improved thermal stability of the supercooled liquid, all consistent with the thermodynamic approach [1].

Figure 1.3 shows the calculated variation of the logarithm of the frequency of homogeneous nucleation of crystals in an undercooled liquid with reduced temperature for various values of $\alpha\beta^{1/3}$ [22]. For numerical modelling the number b was assigned its value for a sphere (16π/3), η was set equal to 10^{-3} Pa s, independent of temperature, and k_n was given the value 10^{23} Nm [22]. It is possible to see that I is negligible at small undercooling. In fact, I must become 10^{-6} /cm^{3}s or larger in order to be observable under common experimental conditions.

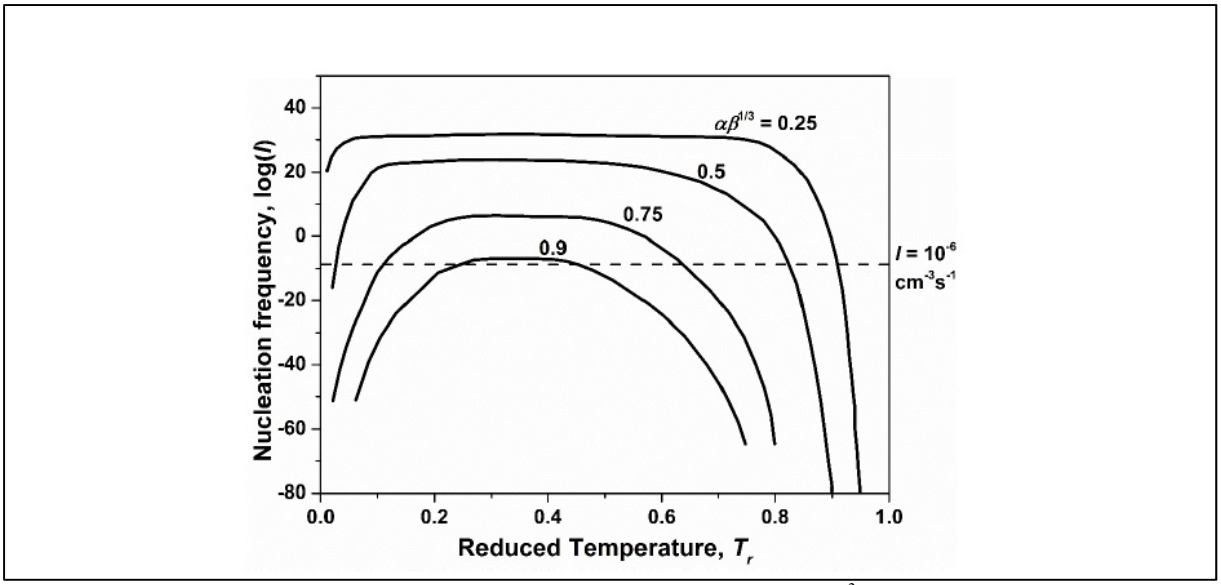

Figure 1.3: Calculated dependence of the logarithm of the frequency (in 1/cm^{3}s) of homogeneous nucleation of crystals in an undercooled liquid as a function of the reduced temperature for various values of $\alpha\beta^{1/3}$ as indicated in [22], computed with the Eq. (1.4) [2, 3].

This means that the part of the I-ΔT_r relation closest to equilibrium, where the simple theory is most valid, is practically inaccessible to the experiment. With increasing ΔT_r, I increases to a broad maximum at T_r = 1/3 and falls to zero at T = 0 K. Liquids with $\alpha\beta^{1/3} > 0.9$ would practically not crystallize at any undercooling, unless they are seeded. Thus, they would form glasses if sufficiently undercooled. In contrast, it should be practically impossible to suppress, upon cooling to 0 K, the crystallization of fluids with $\alpha\beta^{1/3} < 0.25$. Experience indicates that β lies between 1 and 10 for most substances and it is near 1 for most simple monoatomic liquids, such as metals. α has been measured directly only in a few instances and there is no rigorous theory for predicting it [22]. It is reasonable to assume that it may be not greater than unity. In agreement with experimental results, the value of $\alpha\beta^{1/3}$ for metallic melts has been estimated to be about 0.5.

As mentioned before, the formation of the glassy phase is related to a significant increase in the viscosity of the undercooled melt at T_g. That is, any liquid that attains a viscosity of 10^{12} Pa s without crystallization will be considered a glass, irrespective of the alloy system and composition [1]. The viscosities of most common liquids above their melting point are of the order of 10^{-3} Pa s. It is evident that, to change from this value to 10^{12} Pa s, the viscosity must increase very rapidly over some part of the temperature range in the transition from liquid to glass. The viscosities of glass-forming liquids, between 10^{-3} and 10^{6} Pa s, are well described by the Fulcher [95] equation [22]:

$$\eta = A\, exp\left(\frac{a}{T-T_o}\right) \tag{1.7}$$

where A, a and T_0 are constants depending on the material and T is the absolute temperature. When T_o = 0, the equation assumes the familiar Arrhenius form. η will increase very rapidly with falling temperature either when a is very large relative to T or, if a is small, when T has fallen nearly to T_o. The viscosities of pure silica or of germanium are quite well described by an Arrhenius equation. In contrast, the viscosities of such glass formers as toluene or isobutyl chloride are described [96] by rather small values of a but with T_o's which are substantial fractions (e.g. 1/2 to 2/3) of the thermodynamic crystallization temperature, T_m. This means that the viscosity is low and increasing slowly with falling

temperature above T_m, but it then increases with extreme rapidity when the temperature falls nearly to T_o. The change from the quite fluid to the solid condition, characteristic of the glass, then occurs over quite a narrow temperature interval above T_o [22].

Further, Turnbull explained that the glass-forming tendency should increase with the reduced glass transition temperature $T_{rg} = T_g/T_m$ [1-4, 22, 29, 52 ,53, 66]. The higher this value, the higher the viscosity and, therefore, the alloy melt could be easily solidified into the glassy state at a low critical cooling rate. The effect of the different assignments of T_{rg} on the homogeneous nucleation frequency, calculated from the simple theory, with a value of $\alpha\beta^{1/3}$ to be 0.5, is shown in Figure 1.4. The viscosity was calculated from the Fulcher equation (see eq. 1.7) with constants typical of simple molecular liquids and with $T_{ro} = T_{rg}$. The temperature at which η become 10^{14} Pa s is considered as T_g [3, 22, 52].

Figure 1.4 shows the effect of increasing the reduced glass transition temperature, T_{rg} on I-T_r relation. With increasing T_{rg}, the peak lowers, sharpens and shifts to higher T_r values. Seed-free liquids with a glass transition temperature as high as $2/3T_m$ (T_{rg} = 0.66) would crystallize only in a narrow temperature range and with a low nucleation frequency. Thus, they could be easily undercooled to the glassy state with low cooling rates. Liquids with $T_g = 1/2T_m$ (T_{rg} = 0.5) could be undercooled to the glassy state only in relatively small volumes and at high cooling rates [2, 3, 22, 52].

The equation for the growth rate, U, of a crystal from an undercooled liquid can be expressed as:

$$U = \frac{10^2 f}{\eta}\left[1 - exp\left(-\frac{\Delta T_r \Delta H_f}{RT}\right)\right] \tag{1.8}$$

where f represents the fraction of sites at the crystal surfaces where atomic attachment can occur. Here also we can see that U decreases as η increases and will thus contribute to increased glass formability. Since both I and U vary, at any given temperature, as $1/\eta$, both the glass-forming tendency and the stability of the glass should increase with reduced T_{rg} and increasing values of α and β [1].

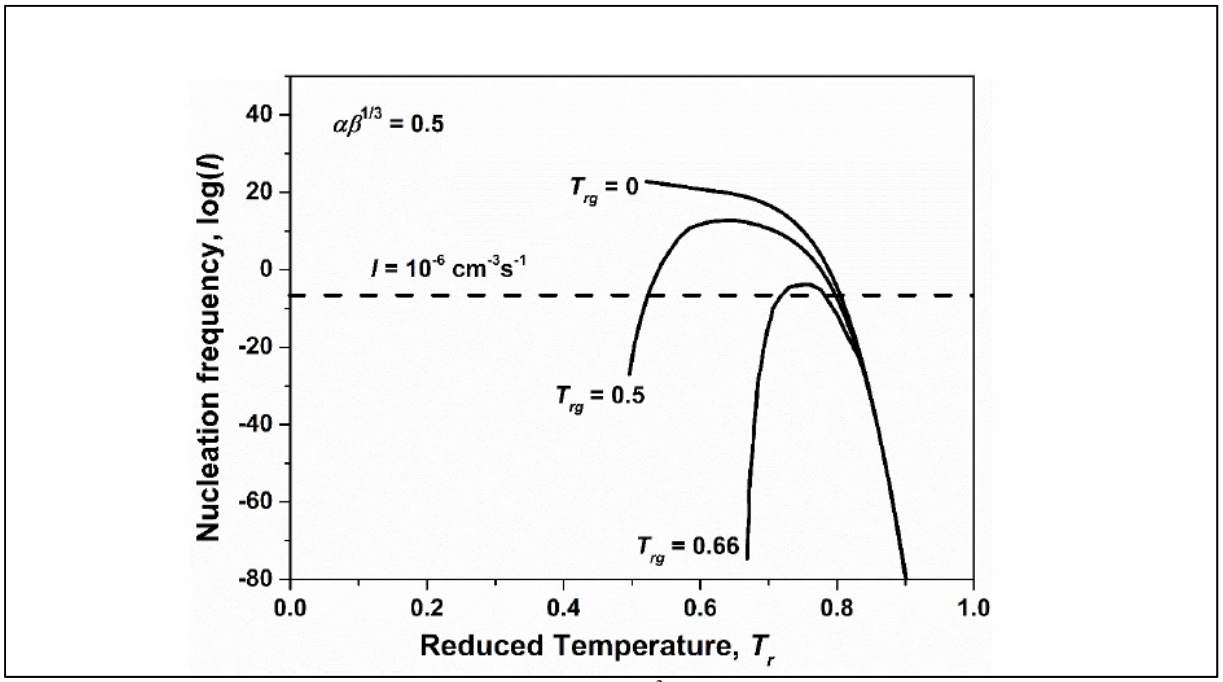

Figure 1.4: Variation of the logarithm of frequency (in 1/cm^{3}s) of homogeneous nucleation of crystals in liquids

with reduced temperature calculated from Eq. (1.4) as indicated in [22]. $\alpha\beta^{1/3}$ was set equal to 0.5 and the viscosity was calculated from the Fulcher equation with indicated assignments of T_{rg}, assumed equal to T_{r0} in Fulcher equation [2, 3].

1.3 Crystallization behavior

Regardless of the method they are synthesized, metallic glasses are in a nonequilibrium state with respect to thermodynamic stability. That is, when they are heated to sufficiently higher temperatures, they tend to attain a more stable condition. However, their deviation from the configurational equilibrium is strongly depends on the processing route used for their production [1, 97], which means that, upon annealing below the glass transition temperature, the as-synthesized glass slowly transforms toward an "ideal" glass of lower energy through structural relaxation. This state corresponds to the ideal frozen liquid without any defects [97]. Practically, every glass possesses defects and the amount of these defects also depends on the temperature, at which departure from configurational equilibrium takes place. The nature of the defects in metallic glasses is currently unknown and all defects that are present in a glass considered as free volume [1]. On annealing, as-synthesized glass evolves to one with higher density through the annihilation of free volume, which could be considered characteristic of glass formation at a slower cooling rate (see Figure. 1.1) [97].

The process of structural relaxation will be complete by the time the glass reaches the T_g temperature. This is the reason of the independence of the transformation temperatures regarding the preparation method has been used. As mentioned before, T_g is a kinetic parameter and inreases with inreasing cooling rate. For this reason, it is reasonable to think that there should be a significant difference between the melt-spun ribbons and BMGs of the same composition regarding their T_g's. However, this is not true, because T_g is an estimation made during the cooling of the molten alloy. On the other hand, its value is measured upon continuious heating of the glass, which has already formed. Once the glass is heated from room temperature to T_g, structural relaxation will be complete and it will not matter how the glass had initially formed. Thus, both type of glasses will have the same T_g and T_x, as long as they are measured at the same heating rate [1].

The amorphous to crystalline transformation is expected to take place at or above the crystallization temperature, T_x, which is commonly measured with a differential scanning calorimeter (DSC), upon continuous heating of the sample at a constant heating rate. However, T_x is a function of the heating rate employed and it increases with increasing rate of heating [1]. The crystallization peaks of a DSC plot indicate a very rapid crystallization and the peak temperatures are called T_x. It is important to mention that the T_x temperature is not a sharply defined temperature (unlike the melting temperature, T_m), rather a temperature range, in which the rate of crystallization increases very strongly with the temperature [98].

As previously mentioned, all metallic glasses, whether synthesized in the form of thin ribbons or cm sized bulk rods, can be considered as a metastable deeply undercooled liquid and consequently lower their energy by transforming into more stable crystalline or quasicrystalline phase(s) [1, 3]. However, the most promising and interesting properties of metallic glasses like excellent magnetic behavior, high hardness and strength combined with bending ductility, corrosion resistance have been found to deteriorate or lost because of the crystallization process [98]. Therefore, crystallization studies of alloys are important from both scientific and technological points of view [1].

From a technological point of view, understanding the micromechanisms gives the opportunity to control or impede the crystallization, which is a prerequisite for most applications, since the T_x temperature provides a real upper limit to the safe use of metallic glasses without loss of their

interesting combination of properties [1, 98]. However, it should be taken into account that T_x is not a direct indicator of the safe operating temperature of a metallic glass [1]. For example, most of the Fe-based metallic glasses have a T_x close to 400°C, but their maximum long-term operating temperatures are only of the order of 150°C [99].

Besides technological aspects, studies on the crystallization behavior of metallic glasses also provide opportunities to study the kinetics of crystallization, which enables the tailoring of the microstructure in order to obtain a glass + nanocrystal or an ultrafine grained composite or a crystalline material with different grain sizes [100]. Controlling the time and temperature of crystallization makes it possible to synthesize BMG composites of a fine crystalline phase dispersed in the amorphous matrix and those composites exhibit appealing mechanical properties such as very high strength [50] and ductility [51]. These special microstructures cannot be obtained from the liquid and crystalline states [98].

The dimensions and morphologies of the crystallization products strongly depend on the transformation mechanism, which is closely related to the chemical compositions of the amorphous phase and to the thermodynamic properties of the corresponding crystalline phases [100]. The crystallization reactions can be classified according to their concentration change [98]. In Figure 1.5, an overall picture of reactions which can take place during crystallization of Fe-B binary system is shown in a hypothetical free energy versus composition diagram [98].

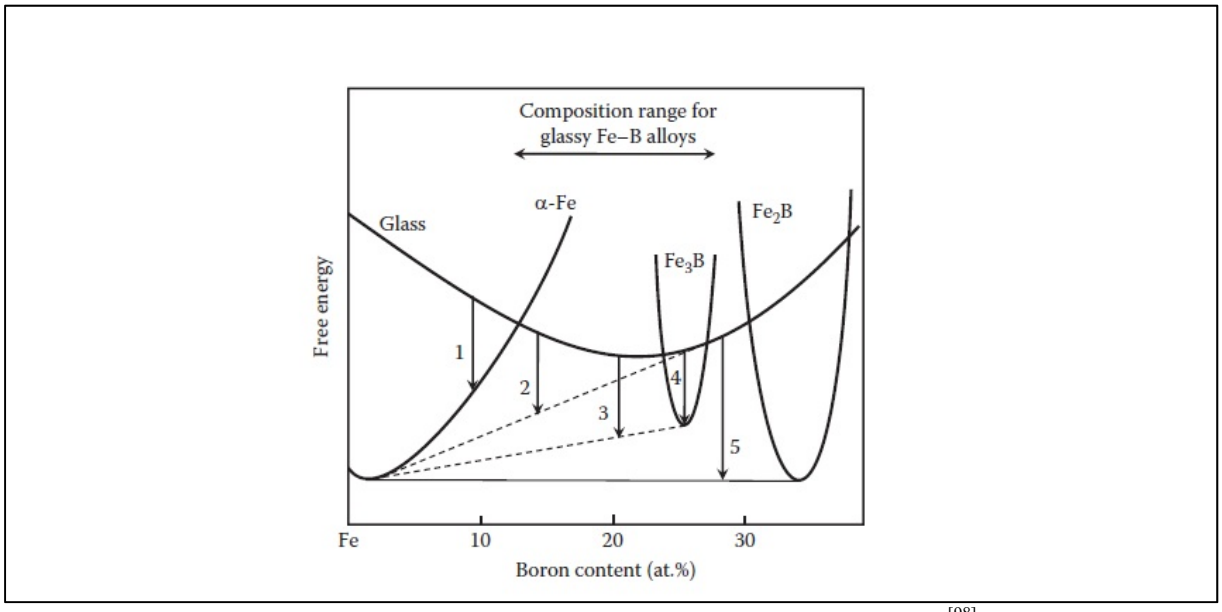

Figure 1.5*:* Hypothetical free energy vs. composition diagram for Fe-B alloy system [98]. The numbers 1 to 5 represent crystallization reactions between the glassy phase and the equilibrium α-Fe and Fe_2B phases, metastable Fe_3B phase [1].

In polymorphous crystallization, the amorphous alloy transforms into a stable (α-Fe) or metastable crystalline solid solution, or into a stable (Fe_2B) or metastable (Fe_3B) crystalline compound, without any change in its concentration. That means, it occurs only in composition ranges corresponding to a stable/metastable solid solution or a stable/metastable crystalline phase. Reaction 1 (supersaturated α-Fe) and Reaction 4 (metastable Fe_3B) are examples of polymorphous crystallization. Since the glassy phase was only reported to form in the composition range between 12 and 27 at.% B in the Fe-B alloy system, the last reaction (polymorphous crystallization into the stable Fe_2B phase) will not be possible [1]. Since Fe_3B phase is metastable, it will subsequently transform into a mixture of the equilibrium α-Fe and Fe_2B phases on further annealing. Likewise, the supersaturated α-Fe phase (Reaction 1) will

decompose by subsequent precipitation reactions and transform into the stable α-Fe and Fe_2B phases [98]. This type of crystallizations has been least common among the metallic glasses [1].

In eutectic type of crystallization, the glassy phase simultaneously transforms into two crystalline phases (e.g. by Reaction 3: α-Fe + Fe_3B or by Reaction 5: α-Fe + Fe_2B) through a discontinuous reaction [98]. This mode of crystallization has the largest driving force and can occur in the whole concentration range between the two stable or metastable phases. Like polymorphous crystallization, the eutectic crystallization is a discontinuous reaction; the overall composition of the crystal and the glass are the same [1].

Crystallization of a single phase accompanied by a composition change is referred to as primary crystallization. During this reaction, a concentration gradient occurs at the interface between the supersaturated solid solution and the glassy phase until the reaction reaches the metastable equilibrium [3]. This kind of a reaction corresponds to Reaction 2. Since the solute (boron) concentration in the α-Fe is lower than that in the glassy phase, the solute atoms will be rejected to the glass and the remaining glassy phase will be enriched in boron until further crystallization is stopped by reaching the metastable equilibrium [1, 98]. Later, according to its B concentration, this B-enriched glassy phase can transform by one of the mechanisms described above. For example, if the B concentration is close to 33 at.%, it will transform into the stable Fe_2B phase by a polymorphous crystallization. Alternatively, if it is close to 25 at.%, transformation results in metastable Fe_3B phase. On the other hand, if it is different from the values, eutectic type of crystallization can occur [1]. The dispersed primary crystallized phase may act as an heterogenous nucleation site for the further crystallization of the amorphous phase [98].

1.4 Magnetic properties of metallic glasses

Soft magnetic properties are of fundamental importance for several applications in the electrical and electronic industries [1]. Over the past several decades, amorphous materials have been investigated for applications in magnetic devices requiring magnetically soft materials such as transformers, inductive devices, etc. [53]. Thus, a very large number of studies have been conducted on Fe-based melt-spun ribbons starting from the pioneering investigation of Duwez [28] on the Fe–P–C system in 1967 [1]. Due to the relatively low coercive force, low core loss, and cheap cost, conventional Fe-based soft-magnetic amorphous ribbons called FINEMET, NANOPERM, and HITPERM, have been widely applied as transformers, motors, sensors, and other electric and electronic components [29]. These alloys may be single phase (Type I) but are generally two-phase materials with a nanocrystalline ferromagnetic phase and a residual amorphous phase at the grain boundaries (Type II) [53]. However, the application of these materials in power transformers and other energy-conversion devices has been limited by their small thickness and lower saturation magnetization compared with traditional crystalline alloys. For example, the low GFA makes the thickness of these Fe-based MG ribbons less than 50 μm, which results in the low packing density of the transformer core and thus increases the Joule losses [54]. Therefore, developing Fe-based BMGs with high GFA and large saturation magnetization have been one of the main goals in the past twenty years [29]. The nature of magnetic investigations in BMG alloys has followed trends very similar to those in the case of melt-spun glassy ribbons. In fact, even for BMG compositions, several researchers have been studying the magnetic behavior using melt-spun ribbons, since except minor differences in magnetostriction and coercivity, they exhibit the same soft magnetic properties [1].

Because of the lack of periodicity in the atomic arrangement, it was believed for a long time that ferromagnetism could not exist in amorphous solids [56]. The existence of ferromagnetism in amorphous solids has been predicted theoretically by Gubanov et al. [55] in 1960, who calculated the effect of structural disorder on the Curie temperature [59]. His work was based on evidence that the electronic band structure of crystalline solids did not change in any fundamental way on transition to

the liquid state [56]. The model used by Gubanov does not require any periodic arrangement of the atoms in a lattice and takes into consideration only the exchange interactions of neighboring atoms and the radial distribution function of the structure; which is basically not different from the crystalline cases where Heisenberg-Dirac direct exchange interactions are usually considered up to the first or second nearest neighbors to calculate the magnetization and the Curie temperature of a system [57, 58].

The magnetic dipole moments of elemental and alloy magnets are most completely understood through the band theory of solids. The calculation of spin-resolved energy bands and densities of states allows for the description of atom resolved magnetic dipole moments and, therefore, spontaneous magnetization of elemental and alloy magnetic solids [53]. Only the three transition elements Fe, Co, and Ni exhibit ferromagnetism at room temperature. In addition to the elemental magnets, ferromagnetism is also found in the binary and ternary alloys of Fe, Co, and Ni with each other, in alloys of Fe, Co, and Ni with other elements, and in a relatively few alloys which do not contain any ferromagnetic elements [61]. It is well known that the magnetic dipole moment of Fe, Co and Ni atom is 2.22 μ_B, 1.72 μ_B and 0.60 μ_B, respectively, at 0 K [53, 61, 63-66]. For crystalline magnetic alloy design, the Slater-Pauling curve is an important starting point. It illustrates the mean atomic magnetic dipole moment as a function of composition in TM alloy system [53].

When a ferromagnetic metal is alloyed, the effect of the solute on saturation magnetization can be basically divided into two parts. First, the presence of foreign atoms is bound to change the atomic moment on an average basis. In other words, if we denote the mean atomic moment of the alloy by $\bar{\mu}$ and the atomic moment of the parent metal by μ_1, $\bar{\mu}$ always differs from μ_1, regardless of the species of the solute. The main goal in alloying is to make $\bar{\mu} > \mu_1$. If the solute atoms also carry magnetic moments, there will be a second effect of the solute, namely, the mode of the coupling between moments of the solute and solvent atoms. Obviously, ferromagnetic coupling is sought, if it is expected that the alloy shows an improved magnetic saturation. Both effects can be expressed by the empirical equation [66]:

$$\bar{\mu} = \mu_1 + (d\bar{\mu}/dc)c$$

where c is solute concentration in atomic percent and $d\bar{\mu}/dc$ gives the rate at which mean atomic moment changes with c. The magnitude and sign of $d\bar{\mu}/dc$ represent the first and second effects, respectively. To understand the different effects of solutes, the observed average values for $\bar{\mu}$ of many important binary alloys are plotted against the average number of the outer electrons, N (or n as in the figure), in Figure 1.6; where $N = Z_1(1-c) - Z_2c$, with subscripts 1 and 2 referring to the solvent and solute, respectively, and Z_1 and Z_2 are the valence electron numbers [66].

The desire for large saturation limits choices of alloys to those rich in Fe or Co and therefore near the top of the Slater-Pauling curve [53]. The addition of cobalt, which is less magnetic than iron, increases the magnetization ($d\bar{\mu}/dc > 0$), and the 30% Co alloy has a higher value of saturation magnetization at room temperature than any other known material [61]. Perhaps the most significant implication of the Slater - Pauling curve is that alloys of the iron-group metals behave magnetically as if they belong to two distinct groups. Alloys lying on the left side of the peak feature a positive slope ($d\bar{\mu}/dc > 0$), whereas those lying on the right side constitute another group displaying a negative slope ($d\bar{\mu}/dc < 0$) [66].

Basically, there are two types of the ferromagnetism. When the Coulomb interaction strength is large enough, we can expect that the up-spin band is below the Fermi level (a completely filled majority-spin band) so that the magnetization is not changed by the magnetic field. Another case is that holes remain in the up-spin band (both spin bands are partially filled at the Fermi energy) so that both the up and down bands are laid on the Fermi level. The former is called the strong ferromagnetism and the latter is called the weak ferromagnetism [70]. The alloys on the left-hand side of the Slater – Pauling curve, as well as Fe are considered as weak ferromagnets, the right-hand site alloys and Co and Ni are considered as strong ferromagnets.

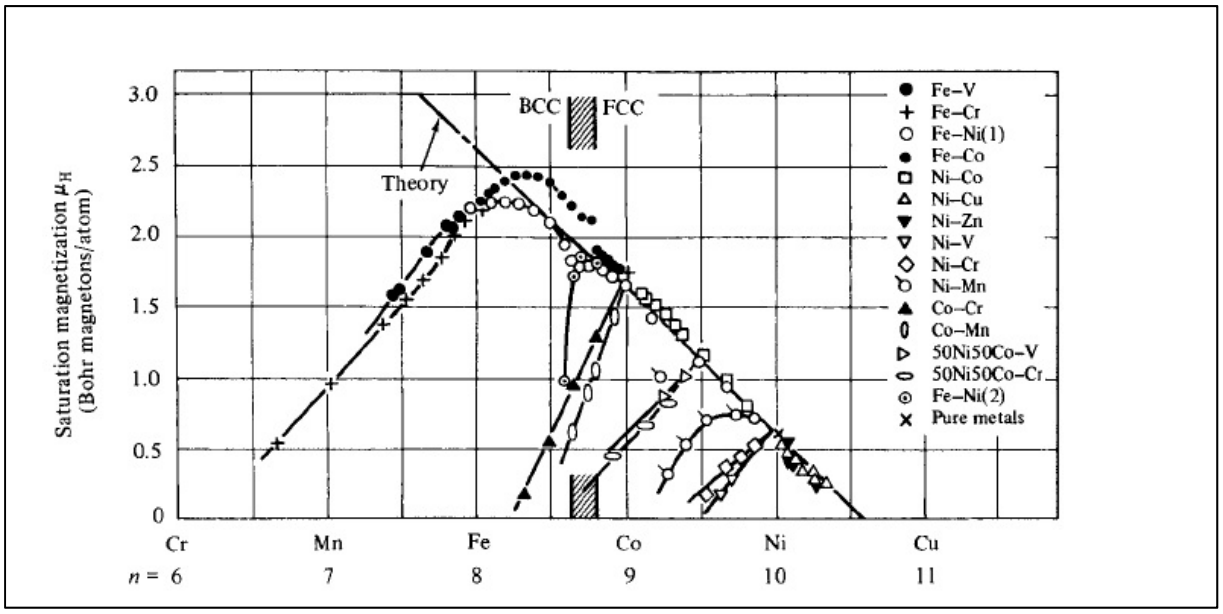

Figure 1.6: Slater–Pauling curve: dependence of saturation magnetization of alloys on the number of valence electrons per atom [61].

The local environment around each atom in an amorphous solid differs from site-to-site in contrast to the regular crystalline structure. Therefore, the magnetic moment of an atom is not expected to be identical on every site in the solid. However, the effect of this distribution is not apparent in the magnetic moments. The major change in magnetic properties observed in amorphous alloys comes from the change in the electronic environment caused by the metalloids [56]. The mean atomic magnetic moments of most amorphous alloys are lower than those of the pure crystalline transition metals which they contain. However, the direct effect of the structural disorder on the moments is very small [56]. The most important changes in the magnetic dipole moments in amorphous alloys depend more strongly on alloy chemistry rather than positional disorder [53]. The moments are lower because of the change in the local chemical environment provided by the presence of the metalloids. These same metalloids are necessary for preparing and stabilizing the amorphous structure [56].

Metallic glasses are rather poor conductors, but their 3*d*-electrons are just as "itinerant" as in crystalline transition metal alloys. Thus, the 3*d*-electron magnetic moments should be discussed in terms of the band theory of magnetism. The rigid band model is often used to correlate results, but it has no theoretical basis. The rigid band theory assumes that the d-bands do not alter on alloying; they just fill or empty. The success of rigid band theory in certain alloy systems is due to a fortuitous cancelling of errors and both theory and experiment show that the band structure does change shape. The addition of metalloids also changes the *d*-bands and does not simply transfer charge. Because the d-bands are not rigid, the plotting of moment against average number of valence electrons, the

Slater−Pauling curve, is without theoretical basis. However, because of the simplicity in correlating the experimental results, the rigid band phenomenology has been commonly used for qualitative interpretation [53]. The concentration dependence of the magnetic moment in amorphous alloys where a transition metal substitutes for another transition metal was studied by many authors. Mizoguchi [69] performed the first systematic investigation of the effect of TM substitution on a series of amorphous $(Fe_{1-x}TM_x)_{80}P_{10}B_{10}$ (TM = Ni, Co, Mn, Cr, V) alloys [59]. In Figure 1.7 the magnetic moments for a wide variety of transition metal alloys with $P_{10}B_{10}$ glass formers are shown as a function of the average valence electron number, N [56].

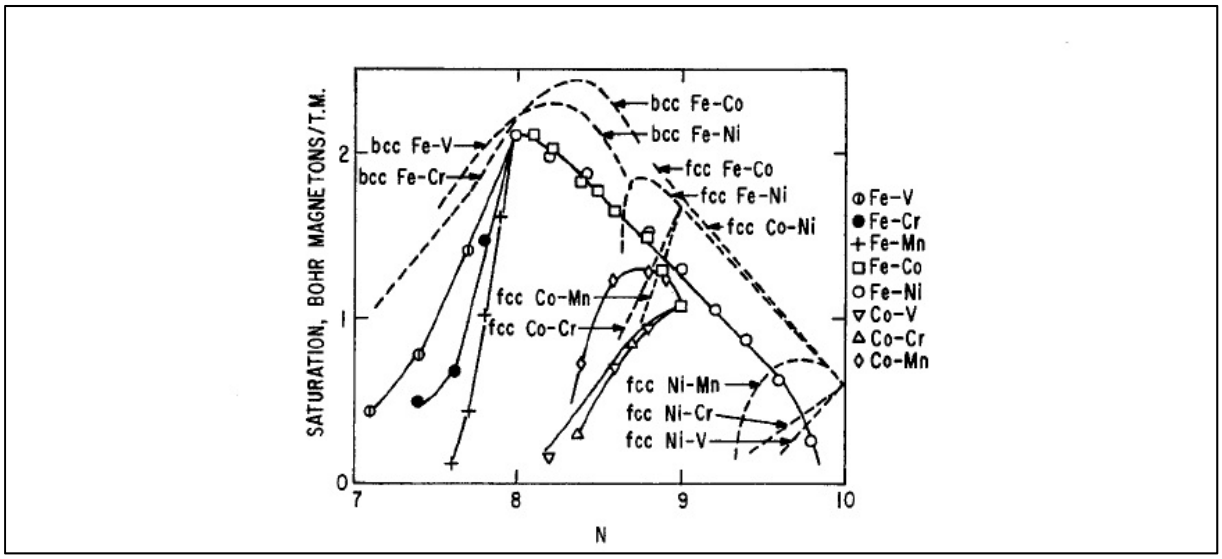

Figure 1.7: The saturation magnetization of amorphous alloys of 3d transition metals $(Fe_{1-x}TM_x)_{80}P_{10}B_{10}$ (TM = Ni, Co, Mn, Cr, V) as a function of the average outer electron concentration, N, of the metallic atoms. Crystalline alloys without P, B shown by dashed curves [56, 62, 69, 71].

As seen from Figure 1.7, these alloys show a uniform reduction of the magnetization as compared with those of the crystalline alloys [70]. The approximate shape of the Slater-Pauling curve is preserved for the amorphous alloys, but the curve is shifted by the assumed transfer of electrons, that is, the metalloid atoms contribute some of their *s*, *p* electrons to fill the *d* band of the transition metal atoms [53, 56, 62, 69]. Fe-Ni and Fe-Co amorphous alloys follow an almost straight line parallel to the right-hand side of the Slater-Pauling curve, shifted to the left by 0.4 electrons per atom [59, 71]. The difference between the crystalline and amorphous data along the right-hand side of the curve (strong ferromagnets) was described in terms of charge transfer from the metalloid elements to the transition metal *d* band [62, 69], however, the shift to the left corresponds to the peak position shift of the DOS with the addition of metalloids and this shift is caused by the change in chemical bonding between TM and metalloid atoms [70].

It is also remarkable that no Invar anomaly is observed in the Fe-Ni system, which normally occurs in crystalline Fe–Ni alloys, the saturation magnetization suddenly decreases around 65 at% Fe, over the concentration range between bcc and fcc phases [59, 62, 70]. Similar to their crystalline counterparts in Figure 1.6, iron-based (Fe-rich) amorphous alloys are regarded as weak ferromagnets, cobalt-based (Co-rich) and nickel-based (Ni-rich) amorphous alloys are strong ferromagnets [62, 72]. The trend with transition metal content is the same as for the corresponding crystalline alloys although there are anomalies, which is shown in Figure 1.7. For example, crystalline (bcc) Fe-Co alloys show a peak in magnetization at about 35% Co, on the other hand, amorphous $(FeCo)_{80}B$ alloys exhibit this peak at

about 15% Co [56]. The crystalline (bcc) Fe-Ni alloys also exhibit an initial increase in magnetization as nickel is added to iron and show a peak at about 7% Ni [73]. The peak in magnetization appears to be absent in $(FeNi)_{80}B$ amorphous alloy, and no magnetization peak is observed for phosphorus-rich mixed metalloid metallic glasses. The origin of these differences has not been examined and is not understood [56].

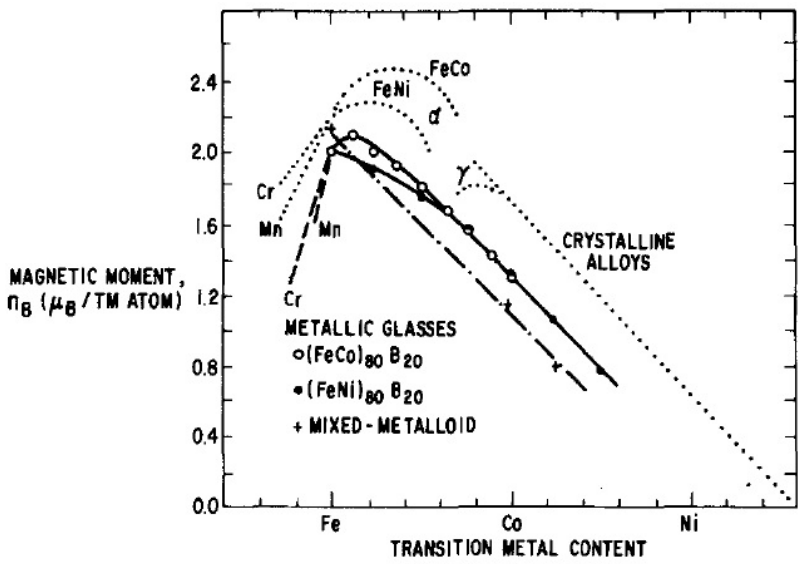

Figure 1.7: Magnetic moment per TM atom for $(FeCo)_{80}B_{20}$ and $(FeNi)_{80}B_{20}$ metallic glasses (solid line). Phosphorus-rich mixed metalloid metallic glasses (dot-dashed line) [68].

The magnetic moment is an important factor characterizing the magnetism of materials, and the saturation magnetization (M_s) value reflects the amount of total magnetic moment [63]. For the ferromagnetic materials the saturation induction, or the saturation flux density, B_s, can be expressed as [64]:

$$B_s = \mu_0 M_s$$

where μ_0 is permeability of vacuum, so the amount of total magnetic moment can reflect the saturation induction for ferromagnetic materials [63]. The average atomic magnetic moment, $\bar{\mu}$, per magnetic atom can be calculated using [65]:

$$\bar{\mu} = \frac{\sigma(0)M}{N\mu_B} X_{TM}^{-1}$$

where $\sigma(0)$ indicates the saturation magnetization of the alloy at temperature of 0 K, M denotes the molecular weight, N is the Avogadro number, μ_B is the Bohr magneton and X_{TM} is the atomic fraction of magnetic atoms [65].

In an amorphous ferromagnet the spins are all oriented in the same direction, but the topological arrangement of spins is not regular. Below the critical (Curie) temperature T_c, all the spins are, on the average, oriented parallel to one another, giving rise to a large spontaneous magnetization of the sample in some arbitrary direction if the system is isotropic. In real amorphous materials, there is always some anisotropy, although it may be weak, and the bulk magnetic moment $M(T)$ is oriented along one of the easy magnetization axes. The spontaneous magnetization decreases as the temperature rises, and, in the absence of an external magnetic field, disappears at the Curie temperature, in contrast with the prediction that a sharply defined transition temperature may not be defined in amorphous ferromagnets, because of the nonuniform distribution of magnetic atoms. Near the Curie temperature ($T \leq T_c$), the temperature dependence of the spontaneous magnetization is given by the expression [60]:

$$M(T) \cong const * \left(1 - \frac{T}{T_c}\right)^{\beta}$$

where β is the critical exponent and close to and close to 0.4, which value is normally a little larger than 0.36 given by the three-dimensional crystalline Heisenberg model. In the low-temperature region, i.e., for $T \rightarrow 0$, the temperature dependence of $M(T)$ has the power form given by [60]

$$M(T) = M(0)(1 - BT^{3/2} - CT^{5/2} - \ldots)$$

where $M(0)$ is the saturation magnetization and corresponds to complete alignment of moments. The values of B in amorphous ferromagnets are typically larger than those in related crystalline ferromagnets. This is understood to be a consequence of the chemical disorder (owing to the presence of metalloids) [62]. Above the Curie temperature ($T > T_c$), an amorphous ferromagnet behaves like a classical paramagnet and the spontaneous magnetization vanishes [60].

The Heisenberg model [74] considers ferromagnetism and the defining spontaneous magnetization to result from nearest neighbor exchange interactions, which act to align atomic moments (spins) in a parallel configuration [52, 53, 60]. The spins of the neighboring electrons are coupled by exchange forces, and in this way, all the spins are oriented in the same direction. This parallel alignment of the spins gives rise to a macroscopic magnetic moment [52]. The sum of spin-dependent exchange energy contributions can be expressed as [52, 60]:

$$H = -\frac{1}{2}\sum_{<i,j>} J_{ij}\, \tilde{S}_i \tilde{S}_j$$

where H is the Heisenberg Hamiltonian, $\tilde{S}_i$ and $\tilde{S}_j$ are the spin angular momenta of the two neighboring atoms and J_{ij} is the Heisenberg exchange coupling (exchange integral). If the exchange integral is positive, the lowest energy state results from parallel alignment of the spins, which is a necessary condition for ferromagnetism to occur [61]. If the exchange integral is negative (which is most commonly so), antiparallel alignment of the spins is energetically favorable. Such materials called antiferromagnets [52]. Exchange force is a consequence of the Pauli exclusion principle, applied to the two atoms as a whole. This principle states that two electrons can have the same energy only if they have opposite spins. In this case, two atoms can form a stable molecule, because for a certain interatomic distance the total energy of the atoms is less than any larger or smaller distances. (i.e.,

hydrogen molecule). On the other hand, if the spins are parallel (in the same direction), they will repel each other. That is, quantum-mechanical exchange forces depend on the relative orientation of the spins of the adjacent atoms. In other words, spin orientations apply a modification to classical electrostatic energy, which can be calculated by Coulomb's law. This indicates that, exchange force is fundamentally electrostatic [61].

The curve in Figure 1.8 shows the variation of the exchange integral with the ratio r_a/r_{3d}, where r_a is the atomic radius and r_{3d} is the radius of the 3*d* orbital [61]. The atom diameter is $2r_a$ and this is the interatomic distance, since the atoms of a solid are regarded as being in contact with each other. If two atoms of the same kind are brought closer and closer together but without any change in the radius r_{3d} of their 3*d* shells, the ratio r_a/r_{3d} will decrease. When this ratio is large, J_{ex} is positive but small, which means, the overlap between nearest neighbor d-orbitals is small. With further decrease in interspace, the ratio r_a/r_{3d} continues to decrease and the 3*d* electrons approach one another more closely. Consequently, positive exchange interaction, which is favoring parallel alignment of the spins first becomes stronger and then decreases to zero. If the interatomic distance decreases further, 3*d* electrons come together so close that they can only have antiparallel spins [61].

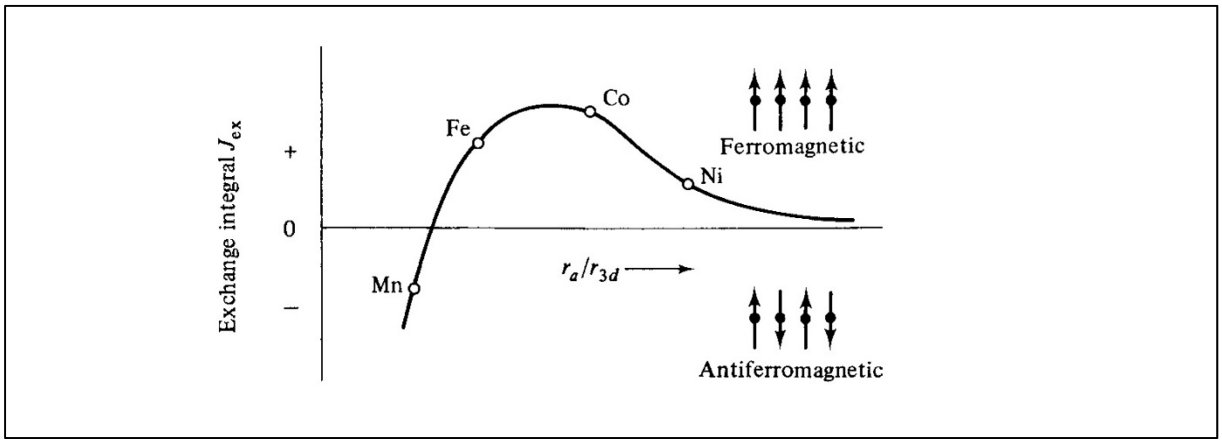

Figure 1.8: Bethe-Slater curve is an empirical description of the variations of the exchange energy with interatomic spacing [61].

When J_{ex} is positive, its magnitude is proportional to the Curie temperature, because spins which are held parallel to each other by strong exchange forces can be disordered only by large amounts of thermal energy. The positions of Fe, Co, and Ni on the curve agree with the fact that Co has the highest, and Ni the lowest, Curie temperature of the three [61]. The coupling of magnetic moments in amorphous magnets, as in most other magnetic materials, is due to the exchange interactions [56, 60]. The exchange is isotropic and depends on the distance between interacting atoms [60]. Only itinerant exchange between 3*d* moments is of importance in the transition metal-metalloid alloys [56]. Accordingly, the direct exchange interaction of amorphous magnets may be given by the semiempirical Bethe-Slater curves as a function of the radius of *d*-shell, R_{3d} and of the atomic separation, R ($=2r_a$) [53, 59, 60]. Despite their chemical and structural disorder, amorphous ferromagnets most often have a well-defined magnetic ordering Curie temperature, T_c [56]. However, the Curie temperatures of amorphous transition metal-metalloid alloys are always found to be significantly lower than those of the pure crystalline transition metals [56, 60]. This reduction of T_c in the amorphous alloys appears to be largely the result of chemical composition and/or chemical disorder [56]. The theoretical treatment of spin ordering in amorphous solids is a much more difficult problem than in

regular crystalline lattices and has not been satisfactorily solved. If the molecular field approximation is used, the Curie temperature can be expressed as [56]:

$$T_c = \frac{2S(S+1)}{3k}\sum_{ij} J_{ij}$$

where S is the atomic spin quantum number, k is Boltzmann's constant and J_{ij} is the exchange interaction between atoms at the position r_i and r_j and can be expressed in terms of the radial distribution function [56]. Chen et al. [76] showed that when T_c values of different glasses are plotted in the function of R/R_{3d}, the influence of metalloid addition and alloying among the transition metals on T_c in metallic glasses may be qualitatively explained in the framework of Bethe-Slater curves [60]. If iron lies in the region of positive $dJ(r)/dr$, the addition of a metalloid (with exception of phosphorus) which expands Fe-Fe interatomic distances raises T_c, while the increase in Co-Co and Ni-Ni pair distances lowers T_c [75]. Another model of Hasegawa and Ray [77] interprets the T_c in terms of a mean field theory which emphasizes the change in the coordination number of the magnetic species [62]. According to O'Handley [62, 78], the true determinant of T_c in $Fe_{100-x}M_x$ glasses is the short-range order (SRO) which includes both of these factors within a mean field theory.

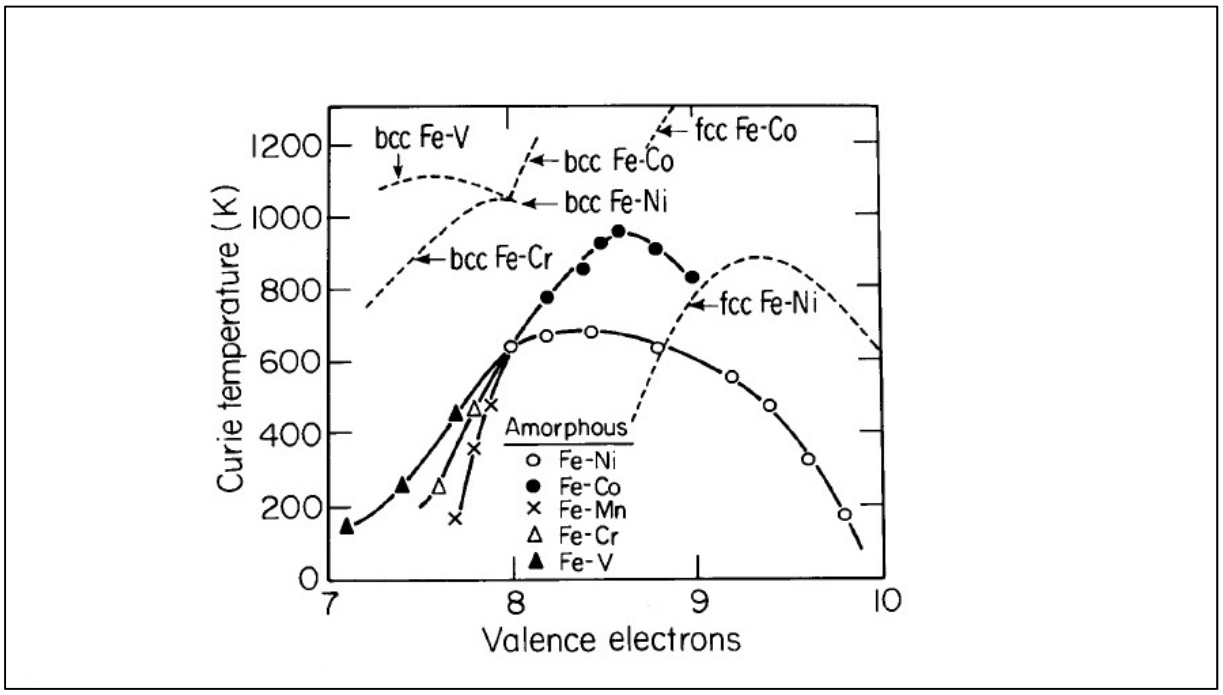

Figure 1.9: The curie temperatures of amorphous alloys of $(Fe_{1-x}TM_x)_{80}P_{10}B_{10}$ as a function of average TM valence electron concentration. Dashed line is data for crystalline alloys [62, 71].

Mizoguchi et al. [69] has reported T_c values for a wide range of transition metal amorphous alloys with the composition $(Fe_{1-x}TM_x)_{80}P_{10}B_{10}$. These are shown in Figure 1.9 plotted as a function of average outer electron concentration, together with the Curie temperatures of the corresponding transition metal crystalline alloys without the metalloids. The behavior of the Curie point is quite different from the crystalline alloys, suggesting the complexity of the effect of crystal structure on T_c [56, 71]. In the amorphous systems there are no discontinuities as found in crystalline alloys at phase boundaries and T_c is a smooth function of alloy composition over the entire range [56, 62, 69, 71]. The influence of alloy

constituents on T_c, is, however, complicated and is far from understood [75]. There exists no widely accepted, first-principle theory of Curie temperatures despite recent progress in this area [62].

An ideally homogeneous, isotropic amorphous alloy should have no macroscopic magnetic anisotropy [79]. However, real materials often fail to meet these conditions, and therefore magnetic anisotropic behavior is observed. Metallic glasses usually exhibit a small magnitude of magnetic anisotropy. Its origin is varied and sometimes not completely understood [56]. Since the magnetic anisotropy represents a barrier to switching the magnetization for soft magnetic materials, a small magnetic anisotropy is desired to minimize the hysteretic losses and maximize the permeability [53, 62]. The presumed isotropic character of the TM-M amorphous alloys had been predicted to result in very low coercivities and high permeabilities; all the desired properties of technological significance for application as soft magnetic materials [56]. On the atomic scale, however, magnetic anisotropy exists even in an ideally homogeneous amorphous alloy. Each magnetic ion experiences an anisotropic electric field or exchange field due to its neighboring ions. The magnitude and easy axis of this local anisotropy vary from site to site within the amorphous structure. In TM-M metallic glasses, the exchange interaction is much stronger than the local anisotropy, so that inside a domain all the spins are essentially parallel. In amorphous alloys containing rare-earth elements, the local anisotropy is often strong enough to prevent parallel alignment of spins, which gives rise to substantial coercivities [79].

Alben et al. [80] has presented a simple, quantitative and illuminating random local anisotropy model in describing the effective magnetocrystalline anisotropy in amorphous materials [53, 62, 78]. The random anisotropy model leads to a small effective magnetic anisotropy due to the statistical averaging of the magnetocrystalline anisotropy. In metallic glasses the idea of a crystal field is replaced by the concept of a short-range local field on the scale of several Å. The symmetry of the local field determines the local magnetic anisotropy and this symmetry depends on local coordination and chemical short-range order. The local anisotropy may be large but is averaged out due to fluctuations in the orientation of easy axes. The statistical averaging of the local anisotropy takes place over a length scale equivalent to the ferromagnetic exchange length, L_{ex} [53]. The short-range local field fluctuates over a characteristic distance d in metallic glasses. This distance is typically of the order 10 Å and it is expected that $L_{ex} > d$. The competing interactions in determining the orientation of the local magnetization are its exchange interaction J with its neighboring moments and its coupling D to the short-range local field anisotropy. In the case of most TM-M glasses, $D/J < 1$, which means that $L_{ex} \gg d$, so the magnetization tends to follow a fixed direction over a range much greater than the distance over which the local anisotropy direction changes [53, 62]. In other words, the magnetization does not respond to the local anisotropy because of the strong exchange coupling [78]. Thus, on macroscopic scale, the local anisotropy is averaged out to a small effective magnetocrystalline anisotropy [53, 62].

Magnetostriction is the process by which the shape of a ferromagnetic material changes during the process of magnetization as a result of magnetoelastic interactions [53]. Magnetostriction arises from the strain derivative of the magnetic anisotropy energy and hence reflects the same atomic-scale mechanisms that give rise to magnetic anisotropy. Since the amorphous alloys considered macroscopically isotropic, the magnetostriction is expressed by a single constant, the saturation magnetostriction, λ_s. Measured magnetostriction values in amorphous alloys are comparable to those in crystalline transition metals, generally 30 x 10^{-6} or less [62]. There exists a compositional dependence of magnetostriction in TM-M metallic glasses, and this dependence, except for cobalt-rich glasses, quite different from the behavior of comparable crystalline alloys. The greater disparity between the magnetostrictions of crystalline and amorphous phases of iron-rich alloys is probably related to the

greater difference in SRO between these two phases than between those of cobalt- or nickel-rich alloys.
This difference in SRO is also reflected in T_c [62]. In melt-quenched alloys, inhomogeneous stresses resulting from differential thermal contraction interact with the magnetostriction to cause local magnetic anisotropy. Nevertheless, this is a macroscopic effect and it tends to disappear as the alloy is homogenized structurally by thermal annealing below the crystallization temperature [56, 79]. This decrease in the strain-magnetostriction anisotropy results in the decrease in coercivity, H_c.

The amorphous alloys have very low DC coercive fields, often 0.8 A/m or less. This is attributed to their homogeneous structure, which lacks grain boundaries, dislocations or precipitate particles to act as pinning centers for domain walls [2, 79]. As is the case in crystalline alloys, the coercive field depends on the details of preparation, heat treatment, and it tends to a minimum value at the composition where the magnetostriction goes through zero, suggesting that the interaction of internal or external stresses with the magnetostriction largely governs H_c [79]. Another desired property of interest for the soft magnetism is the magnetic permeability, μ, the magnetic response function in an applied field, which usually is inversely related to the material's coercivity, H_c [53]. Generally, ferromagnetic metallic glasses exhibit high magnetic permeability, due to the absence of magnetocrystalline anisotropy [2]. In particular, alloys with small magnetocrystalline anisotropies and magnetostrictive coefficients result in small coercivities and large permeabilities, which give rise to particularly soft magnetic materials [53].

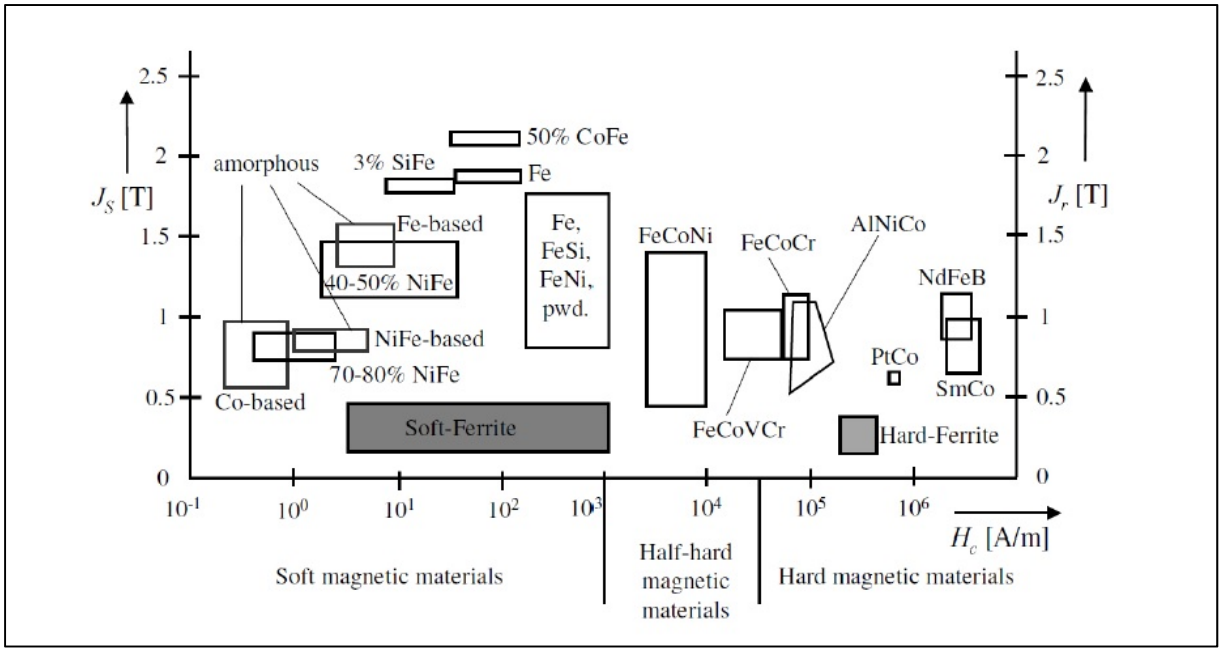

Figure 1.10: Classification of magnetic materials [2, 3].

Figure 1.10 shows a classification of the magnetic materials based on their coercivity, saturation polarization and remanence. The terms “hard” and “soft” magnets are used to distinguish ferromagnets based on their coercivity. As it can be seen, the soft magnetic materials have coercivity below 1 kA/m, while the hard magnets have the coercivity larger than 50 kA/m. The softest magnetic materials are the amorphous alloys [2].

1.5 Glass forming ability (GFA)

The ability of a metallic alloy to transform into the glassy state is defined as the glass-forming ability (GFA) [1, 4]. The GFA of alloys is determined both by structural and kinetic parameters [75]. While structural criteria deal with the geometrical arrangement of atoms, bonding and atomic size effects to predict glass formation, the kinetic criterion considers the rate of cooling relative to the kinetics of crystallization. Both the thermodynamic (structural) and kinetic factors assume importance. However, the basic GFA is mostly determined by structural parameters. This is where structural parameters such as the atomic size and chemical interactions between atoms are important. Once these criteria are satisfied, then the actual formation of the metallic glasses is determined by the kinetic parameters [1, 4]. The most basic criterion in prediction of the GFA of a system is the critical cooling rate, R_c, which is dependent on the alloy system and its composition. The lower the R_c, easier to obtain the glassy state of an alloy. It is a very effective indicator of the GFA; however, its measurement is an involved and time-consuming process. One must take a liquid alloy of a given composition, allow it to solidify at different cooling rates and individually determine the structure after each trial. The cooling rate just above which the metallic alloy melt has transformed into a glass is then designated as the R_c. Since it can only be determined if the system undergoes the glass transition, it is not a predictive criterion. For this reason, other simple and empirical criteria have been proposed to explain the glass formation [1, 4, 23].

Turnbull [22] had suggested that the reduced glass transition temperature, T_{rg}, which is the ratio of T_g to the liquidus temperature of the alloy T_l, should be a good indicator of the GFA of the alloy. In other words, the lower is T_l and the higher is T_g then the higher tends to be the GFA. His suggestion is based on the kinetics of crystal nucleation and the viscosity of melts. The higher the T_{rg} value, the higher the viscosity of the melt and therefore it is easier to obtain the glassy state at a low critical cooling rate. In other words, the lower is T_l and the higher is T_g then the higher tends to be the GFA [1-4, 34, 52, 62, 75]. Up to now, the Turnbull criterion for the suppression of crystallization in undercooled melts remains one of the best ‘‘rule of thumb’’ for predicting the GFA of any system [34].

It has been known that GFA is often associated with the eutectic phase diagram [1, 28 ,75 ,83]. Since the lowest T_l is desirable, it is not too surprising that in binary alloys of eutectic compositions it is easier to realize glass transition [22]. Thermodynamically, the liquid state is energetically preferred over the solid crystalline phases at the eutectic composition, either through the destabilization of the crystalline phases or through the stabilization of the liquid state [1]. Further, the driving force for the nucleation and growth of the crystalline phases below the eutectic temperature (which is the energy difference between the liquid and crystalline phases) is relatively small at the eutectic composition [1, 34, 79]. Since a number of crystalline phases compete with each other for nucleation and growth, the crystallization of the liquid requires extensive rearrangement of the different types of atoms to form the new phases, which means that, glass formation is kinetically also preferred at the eutectic composition [1, 84]. Therefore, an alloy with the eutectic composition, especially if it is a deep eutectic, will form the glassy phase most easily in the alloy system [1, 34, 62]. This is because with increasing solute content T_g changes slowly, but T_l decreases very rapidly as one approaches the eutectic composition. Accordingly, the T_{rg} value is high at the deep eutectic compositions [1, 4, 28, 34, 62, 81-86]. This empirical criterion has been most helpful in identifying glass-forming compositions in simple binary and ternary alloy systems in the early years of RSP research [1].

Metallic glasses produced by RSP methods can be traditionally described in two groups: Metal-metalloid and metal-metal types. It has been observed that for the metal-metalloid type, the best composition to form a glass contains about 80 at.% of the metal component and 20 at.% of the

metalloid component [1, 29, 56, 62, 69, 75, 79, 85, 86]. The requirement of the 20 at.% of the metalloid component is explained through the occupation of the empty spaces, which are inherent in Bernal dense random packed structure [1, 56, 69, 75, 79, 84-86]. The tetrahedron of four metals atoms is filled with a metalloid atom and this gives rise to an alloy composition of A_4B, where A and B represent the metal and metalloid atoms, respectively [1]. The most stable configuration corresponds to the situation when all the holes are filled, corresponding to about 20 at.%. This is near the eutectic composition of many of the alloys and is in the range of the stable glass compositions [56]. However, in metal tetrahedra's of the Bernal structure, neither the size of these voids (they were too small for any metalloid atom to occupy) , nor their concentration (holes of the required sizes) were found to be enough for a proper accommodation in observed glass compositions [1, 56, 75] . Thus, the real reason for the requirement of 20 at.% of metalloid atoms to form glasses is still not very clear [1].

Regardless of the actual size of the voids and whether the presumed model is valid or not, it is notable that the metal–metalloid-type binary phase diagrams exhibit deep eutectics at around a composition of 15–25 at.% metalloid [1]. For example, Fe-C, Fe-B, Fe-P, Au-Si and Pd-Si phase diagrams reveal a deep eutectic point at 15–25 at.% metalloid [1, 29]. It should also be noted that, the total concentration of metalloid additions in Fe based BMGs usually ranges from 17 at% to 25 at%, which is near the deep eutectic point with a low liquidus temperature T_l [29]. Therefore, the concepts of deep eutectics and structural models also seem to converge for (TM or noble) metal–metalloid type metallic glasses [1, 34, 56, 75].

In the case of BMGs, the criteria described for glass formation can not be used effectively. The problem arises from the complexity of the alloy systems and the absence of the phase diagrams for higher order alloys. Therefore, newer criteria have been proposed to explain glass formation in BMGs. Based on the extensive data generated on the synthesis of BMGs, Inoue summarized the results of glass formation in multicomponent alloys and proposed three empirical rules. These may be stated as follows [1-4, 29, 34, 52]:

- For mm-sized samples, the alloy must contain at least three components. The formation of glass becomes easier with an increasing number of components in the alloy system.
- A significant atomic size difference should exist between the constituent elements in the alloy. It is suggested that the atomic size differences should be above about 12% between the main constituent elements.
- There should be negative heat of mixing for the (major) constituent elements in the alloy system.

Considering these criteria, the first is based on the thermodynamic and kinetic aspects of glass formation, and the second on the topological aspects (structure and packing of atoms). The third criterion is essential for the mixing of atoms (alloying) to occur and for the formation of a homogeneous glassy phase [1, 4]. Any metallic liquid, which satisfies the three empirical rules, is expected to have a denser randomly packed atomic configuration, which results in extremely slow atomic mobility, thus making the redistribution of atoms on a large scale very difficult. Such kind of structure can effectively surpass the nucleation and growth of crystalline phase(s), which is equivalent to the increase in GFA of the glass-forming alloys [2, 34].

2. Experimental Details and Measurements

In this part, the experimental procedure involved in preparation techniques of the industrial grade low-cost soft-magnetic glass-forming alloys, post-characterization techniques such as, thermal, magnetic and morphological property measurement techniques are discussed.

2.1 Master alloy preparation

In order to prepare a high number of different master alloys used in this work, two different melting techniques, namely arc melting and induction melting were utilized. According to the ribbon casting results, the induction melting technique is chosen finally as the main production method. The reason behind this decision is related to the difficulties in the melting process of the FeP prealloy and to its overestimated amount of impurities. This pre-alloy was commercial raw, and its chemical analyses is given in Table 2.1. At the time the author started to produce the first eight master alloys, this analysis was unavailable, and the overall amount of impurities were assumed to be much higher. For this reason, several efforts have been made to purify the pre-alloy, by means of melting and solidifying multiple times, before using it as a constituent in a master alloy. After the arrival of the chemical analysis presented below, these steps were eliminated, and the pre-alloy was used directly as a phosphorus source for the next series of master alloys.

P	Cu	Ni	Mn	Al	Co	Si	C	S	Fe
23.23%	0.05%	0.36%	0.003%	0.005%	0.012%	0.005%	0.01%	0.011%	balance

Table 2.1: Chemical analysis of the commercial raw FeP prealloy.

The first six master alloys were prepared through the Edmund Bühler GmbH Arc Melter AM/0,5 casting device, which is depicted in Figure 2.1. During the preparation of the master alloys, the diffusion pump of the device was not activated, and in order to maintain the low vacuum level, only the rotary pump was used. Using this pump yields a vacuum of the several order of 10^{-3} mbar which takes approximately 15 minutes to achieve this vacuum value. These first six master alloy compositions were $Fe_{80}P_{13}C_7$ (MA-1, MA-2, MA-3, MA-4), $Fe_{57}Co_{23}P_{13}C_7$ (MA-5) and $Fe_{60}Co_{20}P_{13}C_7$ (MA-6). The first master alloy (MA-1) was prepared with pure iron flakes (99.99%), commercial raw FeP pre-alloy and graphite powder (99.99%). First, the given composition was converted from at.% to wt.%, and the calculated amounts of the ingredients were carefully weighed to make a total alloy mass of 20 g. Then, this mixture was placed into the copper heart of the arc melter, vacuumed down to 5.10^{-3} mbar, and subsequently melted through the electric arc under a titanium-gettered high purity argon atmosphere. However, during the melting process, the vacuum chamber of the arc melter became black and smoky, and moreover, small pieces from the alloy mass exploded and flew away.

These problems were interpreted to be resulting from the graphite powder and/or the impurities of the FeP pre-alloy. In order to verify this, MA-2 was prepared with the substitution of graphite powder by Fe_3C iron carbide granules (purity of 99+%). Nevertheless, the black smoke and the small pieces flying away were observed again. This raised the concerns about the possibility of a strong deviation from the glass forming composition, arising from the evaporation of the phosphorus and/or the impurities of the pre-alloy. Thus, ribbon casting attempts from these two master alloys have failed, and the author decided to substitute the commercial row FeP pre-alloy with a pure (Fe_2P, purity of 99+%) one for the next master alloys, in order to be sure about the actual phosphorus amounts in the alloys. With this substitution, no deviation was expected from the glass forming composition, since the pre-alloy was pure, and it would be possible to melt it down completely with the arc melter, which operates at temperatures up to 3773 K. Accordingly, MA-3 (10 g), MA-4 (10 g), MA-5 (25 g, with 99.99% Co) and MA-6 (25 g, with 99.99% Co) were prepared with the previous iron and carbon sources (pure Fe_3C as carbon source) and pure Fe_2P prealloy. As expected, the problems which had been observed before were not present during the preparation of these new master alloys.

Despite the fact that only pure alloy constituents were used, due to the lack of experience of the author as a casting operator, and general difficulties in obtaining Fe-based amorphous ribbons, only two of the casting operations were resulted in glassy samples. MA-3 ($Fe_{80}P_{13}C_7$) and MA-6 ($Fe_{60}Co_{20}P_{13}C_7$) were the master alloys of these first glassy ribbons, which will be shown later. Although these master alloys were prepared only with pure constituents and melted with an arc melter, the casting results were largely unsuccessful. Hence, the author decided to change the type of the melting process to induction melting

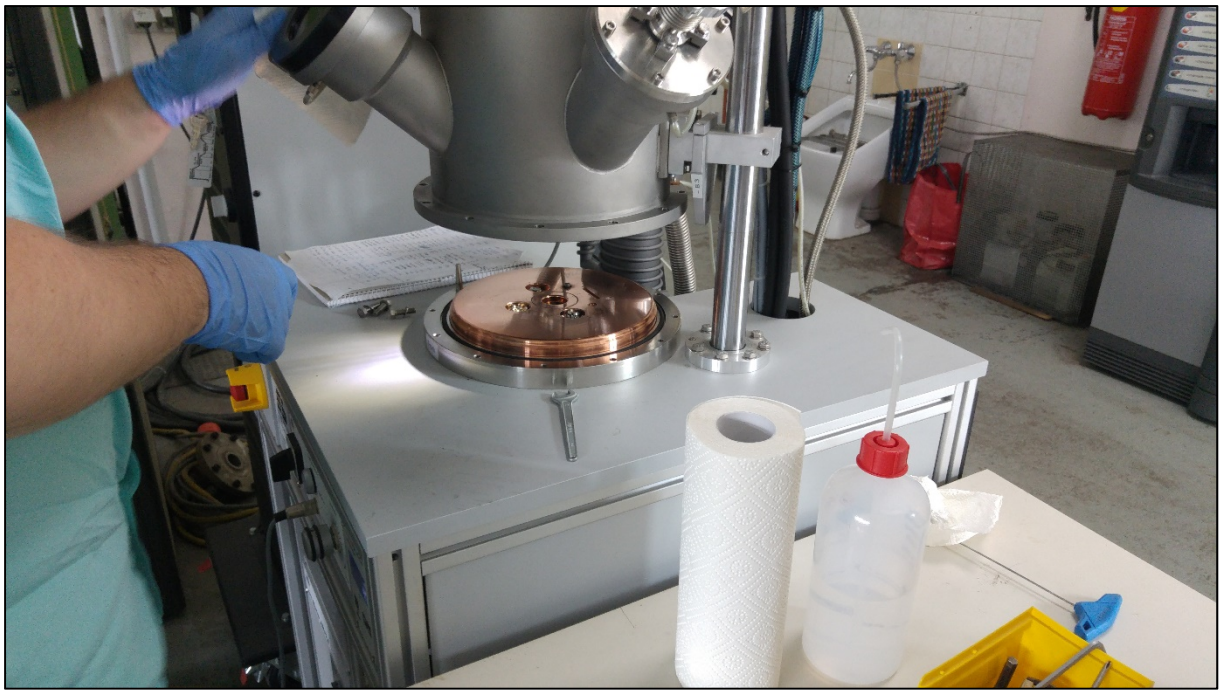

Figure 2.1: An image of the arc melter device used in this work.

to melt commercial raw FeP pre-alloy properly. With induction melting, the alloy constituents were not exposed to high temperatures of an electric arc. Instead, the maximum operating temperature of the melt spinner was kept below 1973 K. The author has temporarily changed the setup of the Edmund Bühler GmbH Melt Spinner HV device into an induction melter with the help of an aluminium cantilever attached on an aluminium platform. When this platfom was placed inside the large vacuum chamber of the melt spinner at a correct angle, L-shaped cantilever was providing a small platform, which was suitable to place the alumina crucible into the interior space of the induction coils. The height of the crucible (the filled part of the crucible had to be approximately the middle of the coil cylinder) was adjustable via adding or removing some small pieces of refractory material between the crucible and the aluminium platform. An image of this setup is shown in Figure 2.2.

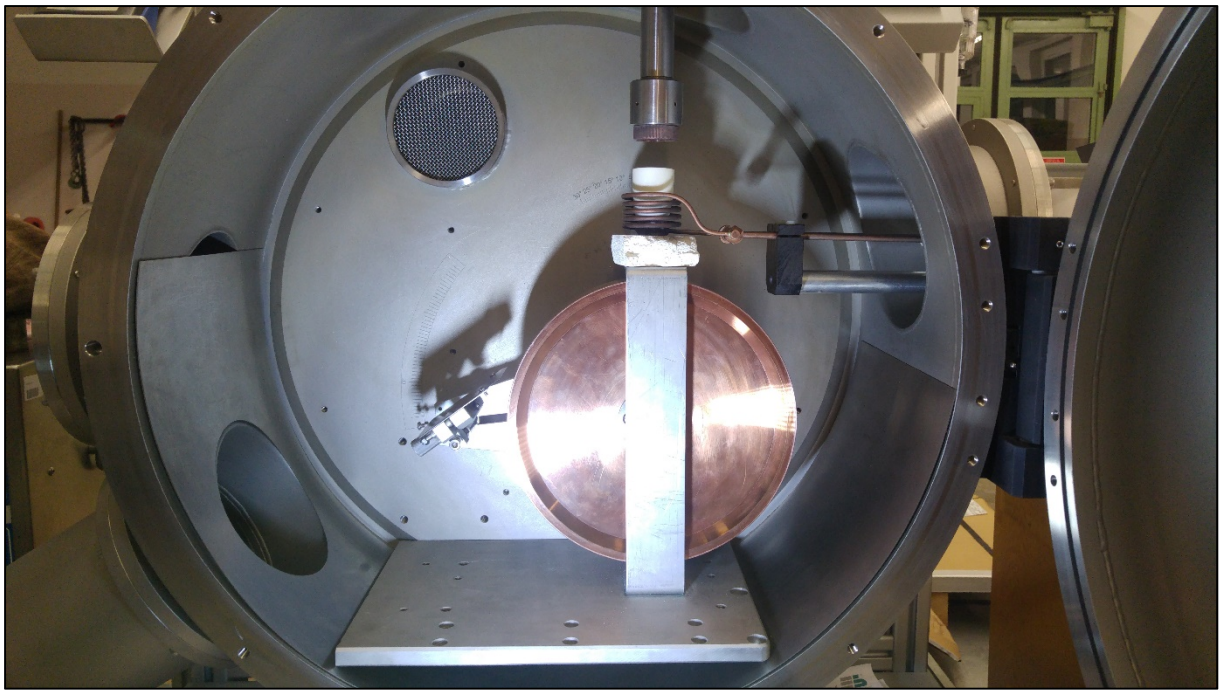

Figure 2.2: The setup used for induction melting of the master alloys in this work.

Before this setup was realized, the author had already prepared the 20g of MA-7 with a composition of $Fe_{65}Ni_{15}P_{13}C_7$ via induction melting and standard quartz tubes of the device. The alloy components of this master alloy were pure iron flakes (99.99%), pure nickel flakes (99.99%), commercial raw FeP pre-alloy and Fe_3C iron carbide granules (99+%). However, as mentioned before, the author had concerns about amount of the impurities in the industrial grade pre-alloy. Thus, the pre-alloy was re-melted four times with an induction melter up to 1973 K in a standard quartz crucible of the melt spinner (quartz tube for ribbon casting) to 'purify' it to some extent before using it as a component. After these steps, the alloy was melted with the induction melter up to 1523 K in a standard quartz crucible. Since it is rather low temperature for FeP pre-alloy (e.g., Fe_2P has a melting temperature of 1643 K), the master alloy was re-melted three more times with the arc melter for enhanced homogeneity. As mentioned before, all of these re-melting, solidifying and master alloy preparation steps were performed only with the rotary pump of the devices, which means low vacuum conditions ($<10^{-4}$ mbar) were realized prior to flushing the vacuum chambers of the devices with high purity argon. Despite these efforts, it was not possible to cast fully amorphous ribbons from this master alloy.

MA-8 was prepared with a composition of $Fe_{60}Ni_{10}Co_{10}P_{13}C_7$ (25g, with 99.99% Co) and melted in an alumina (Al_2O_3) crucible using the melt spinners induction melter and the setup explained above. The rest of the alloy components were same as MA-7, but this time the industrial grade FeP pre-alloy was melted up to 1773 K twice before using it as an alloy component. Two ribbon casting attempts from this master alloy were successful, and this was the last master alloy produced without the knowledge of chemical analysis of the FeP pre-alloy shown in Table 2.1. At the same time, the author has also received the chemical analysis of an industrial grade NiP pre-alloy from the same company, and used this pre-alloy as nickel and phosphorus source for two master alloys, namely MA-9 (25g, with 99+% Fe_3C) and MA-13 (25g, with 99.9% graphite powder) with the same composition of $Fe_{50}Ni_{30}P_{13}C_7$. The NiP pre-alloy was directly used as an alloy component, and these master alloys were also prepared in melt spinner with the same setup and under the same conditions. However, it was not possible to produce any glassy ribbons from MA-9. On the other hand, MA-13 was not used at all, due to the exclusion of this composition from the studied alloys. For this reason, the chemical analysis of the

industrial grade NiP prealloy is not given in details. The remaining master alloys were all prepared with the same technique and the components above mentioned, namely, as phosphorus source the as-received industrial grade FeP pre-alloy, and as carbon source Fe_3C iron carbide granules or graphite powder were used. These master alloys had a total mass of 25 g, and most of them completely consumed during various casting trials with different parameters. Their compositions are; MA-10 ($Fe_{60}Ni_{10}Co_{10}P_{13}C_7$), MA-11 ($Fe_{60}Ni_{20}P_{13}C_7$), MA-12 ($Fe_{60}Co_{20}P_{13}C_7$), MA-14 ($Fe_{60}Ni_{15}Co_5P_{13}C_7$), MA-15 ($Fe_{60}Co_{15}Ni_5P_{13}C_7$), MA-16 ($Fe_{60}Co_{20}P_{13}C_7$), MA-17 ($Fe_{80}P_{13}C_7$), MA-18 ($Fe_{60}Ni_{20}P_{13}C_7$), MA-19 ($Fe_{60}Ni_{10}Co_{10}P_{13}C_7$).

2.2 Fluxing process

In order to increase the number of the glassy samples obtained, fluxing treatment was performed to MA-9, MA-10, MA-11, MA-12, MA-14, MA-15, MA-16, MA-17, MA-18 and MA-19. The treatments were conducted with the induction melter of the melt spinner. As a fluxing agent, B_2O_3 (99.99%) powder was used. Small pieces (~4-5g) of each master alloy were put into alumina crucibles, they were completely covered with B_2O_3 and after flushing the chamber twice with high purity Ar, they were heated up to ~1473 K under 10^{-1} mbar vacuum.

The most important issue is to maintain the same temperature during fluxing process, which usually takes between 4.5 to 10 hours [1, 5-14, 18, 90]. However, during the melting of the master alloys, B_2O_3 was producing a thick foam-like layer, and this layer was greatly deteriorating the temperature measuring capability of melt spinner's infrared pyrometer. The values were fluctuating largely, and they were quite lower than expected. Since it was very difficult the regulate the temperature, we relied on the voltage values, which corresponded to the necessary temperatures based on previous experiences on master alloy melting and ribbon casting processes. Furthermore, in order to not to cause any possible damage to the melt spinner device, the overall duration of the fluxing process is decreased to 1 hour and 15 minutes. In Figure 2.3, the first setup used for fluxing and the foam-like layer above mentioned are depicted.

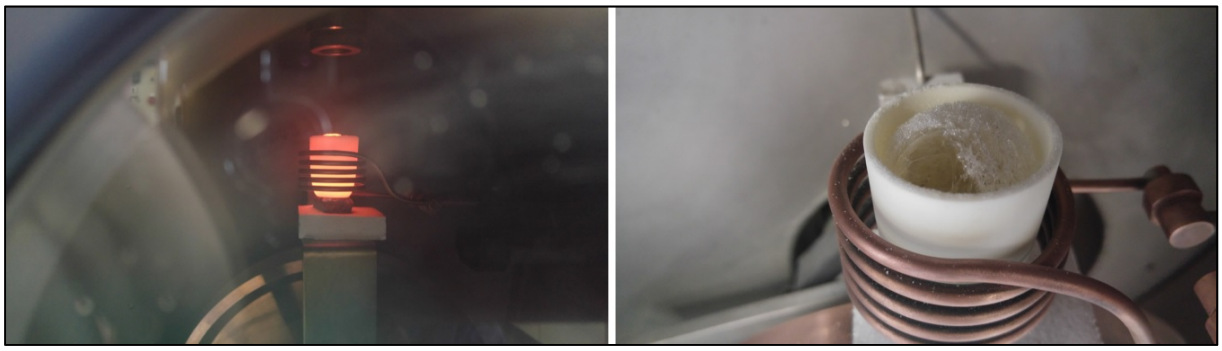

Figure 2.3: The first setup used for fluxing treatment and the foam-like B_2O_3 glass layer.

Other than alumina crucibles, standard quartz crucibles were also tried. However, the second setup had the same problem as the first one, that is, the process temperature was only estimated through the generator voltage applied. Nevertheless, in both setups the pieces of the master alloys melted successfully and soaked completely in the liquid oxide, and eventually 10 small ingots of 10 different master alloys were obtained. Since each fluxed small piece is corresponding to the mass necessary for one ribbon casting attempt, the author initially consumed the unfluxed master alloy (~20g) in order to

determine the best casting parameters, and after that, used the remaining fluxed small piece while expecting to achieve a successful ribbon production. Out of 10 fluxed small master alloy pieces 10 ribbon casting attempts have been made, and 3 of these attempts were resulted with amorphous ribbons. Two of these master alloys, which are MA-9 ($Fe_{50}Ni_{30}P_{13}C_7$) and MA-12 ($Fe_{60}Co_{20}P_{13}C_7$), rendered unsuccessful results, that is, casting trials with neither fluxed nor unfluxed master alloys did end up with amorphous ribbons.

2.3 Ribbon casting process

In this part, a large number of casting experiments were conducted with the melt spinner. All of the master alloys, with an exception of MA-13 ($Fe_{50}Ni_{30}P_{13}C_7$), has been used only for ribbon casting trials. Most of them were completely consumed, on the other hand some remaining master alloys were preserved for possible bulk-sized rod producing opportunities. The author has failed to synthesize any glassy ribbons from some of the master alloys, e.g., MA-1 ($Fe_{80}P_{13}C_7$), MA-2 ($Fe_{80}P_{13}C_7$), MA-4 ($Fe_{80}P_{13}C_7$), MA-5 ($Fe_{57}Co_{23}P_{13}C_7$), MA-7 ($Fe_{65}Ni_{15}P_{13}C_7$), MA-9 ($Fe_{50}Ni_{30}P_{13}C_7$) and MA-12 ($Fe_{60}Co_{20}P_{13}C_7$), even though they have been tried a number of times with different spinning parameters. The failed results were mostly consisted of partially welded, very brittle, entangled ribbon-like metallic bundles. On the other hand, in some cases, the as cast samples used to have a uniform ribbon form and they were not entangled, but they were only partially amorphous.

All casting trials, including the unsuccessful attempts, were realized under high purity argon atmosphere, after flushing the vacuum chamber of the melt spinner twice with argon and going down to a vacuum level of ~5.10^{-3} mbar measuring only the rotary pump of the device. For each casting event, a small piece (4-5g) of a master alloy was put into a standard quartz crucible, whose tip was grinded carefully to make a circular nozzle tip to facilitate the molten alloy pour onto the fast-rotating copper wheel. Since this grinding process had to be made by hand, and the main concern was to make the grinded area parallel to the copper wheel surface, the diameter of these holes ranged between ~1 to ~1.5 millimeters. A schematic illustration of the melt spinner is shown in Figure 2.4. After placing the small quantity of master alloy, with the help of the rotary pump, the air inside the vacuum chamber was evacuated to10^{-3} mbar. Following this, the flushing with high purity argon steps are taken, and after each flushing event the chamber was evacuated again with the rotary pump up to 10^{-3} mbar. After these steps, high purity argon was given to the chamber, and an ejection pressure difference was realized between the main vacuum chamber and external over pressure chamber.

The master alloy piece then heated up inductively to the desired casting temperature with the help of a high-frequency generator. At this point, the author pressed the casting button and let the molten alloy leave the crucible with the help of Ar gas coming out of the high-pressure chamber through the nozzle. The ejected molten alloy solidified it at a rate of 10^5-10^6 K/s. However, in very few cases did the molten alloy completely leave the quartz crucible, but most of the time there was a remaining piece (1-1.5g) solidified inside the crucible. In most of the attempts, the distance between the nozzle in the casting position and the wheel was 1 mm, and the ejection pressure of the Ar gas was 300 mbar. The angular frequency of the copper wheel was mostly 40 Hz, corresponding to a velocity of 31,416 m/s. According to the results, these parameters were slightly changed by the author, with an intention of obtaining a decent ribbon form, since this is the main indicator of an amorphous structure.

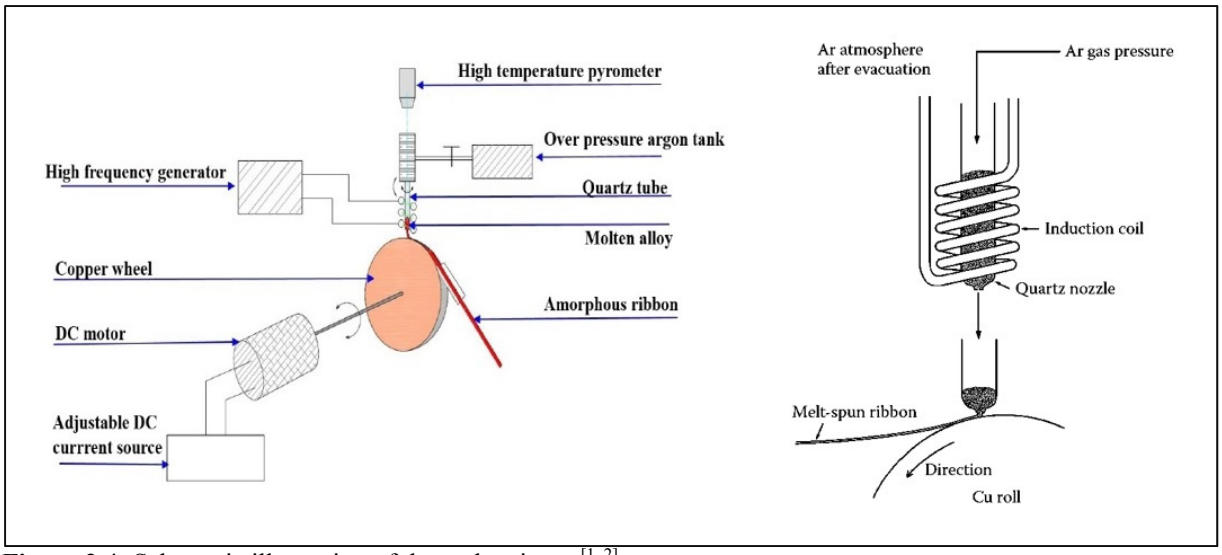

Figure 2.4: Schematic illustration of the melt spinner [1, 2].

The most important parameter of the casting process is the casting temperature, since this is directly related to the viscosity of the molten alloy. In general, exceeding the melting temperature about 150-200 K [2] is enough to eject the molten alloy, however, this was not the case in this work. For this reason, first of all the author has tried to determine the optimum casting temperature. For instance, if the casting temperature was too low, the molten alloy did not leave the crucible at all, because the viscosity was too high. Similarly, if the casting temperature was too high, then the alloy did completely leave the crucible, however it was solidified into small droplet-like splashed metal pieces, not shaping a ribbon form. For this reason, after determining the optimum casting temperature for each alloy individually, other parameters mentioned above were changed slightly in order to obtain the best ribbon form.

In Table 2.2, all of the 26 amorphous ribbons have been produced in this work are shown. Each color represents a particular composition. The master alloys are also grouped by their melting technique and P and C sources. Three of these ribbons were synthesized from fluxed master alloy pieces that mentioned in Chapter 2.2. Other process parameters and overall uniformity of the ribbons can also be seen from the table. For further investigations on thermal, crystallization and magnetic properties of the alloys, 9 of these ribbons are selected, and 3 of them were cast from fluxed master alloys

Master Alloy of the Ribbon	P and C Sources	Casting Temp.	Wheel Speed	Fluxed	Unfluxed	Uniformity	Vacuum [mbar]	DSC	VSM
MA-3 ($Fe_{80}P_{13}C_7$)	pure Fe_2P / Fe_3C / Arc Melter (high vacuum)	1473 K	40 Hz	NA	yes	moderate	Diffusion (10^{-6})	1473 K	
MA-6 ($Fe_{60}Co_{20}P_{13}C_7$)	pure Fe_2P / Fe_3C / Arc Melter (high vacuum)	1273 K	40 Hz	NA	yes	good	Rotary (10^{-3})	1473 K	
MA-8 ($Fe_{60}Ni_{10}Co_{10}P_{13}C_7$)	at 1500 °C induction remelted ind. grade-FeP / Fe_3C / Induction Melting	1248 K	40 Hz	NA	yes	bad	Rotary (10^{-3})		
MA-8 ($Fe_{60}Ni_{10}Co_{10}P_{13}C_7$)	at 1500 °C induction remelted ind. grade-FeP / Fe_3C / Induction Melting	1273 K	40 Hz	NA	yes	good	Rotary (10^{-3})	1473 K	
MA-10 ($Fe_{60}Ni_{10}Co_{10}P_{13}C_7$)	as received ind. grade-FeP / Fe_3C / Induction Melting	1283 K	35 Hz	-	yes	bad	Rotary (10^{-3})		
MA-10 ($Fe_{60}Ni_{10}Co_{10}P_{13}C_7$)	as received ind. grade-FeP / Fe_3C / Induction Melting	1298 K	35 Hz	-	yes	moderate	Rotary (10^{-3})		
MA-11 ($Fe_{60}Ni_{20}P_{13}C_7$)	as received ind. grade-FeP / Fe_3C / Induction Melting	1273 K	30 Hz	yes	-	good	Rotary (10^{-3})	1473 K	yes
MA-14 ($Fe_{60}Ni_{15}Co_5P_{13}C_7$)	as received ind. grade-FeP / Fe_3C / Induction Melting	1298 K	40 Hz	-	yes	good	Rotary (10^{-3})	1473 K	yes
MA-15 ($Fe_{60}Co_{15}Ni_5P_{13}C_7$)	as received ind. grade-FeP / Graphite / Induction Melting	1298 K	40 Hz	-	yes	good	Rotary (10^{-3})		
MA-15 ($Fe_{60}Co_{15}Ni_5P_{13}C_7$)	as received ind. grade-FeP / Graphite / Induction Melting	1323 K	40 Hz	-	yes	good	Rotary (10^{-3})	1473 K	yes
MA-15 ($Fe_{60}Co_{15}Ni_5P_{13}C_7$)	as received ind. grade-FeP / Graphite / Induction Melting	1348 K	40 Hz	-	yes	good	Rotary (10^{-3})	1473 K	
MA-15 ($Fe_{60}Co_{15}Ni_5P_{13}C_7$)	as received ind. grade-FeP / Graphite / Induction Melting	1373 K	40 Hz	-	yes	good	Rotary (10^{-3})		
MA-15 ($Fe_{60}Co_{15}Ni_5P_{13}C_7$)	as received ind. grade-FeP / Graphite / Induction Melting	1323 K	40 Hz	yes	-	good	Rotary (10^{-3})	1473 K	yes
MA-16 ($Fe_{60}Co_{20}P_{13}C_7$)	as received ind. grade-FeP / Graphite / Induction Melting	1423 K	40 Hz	-	yes	good	Rotary (10^{-3})	1473 K	yes
MA-16 ($Fe_{60}Co_{20}P_{13}C_7$)	as received ind. grade-FeP / Graphite / Induction Melting	1473 K	40 Hz	-	yes	good	Rotary (10^{-3})		
MA-16 ($Fe_{60}Co_{20}P_{13}C_7$)	as received ind. grade-FeP / Graphite / Induction Melting	1468 K	50 Hz	-	yes	good	Rotary (10^{-3})		
MA-17 ($Fe_{80}P_{13}C_7$)	as received ind. grade-FeP / Graphite / Induction Melting	1298 K	40 Hz	-	yes	good	Rotary (10^{-3})	1473 K	yes
MA-17 ($Fe_{80}P_{13}C_7$)	as received ind. grade-FeP / Graphite / Induction Melting	1323 K	40 Hz	yes	-	good	Rotary (10^{-3})	1473 K	yes
MA-18 ($Fe_{60}Ni_{20}P_{13}C_7$)	as received ind. grade-FeP / Graphite / Induction Melting	1348 K	50 Hz	-	yes	good	Rotary (10^{-3})		
MA-18 ($Fe_{60}Ni_{20}P_{13}C_7$)	as received ind. grade-FeP / Graphite / Induction Melting	1473 K	50 Hz	-	yes	good	Rotary (10^{-3})		
MA-18 ($Fe_{60}Ni_{20}P_{13}C_7$)	as received ind. grade-FeP / Graphite / Induction Melting	1473 K	40 Hz	-	yes	good	Rotary (10^{-3})	1473 K	yes
MA-19 ($Fe_{60}Ni_{10}Co_{10}P_{13}C_7$)	as received ind. grade-FeP / Graphite / Induction Melting	1298 K	40 Hz	-	yes	good	Rotary (10^{-3})	1473 K	
MA-19 ($Fe_{60}Ni_{10}Co_{10}P_{13}C_7$)	as received ind. grade-FeP / Graphite / Induction Melting	1323 K	40 Hz	-	yes	good	Rotary (10^{-3})		
MA-19 ($Fe_{60}Ni_{10}Co_{10}P_{13}C_7$)	as received ind. grade-FeP / Graphite / Induction Melting	1373 K	40 Hz	-	yes	good	Rotary (10^{-3})		
MA-19 ($Fe_{60}Ni_{10}Co_{10}P_{13}C_7$)	as received ind. grade-FeP / Graphite / Induction Melting	1423 K	40 Hz	-	yes	good	Rotary (10^{-3})		
MA-19 ($Fe_{60}Ni_{10}Co_{10}P_{13}C_7$)	as received ind. grade-FeP / Graphite / Induction Melting	1458 K	40 Hz	-	yes	good	Rotary (10^{-3})	1473 K	yes

Table 2.2: All the amorphous ribbons that have been produced in this work, their master alloys and casting parameters. The highlighted ribbons are going to be explained thoroughly in Chapter 3.

2.4 X-ray diffraction

All the synthesized samples, which possess more or less a ribbon form, are subjected to X-ray diffraction (XRD) analysis in order to determine whether their as-cast structures are glassy or not. These were performed in reflection configuration (D2 phaser – Bruker) using Co-K_α (λ = 1.7089 Å) radiation. The diffraction patterns were recorded between 20° and 120° (2θ) in a step mode, with a step size of $\Delta(2\theta) = 0.02°$. For this analysis, two samples for each ribbon were prepared, namely: one sample for the air side, and the other sample for the wheel side of the ribbons, considering the difference in their rate of cooling. Only after the both sides are identified as amorphous, a ribbon is accepted as a glassy one. All the ribbons presented in Table 2.2 were subjected to this analysis.

For further experiments, 9 of them (as discussed further in the next section) were selected and these ribbons were non-isothermally annealed according to their differential scanning calorimeter (DSC) curves, which means, up to the temperatures slightly exceeding their crystallization peak temperatures. In order to identify these crystallization products, each of these as cast ribbons is annealed according to its DSC trace, and after each annealing step, the sample was subjected to XRD analysis. This led to a sum of 28 diffraction patterns from these 9 selected ribbons, and all these patterns are investigated in order to identify the crystallization products and the crystallization sequence. For these XRD analyses, the same device and the parameters above mentioned were used. All these patterns will be shown in the third chapter in details.

2.5 Differential scanning calorimeter

A computer-controlled differential scanning calorimeter was used in order to determine glass transition, crystallization and melting points of the glassy samples. The tests were conducted using a Netzsch DSC 404 F1 Pegasus device under argon atmosphere at a constant heating and cooling rate of 20 K/min. Alumina (Al_2O_3) crucibles were used for all experiments, and for high temperature measurements up to 1200°C also Y_2O_3 powder was placed inside the bottom of the Al_2O_3 crucible to prevent any possible reaction between the sample and the crucible. 14 of 26 glassy ribbons in Table 2.2 were subjected to high temperature measurements, where they were heated up to 1200°C twice, with an aim of normalization by subtracting the baseline from the original heating curve. For these experiments the sample weight was selected to be 14 mg ± 1 mg. The glass transition temperature T_g, crystallization temperature T_x and liquidus temperature T_{liq} were determined from the onsets of the respective peaks, using the two-tangent method of the software.

For further experiments selected 9 ribbons were exposed to crystallization annealing, as mentioned in previous section. In order to ascertain their crystallization patterns, some of them were heated up to 973 K; nevertheless the resulting traces were same as the ones previously obtained. All the selected ribbons, except MA-16 ($Fe_{60}Co_{20}P_{13}C_7$), were heated up to beyond their crystalline state Curie temperatures, T_{cx}. These experiments were implemented with sample weights of 20 ± 1 mg, they were heated up once with a heating rate of 20 K/min and subsequently cooled down with the cooling rate of 20 K/min. Since no melting is expected, no Y_2O_3 was put into alumina crucibles to prevent possible reactions. These DSC curves of the selected non-molten 9 ribbons will be shown in detail in the third chapter.

2.6 Vibrating sample magnetometer

In order to obtain the room temperature saturation magnetization and coercivity values of the 9 selected ribbons, the author visited Vienna University of Technology (TU Wien) and conducted a series of experiments in the Institute of Solid State Physics with kind permission of Prof. Michael Reissner. These experiments were performed using a Physical Property Measurement System (PPMS 6500) by Quantum Design Inc. in vibrating sample magnetometer (VSM) mode. Small pieces of the ribbons were carefully weighed, and then placed onto a quartz sample holder with the help of a high vacuum grease. The samples were vibrated continuously up and down inside the pickup coil with a DC field varying between -10 kOe to 10 kOe. The details of the VSM setup can be found elsewhere [2, 3].

For the coercivity measurements, applied magnetic field was scanned between -100 Oe and +100 Oe. Even with 1 Oe increments, the devices resolution was insufficient to measure the coercivity of the soft magnetic ribbons. For this reason, only the magnetic moments of the 9 selected ribbons were recorded. From these values, using the calculated volumes of the samples, the magnetic polarization of the ribbons was calculated. The influence of the demagnetizing field has been neglected. The obtained hysteresis curves of the samples will be shown in detail in the next chapter.

3. Results and Discussion

In this chapter, the results of the experiments of 9 selected ribbons subjected to further investigations are going to be presented and the interpretation of the results are going to be made. As seen from the Table 2.2, all these ribbons were cast in a low vacuum environment and only commercial grade raw materials were used in the preparation of their master alloys. The reason behind this decision is to be able to realize the industrial manufacturing conditions and to reduce the production costs, since the necessity of high purity starting materials and/or high vacuum levels are the most important constraints on the large-scale industrialization of the MGs. [1, 9, 29, 101, 103]. As a result, cost-effective mass production with commercial raw materials under low vacuum conditions should be the first consideration for the extensive application of the MGs.

3.1 MA-17 ($Fe_{80}P_{13}C_7$)

This ribbon belongs to the starting composition of $Fe_{80}P_{13}C_7$ cast at 1298 K. The details of its master alloy (MA-17) and other casting parameters can be found in Table 2.2. An overall image of the glassy ribbon is shown in Figure 3.1.

Figure 3.1: Overall view of MA-17 ($Fe_{80}P_{13}C_7$) metallic glass ribbon.

Since only a low vacuum condition prior to casting atmosphere of high-purity argon was realized, the presence of oxygen in the amorphous ribbon is expected [1, 3, 9, 29, 101]. Moreover, due to the melting technique used for the master alloy, the low vacuum environment prior to melting process, and the non-gettered argon atmosphere during the melting event, it is highly possible that the master alloy also contains some amount of oxygen, either dissolved in the alloy or as oxides.

It is widely accepted [1, 3, 9, 29, 101-104] that the oxygen contamination severely deteriorates the GFA of the alloys, since most of the Fe-based alloys have a strong affinity with oxygen. Thus, the resulting oxides might induce the heterogeneous nucleation of the primary crystalline phase, or oxygen can change the

competing phase to a more quickly precipitating one, or they can destabilize the undercooled liquid by changing the crystallization process from a single to multiple staged one.

However, it has also been observed [3, 9, 29, 101-105] that oxygen presence can also have positive effects on GFA. Oxygen atoms can act as an alloying element, and since they are small and have a larger negative heat of mixing with other constituents, they tighten the dense random packed structure and stabilize the undercooled liquid by decreasing the liquidus temperature [29, 102, 103]. Moreover, Yang et al. [9] has reported that, oxygen can act as an impurity scavenger during the preparation of $Fe_{80}P_{13}C_7$ BMGs, by the synergistic reaction between oxygen and the impurities from industrial raw starting materials, the purification of the alloy melt occurs with the driving force of flotation of oxide inclusions.

In Figure 3.2, the high temperature DSC trace of the $Fe_{80}P_{13}C_7$ ribbon is depicted. The DSC trace is measured at 20 K/min and shows clearly the glass transition event, T_g, the supercooled liquid region, *SCLR* ($\Delta T_x = \Delta T_{x1} - T_g$), Curie temperature in amorphous state, T_c, as well as in crystalline states, T_{cx1} and T_{cx2}, and the two-staged crystallization event, T_{x1} and T_{x2}. Even though one subsidiary and one large exothermic peak is quite often observed [7, 9, 11, 12, 16, 63, 106-111] at different rates of heating for this composition, Yang et al. [9] has reported that this composition may also show single crystallization peak

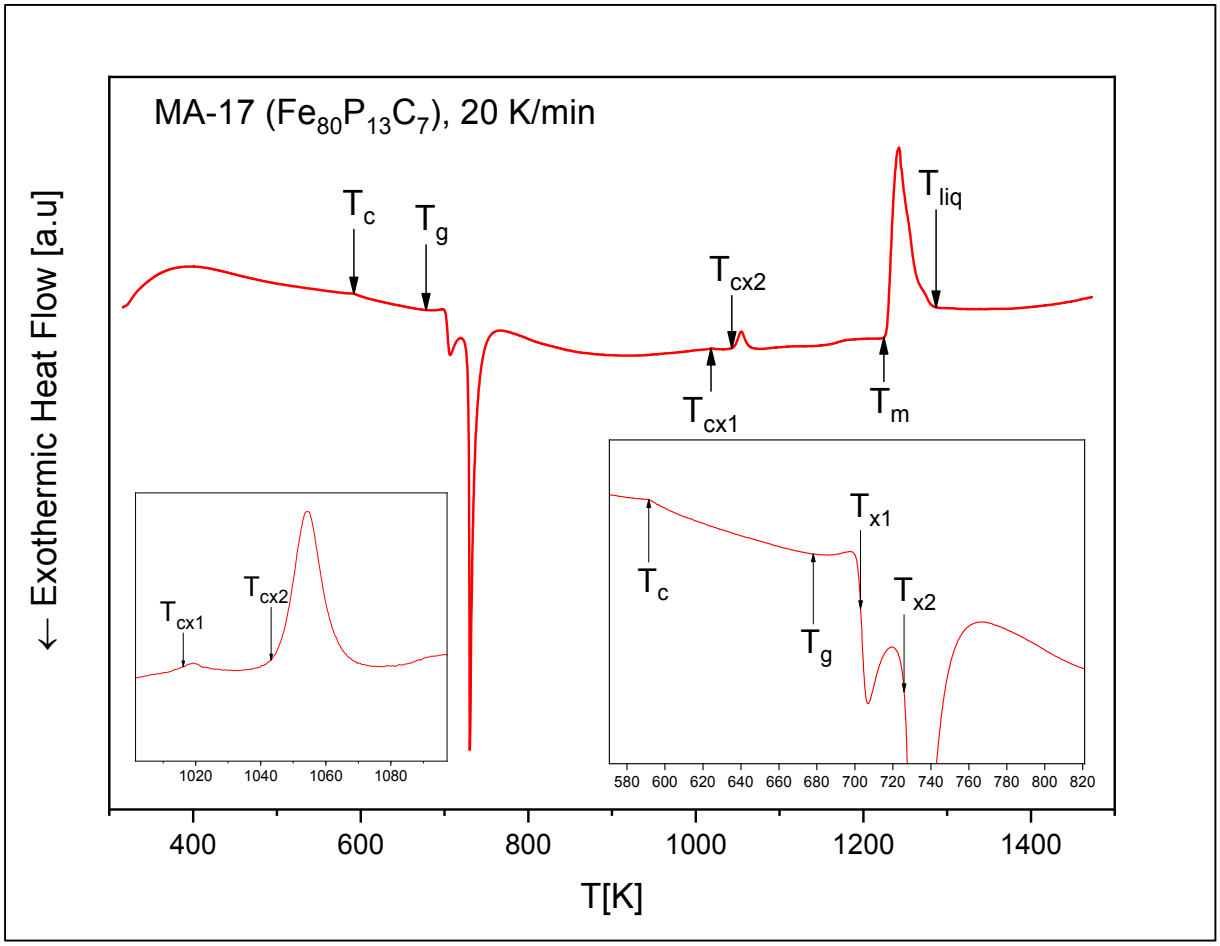

Figure 3.2: DSC trace of as-cast MA-17 ($Fe_{80}P_{13}C_7$) glassy ribbon. The insets show the enlarged regions of the same curve.

if the starting materials are industrial grade. Therefore, it can be assumed that the DSC trace of the base alloy coincides quite well with the literature. From the DSC trace one can see that for this alloy eutectic crystallization does not occur, and the equilibrium phases are formed in two stages. T_g, T_{x1}, T_{x2}, T_{cx1}, T_{cx2}, T_m and T_{liq} are measured with the two-tangent method from the onsets of the corresponding events. Using these values, the extension of the *SCLR* ($\Delta T_x = \Delta T_{x1} - T_g$) and the reduced glass transition temperature T_{rg} ($T_{rg} = T_g / T_{liq}$) are calculated to make a prediction of the GFA of the base alloy. From the thermal properties of the ribbon, it can be concluded that $Fe_{80}P_{13}C_7$ alloy has a low GFA [11, 35]. The results and the characteristic temperatures, including Curie temperature, T_c, are presented in Table 3.1.

Master Alloy	**Composition**	T_c **[K]**	T_g **[K]**	T_{x1} **[K]**	T_{x2} **[K]**	T_{liq} **[K]**	ΔT_x **[K]**	T_{rg}
MA-17	$Fe_{80}P_{13}C_7$	591	678	703	726	1286	25	0.527

Table 3.1: Curie temperature, T_c, glass transition, T_g, crystallization temperatures T_{x1} and T_{x2}, liquidus temperature, T_{liq}, extension of the supercooled liquid region, ΔT_x, and reduced glass transition temperature, T_{rg} of the MA-17 ($Fe_{80}P_{13}C_7$) metallic glass ribbon.

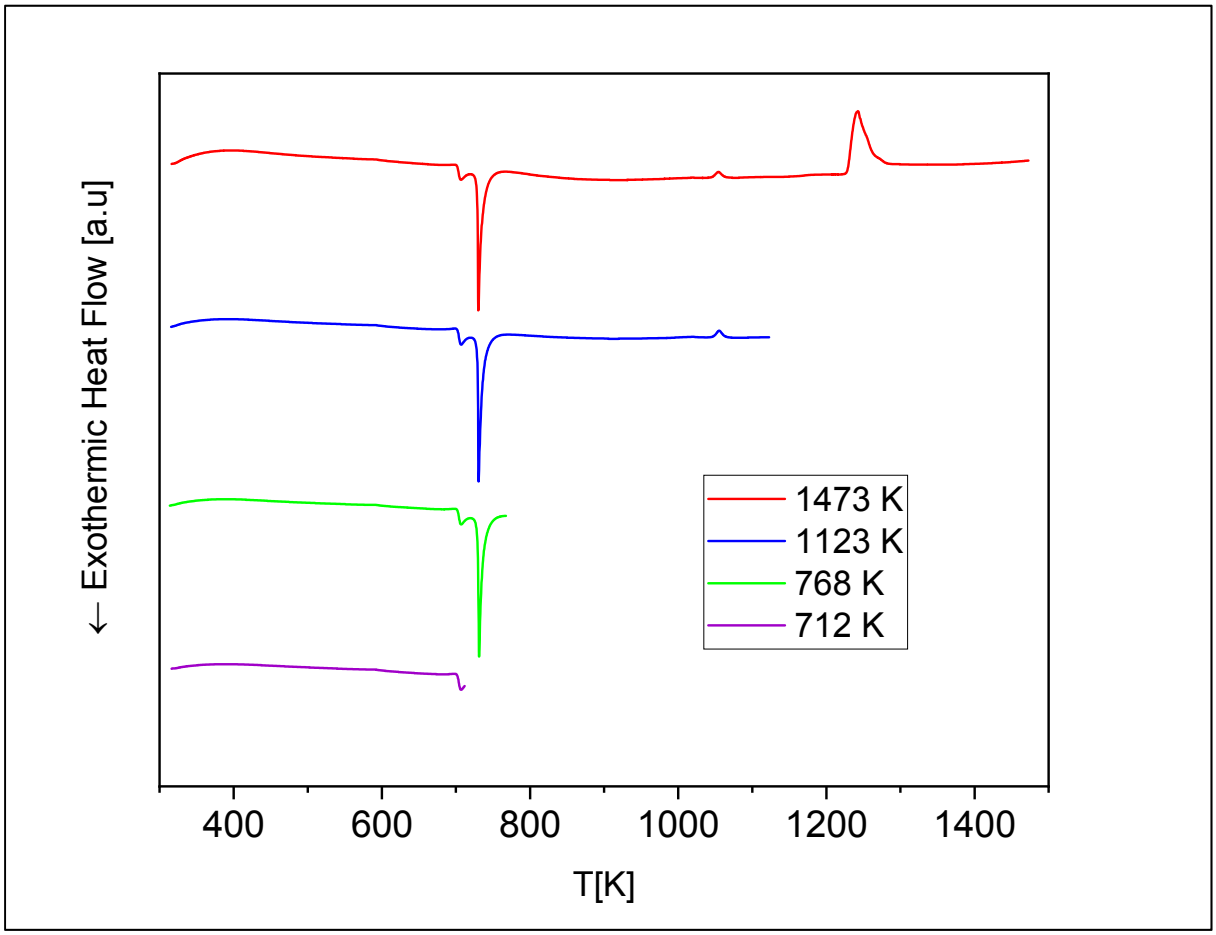

Figure 3.3: DSC traces of MA-17 ($Fe_{80}P_{13}C_7$) metallic glass ribbon, subjected to non-isothermal crystallization annealing at 20 K/min.

The structure evolution of the $Fe_{80}P_{13}C_7$ glassy ribbon upon non-isothermal crystallization annealing was investigated using DSC. The investigated samples were cut from the as cast ribbon, heated up to temperatures exceeding the peak temperature of each crystallization stage, but not exceeding the onset temperature of the following exothermic peak. The crystallization annealing processes were performed at 20 K/min, and the annealing temperature was determined considering the temperature overshooting of the DSC device, which was about 6 K at this rate of heating. It is important here to note that, after reaching the maximum temperature, the samples were not held at constant temperature, and the cooling was started immediately afterwards. In Figure 3.3, these heating curves and the initial high temperature DSC curve are depicted. After these processes, the annealed samples are investigated by X-ray diffraction using Co-K_α radiation (λ = 1.7089 Å).

In Figure 3.4, the XRD patterns of the annealed samples and the identified crystallization products are presented. The inset shows the very first XRD investigation of the as-cast ribbon prior to any other characterization experiments. From the inset, one can clearly see that, neither on the air side nor on the wheel side of the ribbon a sharp peak corresponding to a crystalline phase is present, and the characteristic broad diffraction maxima are clearly visible. This indicates that the sample was fully XRD-amorphous.

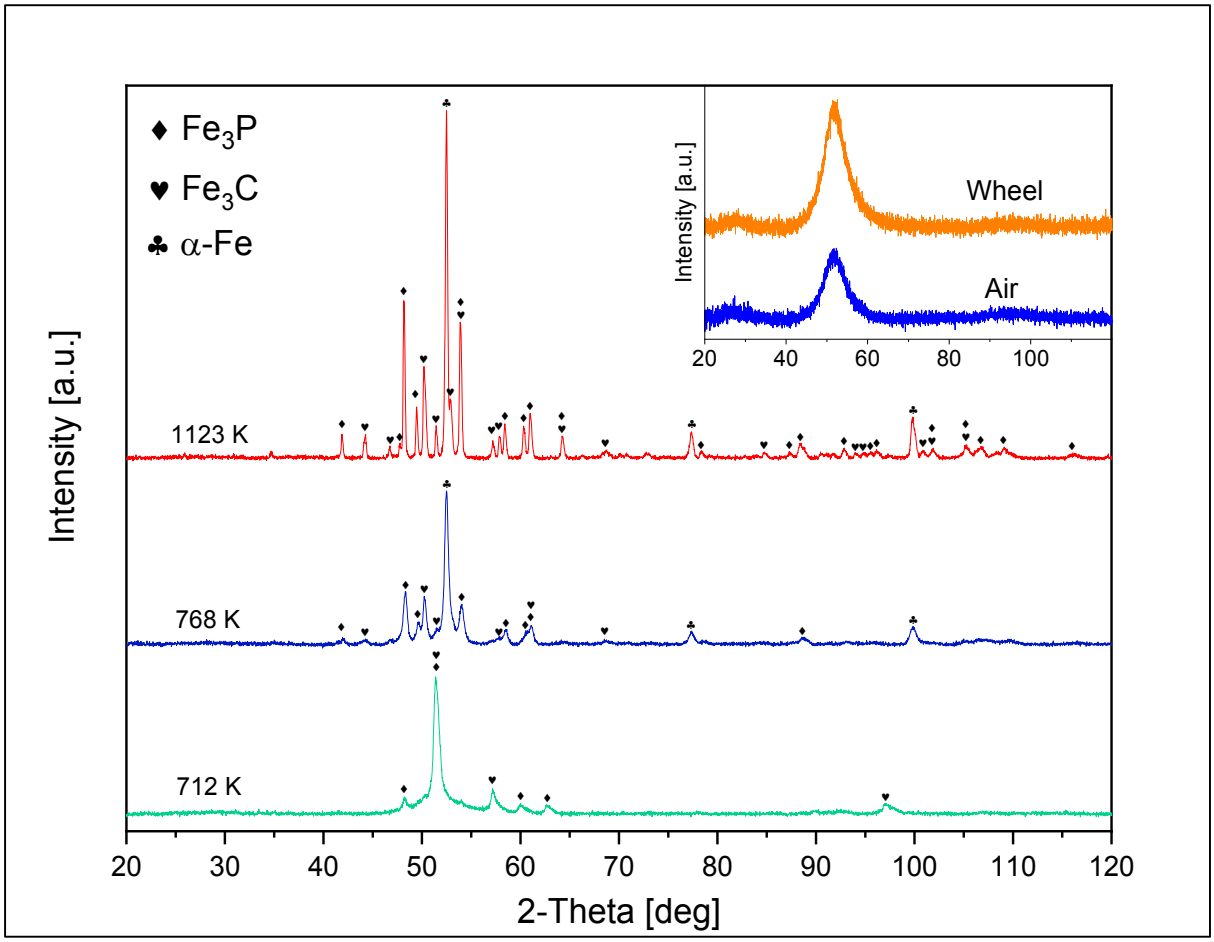

Figure 3.4: XRD patterns for MA-17 ($Fe_{80}P_{13}C_7$) glassy ribbon annealed up to different temperatures at 20 K/min and indexed crystallization peaks. The inset shows the XRD patterns of the as-cast ribbon.

According to the efficient cluster packing model [113], the structure of the metallic glasses can be described as a space filling network of densely packed solute-centered atomic clusters. For Fe-P-C ternary system, it is expected that these are consist of C-centered prism-like and P-centered antiprism-like clusters, which means that there are no P-P, C-C or P-C atomic bonds present in the glassy structure. In other words, these clusters share Fe atoms in common faces, edges or vertices, so that adjacent P or C-centered clusters overlap in the first coordination shell [114]. This is also in agreement with the mixing enthalpy principle proposed by Inoue [19], as the enthalpy of mixing of Fe-C and Fe-P pairs are −50 kJ/mol and −39.5 kJ/mol, respectively, while P-C pair exhibits 0 kJ/mol. Since the equilibrium crystalline phases of $Fe_{80}P_{13}C_7$ alloy are α-Fe solid solution, Fe_3P and Fe_3C [16, 28], it can be expected that these P- and C-centered short-range atomic clusters may become pre-existing nuclei and promote the primary crystallization of $Fe_3(P,C)$ phase, because they are similar in structure [108, 112]. On the other hand, there is a large difference between the structure of these SRO clusters and α-Fe phase. Therefore, the precipitation of $Fe_3(P,C)$ should be easier than α-Fe.

As seen from Figure 3.4, the sample which was heated up to 712 K (the purple bottom curve in Figure 3.3), still maintains its first broad peak besides the crystalline phases of Fe_3P and Fe_3C. The crystallization peak with highest intensity may correspond to the primary crystallization of $Fe_3(P,C)$ phase [7, 108, 110, 112]. However, some other primary crystallization products have also been reported [9, 16, 115] for this alloy. In our case, first $Fe_3(P,C)$ phase precipitates from the amorphous matrix, which corresponds to the first exothermic peak in the DSC trace. Therefore, most probable non-isothermal

crystallization structure of the sample heated up to 712 K should be $Fe_3(P,C)$, Fe_3C and Fe_3P embedded in a residual amorphous matrix, whose chemical composition is different from the starting composition.

The second sample was heated up to 768 K (the green DSC trace in Figure 3.3) precipitates to an equilibrium α-Fe(P,C) phase, as seen from Figure 3.4. Since the process is a non-isothermal crystallization event, there still exist the first broad peak, even though the annealing temperature exceeds the offset temperature of the second large exothermic peak in the DSC trace. This indicates that the kinetic of the crystallization is sluggish and the mobility of the atoms is difficult. Besides α-Fe, the primary crystallization products Fe_3C and Fe_3P become more prominent, as expected.

The third sample was heated up to 1123 K (the blue DSC trace in Figure 3.3). As a result, the amorphous alloy was completely crystallized, even though the sample cooled down immediately at 20 K/min as the previous samples mentioned above. The intensity difference between the peaks of the α-Fe and the $Fe_3(P,C)$ phases may be explained by the fact that α-Fe solid solution is actually the main crystallization product, whose lattice structure is much more simple than tetragonal Fe_3P and orthorhombic Fe_3C.

From Figure 3.2, one can see that the first Curie temperature of the crystalline state T_{cx1} is 1016 K. At this temperature, ferromagnetic bcc α-Fe(P) solid solution (unsaturated in P) reveals a magnetic transformation and becomes paramagnetic [16, 117-119].

The onset of second larger endothermic peak, T_{cx2} is at 1043 K, and this temperature corresponds to the well-known Curie temperature of α-Fe(C) solid solution and pure α-Fe [118]. Since the first endothermic peak is relatively small compared to the second one, it can be stated that magnetically transformed α-Fe upon heating is mainly unsaturated α-Fe(C) or α-Fe(P) unsaturated in P. This assumption can be made because of the absence of an endothermic peak corresponding to the allotropic transformation (α-Fe ↔ γ-Fe) temperature of α-Fe(C) saturated in C at 1000 K and also to the absence of an endothermic peak corresponding to the allotropic transformation of pure α-Fe at 1185 K in the DSC trace.

On the other hand, this second large endothermic peak may also correspond to an allotropic transformation of Fe(C) solid solution saturated in C at the equilibrium phase boundary between α and α + γ. Actually, both events result in endothermic peaks and they might be overlapping in the DSC curve of the sample.

Figure 3.5 shows the room temperature magnetic polarization of the as-cast MA-17 ($Fe_{80}P_{13}C_7$) glassy ribbon under an applied field of 800 kA/m. The magnetic polarization, J, was calculated from the total magnetic moment (emu) of the alloy sample and its calculated volume. The experiment reveals that the alloy exhibits a J_s of 1.3 Tesla. This indicates that because of the charge transfer from metalloid atoms to the *3d* band of iron, as well as the (*sp*)-*d* hybridization between the metalloids and iron, a significant decrease occurs in the magnetic moment of Fe [78].

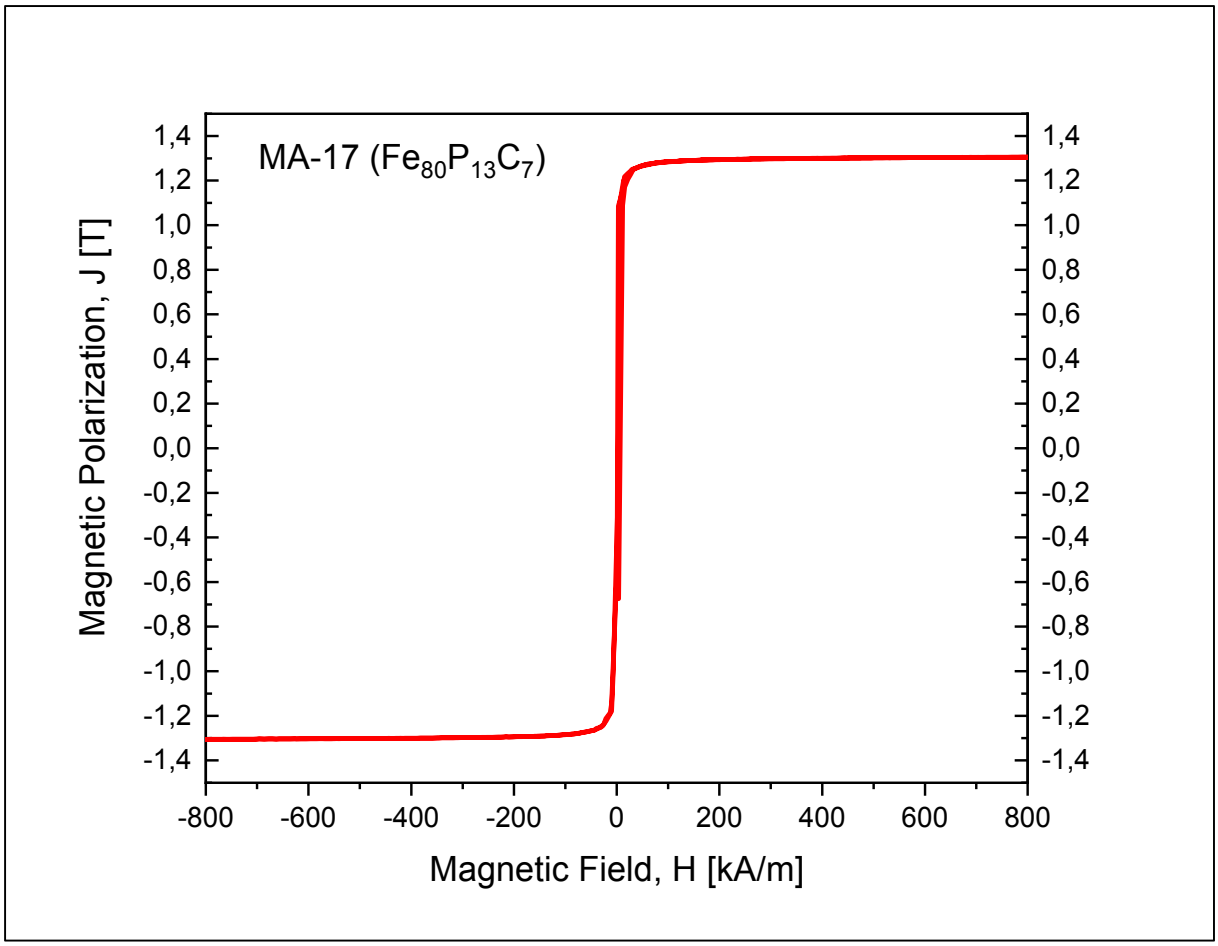

Figure 3.5: Hysteresis curve for as-cast MA-17 ($Fe_{80}P_{13}C_7$) glassy ribbon.

As mentioned before, the coercivity, H_c of the specimen cannot be resolved by the instrument even with 1 Oe (80 A/m) increments in the applied magnetic field. Therefore, it can be deduced that the H_c of the as-cast ribbon should be less than 80 A/m, indicating that the glassy alloy exhibits good soft magnetic properties (see Figure 1.10). This is not surprising considering the absence of grain boundaries and dislocations in the amorphous structure of the sample, which act as pinning centers for magnetic domain walls.

3.2 MA-17-Fluxed ($Fe_{80}P_{13}C_7$)

This amorphous ribbon was cast at 1323 K from the same master alloy, but it was subjected to a fluxing treatment as mentioned in Chapter 2.2. Further details of the casting process can be found in Table 2.2. Since it is the same master alloy as the previous unfluxed ribbon, and the casting temperatures are close to each other, one can expect that it should possess very similar properties to those mentioned in Chapter 3.1. However, some unexpected differences have been determined.

As mentioned before, fluxing treatment eliminates the influence of oxygen coming from the raw materials, which may form harmful oxides and/or metastable phases acting as heterogeneous nucleation sites [9]. Oxygen in Fe-based alloys mainly exists in oxide form because of its low solubility in iron. During melting process these oxides dissolve in the melt, and upon cooling they may form oxides and therefore deteriorate the GFA of the alloy [9]. Further, some oxides with high melting point do not dissolve during melting prior to casting process. If these impurities have a large size, they float to the surface of the melt and form slag, which can be removed from the master alloy after its preparation. However, if these inclusions have a small size, they get trapped in the master alloy and act as nucleation agents in the casting process, since there is not enough amount of oxygen dissolved in the melt under high purity argon atmosphere to promote the growth of these oxides [6, 9, 116]. In order to prevent this, master alloy has to be fluxed with B_2O_3. Fluxing agent B_2O_3 is capable of reacting with these oxides and trap them along with surface impurities. After gravity segregation, the impurities either get dissolved or deactivated (by being wet) by the molten oxide [1, 6, 90, 116]. On the other hand, if the small sized inclusions have a low melting point, they may not deteriorate the GFA at all and even be beneficial in terms of microalloying [116].

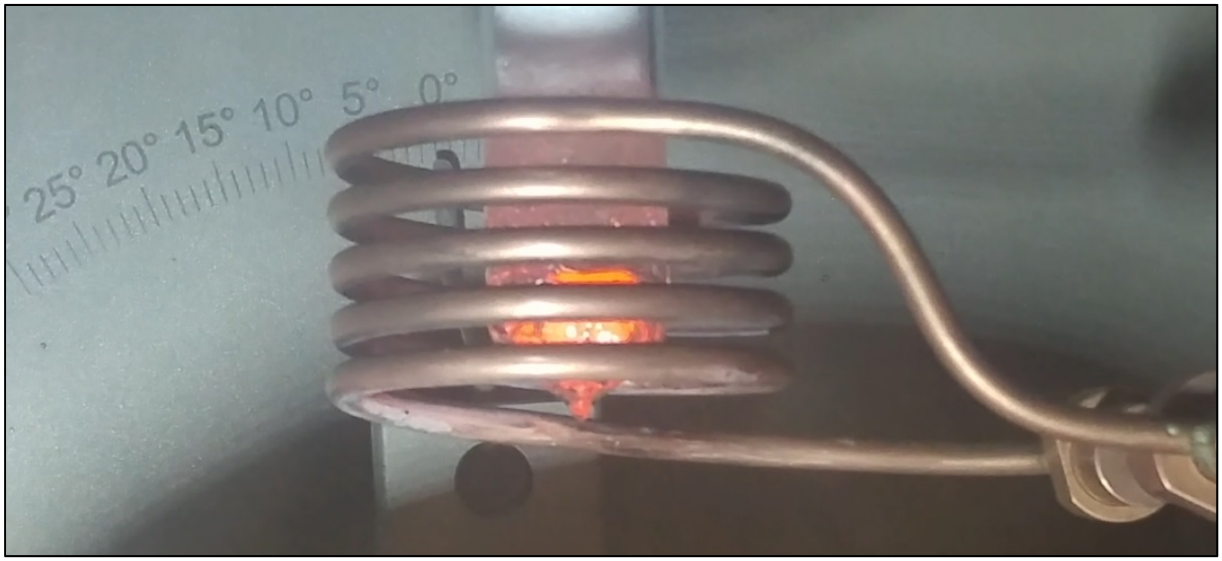

Figure 3.6: The second setup used for the fluxing treatments in this work, this time with Al_2O_3 crucibles.

Recently, Yang et al. [6] has reported that a very commonly implemented fluxing agent composed of B_2O_3 and CaO with a mass ratio of 3:1 result in a significant incorporation of boron in the alloy by a chemical reaction at temperatures above 1500 K in the expense of P and mostly C. After the APT (Atom probe tomography) analysis they have observed that the metalloid amount (13 % P and 7 % C) of nominal atomic composition was decreased to 12 % P and to 3 % C, with about 1.5 % B incorporation. Later, Wan et al. [8] has confirmed this statement and they have introduced an improved fluxing treatment, which consists of utilizing only B_2O_3 as fluxing agent and limiting the temperature to 1450 K. They showed that with this improved method, the amount of boron alloyed was reduced to

0.4 at.%. Therefore, in this present work only B_2O_3 was used for fluxing treatment. However, as mentioned in Chapter 2.2, it was not possible to regulate the temperature precisely by only using the AC generator, and thus it can be expected that the temperature was above 1450 K during fluxing treatments.

In Figure 3.6, the setup used for fluxing treatment is depicted. As seen from the figure, the molten master alloy was completely immersed in molten fluxing agent and it continuously generated gas bubbles during the process. These bubbles on the interface between the molten alloy and the fluxing agent was accounted for the chemical reaction products of CO and CO_2 [6], and this also in our case most likely led to a reduction of C amount of the nominal composition.

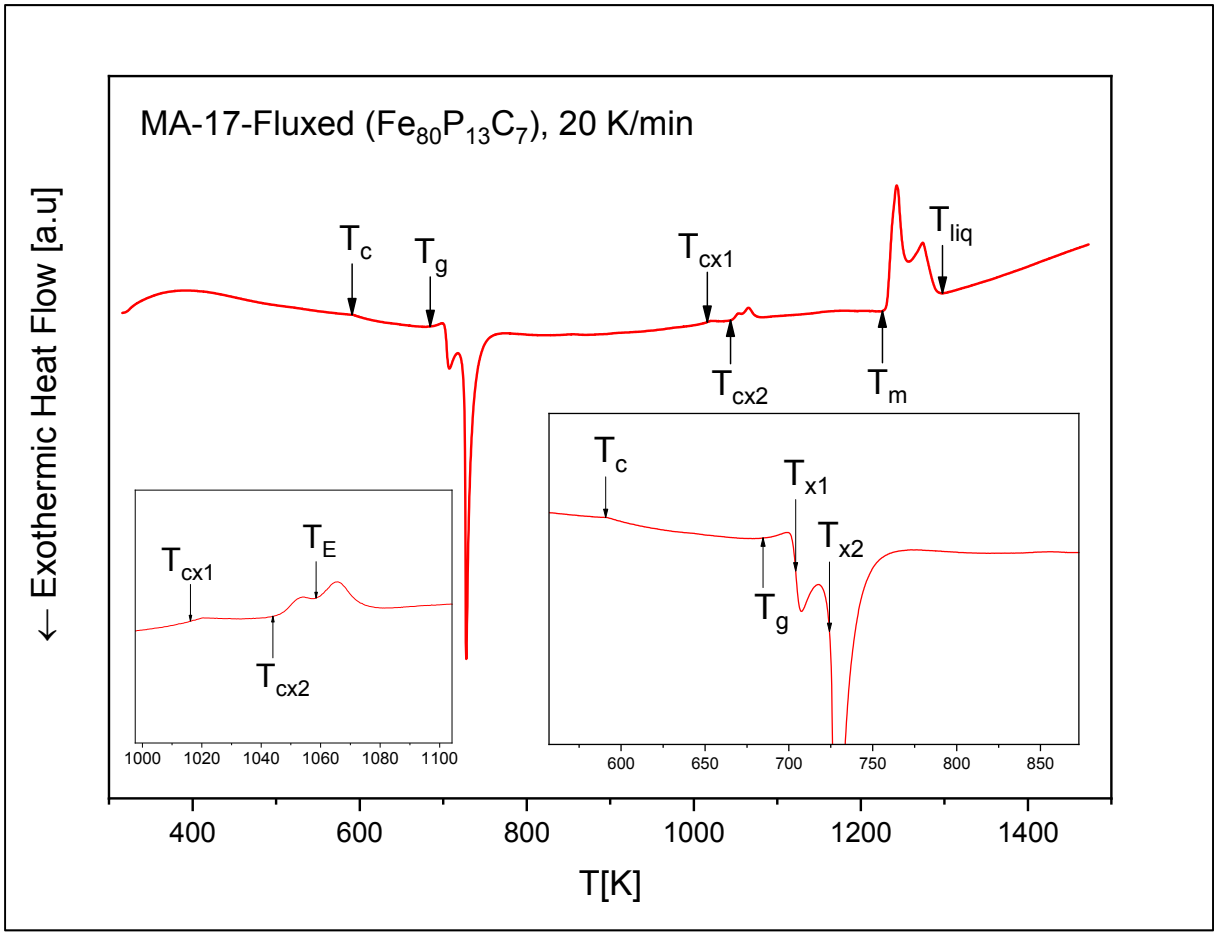

Figure 3.7: DSC trace of as-cast MA-17-Fluxed ($Fe_{80}P_{13}C_7$) glassy ribbon. The insets show the enlarged regions of the same curve.

Master Alloy	Composition	T_c [K]	T_g [K]	T_{x1} [K]	T_{x2} [K]	T_{liq} [K]	ΔT_x [K]	T_{rg}
MA-17-Fluxed	$Fe_{80}P_{13}C_7$	590	679	703	724	1297	24	0.523

Table 3.2: Curie temperature, T_c, glass transition, T_g, crystallization temperatures T_{x1} and T_{x2}, liquidus temperature, T_{liq}, extension of the supercooled liquid region, ΔT_x, and reduced glass transition temperature, T_{rg} of the MA-17-Fluxed ($Fe_{80}P_{13}C_7$) metallic glass ribbon.

Taking into account the difficulties in the process, and the relatively shorter (about 1.5 hour) fluxing time, the author was not sure about the overall effect of the treatment on the master alloy. After fluxing process, solidified master alloy piece was removed from the alumina crucible and mechanically polished before the casting process. Fortunately, the casting attempt was successful, and the resulting ribbon was used for further investigations.

In Figure 3.7, the high temperature DSC trace of the as cast ribbon is shown. The heating curve of the fluxed ribbon exhibits no major difference from the unfluxed one in Figure 3.2, and shows clearly the glass transition event, T_g, the supercooled liquid region, *SCLR* ($\Delta T_x = \Delta T_{x1} - T_g$), Curie temperature in amorphous state, T_c, as well as in crystalline states, T_{cx1} and T_{cx2}, and the two-staged crystallization event, T_{x1} and T_{x2}. Apart from the unfluxed one, this fluxed ribbon presents an additional endothermic peak, T_E at 1058 K after T_{cx1} and T_{cx2} and another endothermic melting peak before T_{liq}.

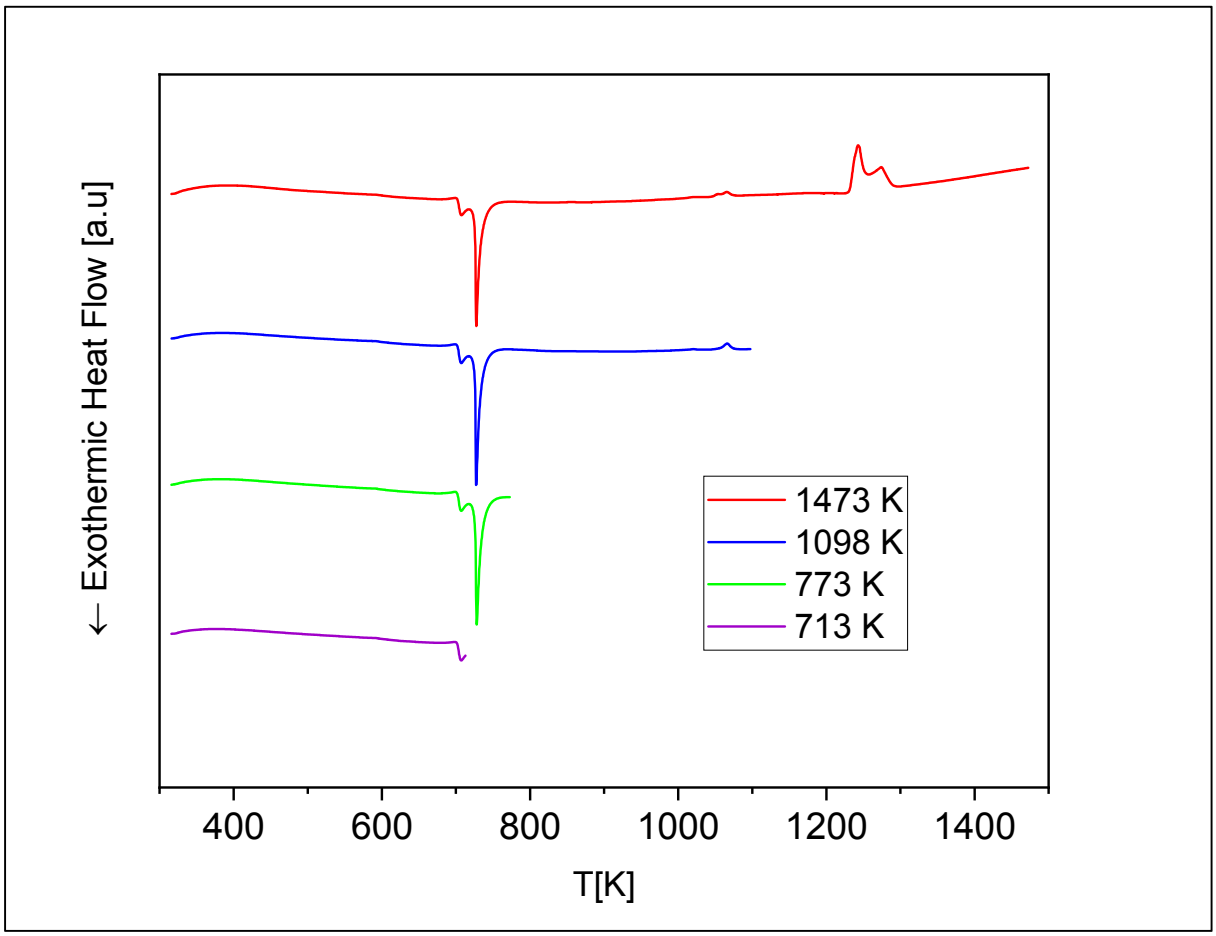

Figure 3.8: DSC traces of MA-17-Fluxed ($Fe_{80}P_{13}C_7$) metallic glass ribbon, subjected to non-isothermal crystallization annealing at 20 K/min.

From the DSC trace, it can be seen that also for this alloy the eutectic crystallization is not the case and the equilibrium phases are formed in two stages. T_g, T_{x1}, T_{x2}, T_{cx1}, T_{cx2}, T_E, T_m and T_{liq} are measured with the two-tangent method from the onsets of the corresponding events. Using these values, the extension of the *SCLR* ($\Delta T_x = \Delta T_{x1} - T_g$) and the reduced glass transition temperature T_{rg} ($T_{rg} = T_g / T_{liq}$) are determined to make a prediction of the GFA. Thermal properties and calculated T_{rg}, ΔT_x values of the fluxed ribbon are presented in Table 3.2. Considering these values, it can be concluded that the fluxed ribbon exhibits a slightly lower GFA than the unfluxed one. Both T_{rg} and ΔT_x values are

smaller than those of the unfluxed ribbon. However, the difference in both GFA parameters are very small and can be neglected. In addition to the lower ΔT_x and T_{rg} values, fluxed ribbon exhibits a wider melting region (T_{liq}-T_m) of 72 K compared to the unfluxed ribbon of 62 K, and there are two separated melting peaks present in this wider region. This indicates that fluxed ribbon is synthesized from a more off-eutectic composition than the unfluxed one. The small differences in thermal properties should be most probably related to the fluxing process, possibly to the change of the nominal composition after fluxing treatment, since the casting temperatures of the ribbons are very close and the remaining casting parameters are identical.

In Figure 3.8, DSC traces of the non-isothermal crystallization annealing and initial high temperature DSC curve of the fluxed ribbon are depicted. The investigated samples were cut from the as-cast ribbon, heated up to temperatures exceeding the peak temperature of each crystallization stage, but not exceeding the onset temperature of the following exothermic peak. As in the case of the unfluxed one, these measurements are performed considering the temperature overshooting of the device. After these steps, each sample is subjected to XRD analysis in order to identify crystallization steps and their sequence.

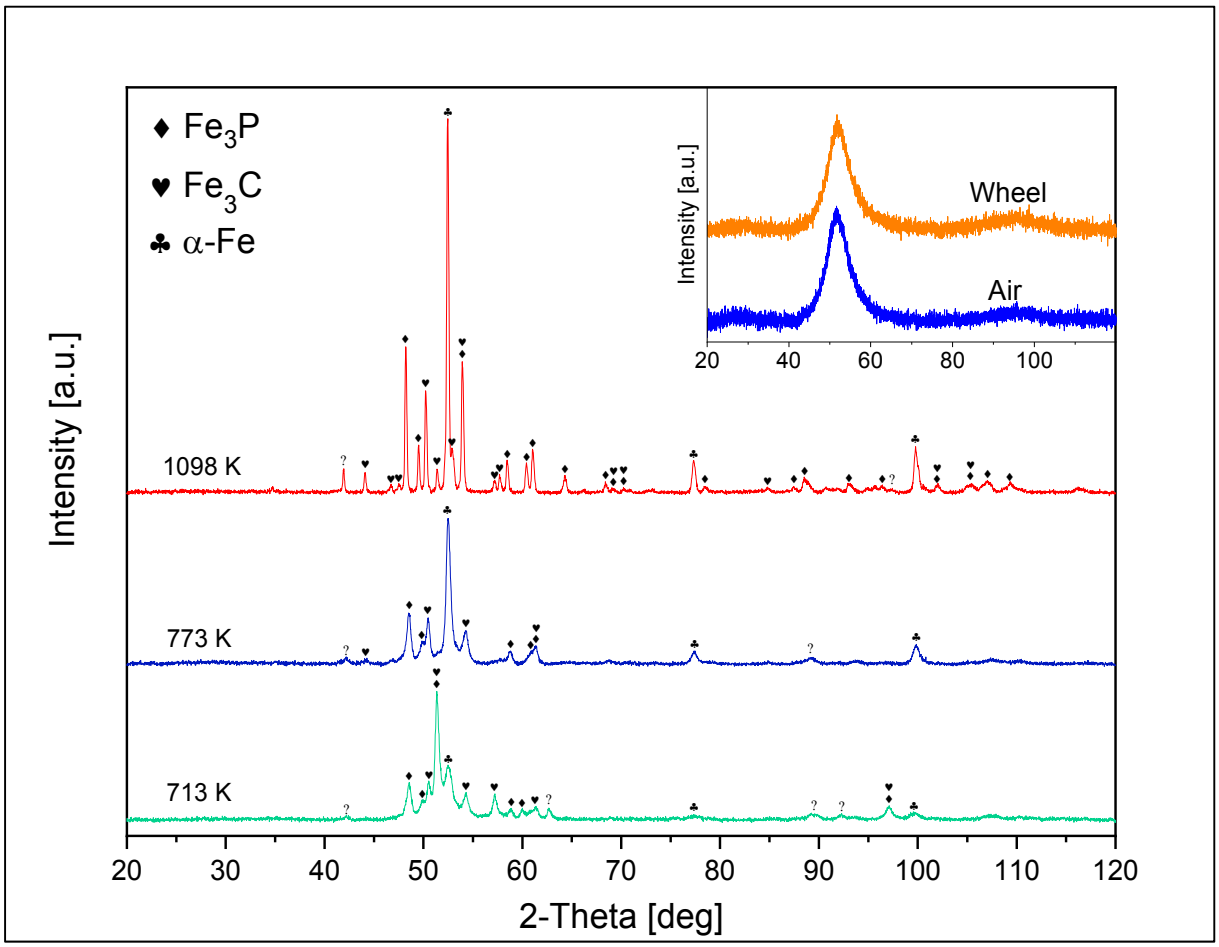

Figure 3.9: XRD patterns for MA-17-Fluxed ($Fe_{80}P_{13}C_7$) glassy ribbon annealed up to different temperatures at 20 K/min and matched crystallization products. The inset shows the XRD pattern of the as-cast ribbon.

In Figure 3.9, the XRD patterns of the annealed samples and the identified crystallization products are presented. The inset shows the very first XRD investigation of the as-cast ribbon, prior to any other characterization experiments. From the inset, one can clearly see that, neither on the air side nor on the

wheel side of the ribbon, a sharp peak corresponding to a crystalline phase is present, and the characteristic broad diffraction maxima are clearly visible.

As seen from Figure 3.9, the sample heated up to 713 K (purple DSC curve in Figure 3.8), still maintains its first broad peak besides the crystalline phases of Fe_3P and Fe_3C. Surprisingly, the fluxed ribbon exhibits also α-Fe at this temperature, which was the product of the second crystallization event of the unfluxed ribbon. The crystallization peak with highest intensity may correspond to the primary crystallization of $Fe_3(P,C)$ phase. The intensity of the peaks correspond to α-Fe are relatively weak, which may indicate that this phase starts to precipitate only after $Fe_3(P,C)$ phase forms as the primary crystallization product.

Since the crystallization temperatures of the fluxed and unfluxed ribbons are very close, the reason of the early precipitation of the α-Fe might be related to the fluxing treatment, which might have caused a decrease in overall metalloid amount of the nominal composition [6, 8], especially in the carbon content. Since C has a very low solubility in Fe compared to P, during the precipitation of α-Fe more C atoms must be diffused and rearranged in comparison to P atoms. As a result, a reduction in carbon content might have had promoted the early precipitation of α-Fe [29]. On the other hand, also phosphorus might have been evaporated during the fluxing treatment.

The second sample which was heated up to 773 K (green DSC trace in Figure 3.8) shows the primary crystallization products of Fe_3P and Fe_3C. Additionally, α-Fe becomes the dominating crystalline phase at this temperature, as can be seen from its peak intensities. Because of the non-isothermal crystallization annealing, even at 773 K the first broad diffraction maxima still can be seen in the diffraction pattern, which means that the amorphous matrix still exists, and the precipitated equilibrium phases are embedded in the glassy matrix [2, 3]. The third sample heated up to 1098 K (blue DSC trace in Figure 3.8) shows the equilibrium crystalline phases Fe_3P, Fe_3C and α-Fe. It can be seen that the sample was completely crystallized.

In Figure 3.10, the room temperature magnetic polarization of the as-cast MA-17-Fluxed ($Fe_{80}P_{13}C_7$) glassy ribbon under an applied field of 800 kA/m is shown. The experiment reveals that the fluxed ribbon exhibits a J_s of 1.31 T. This is value is very close to the unfluxed ribbon and the small difference can be attributed to the possible metalloid deviation in the alloy composition. The Curie temperatures of the fluxed and unfluxed ribbons in the glassy state are also very close to each other. This shows that ferromagnetism in amorphous state is not so sensitive to small changes in the metalloid concentration [56, 61, 62].

In Figure 3.7, one can see that the fluxed ribbon exhibits its first Curie temperature of the crystalline state T_{cx1} at 1016 K (onset of the first endothermic peak) and at this temperature, ferromagnetic bcc α-Fe(P) solid solution (unsaturated in P) becomes paramagnetic. This can be expected since α-Fe(P) solid solution saturates in P at 1.65 at.% and the Curie temperature decreases linearly from 1185 K to 1008 K at the equilibrium phase boundary between α and α + Fe_3P [119].

The onset temperature of the second larger endothermic peak, T_{cx2} is again at 1043 K and this temperature corresponds to the Curie temperatures of α-Fe(C) solid solution and pure α-Fe. Since the first endothermic peak is relatively small compared to the second one, it can be stated that magnetically transformed α-Fe upon heating is mainly α-Fe(C) solid solution and/or pure α-Fe, but most likely a α-Fe(C) phase which is not saturated in C. This assumption can be made due to the absence of an endothermic peak, which corresponds to the allotropic transformation (α-Fe ↔ γ-Fe) temperature of saturated α-Fe(C) 1000 K, as well as to the absence of an endothermic peak corresponding to the allotropic transformation of pure α-Fe at 1185 K in the DSC trace. Other than these two endothermic

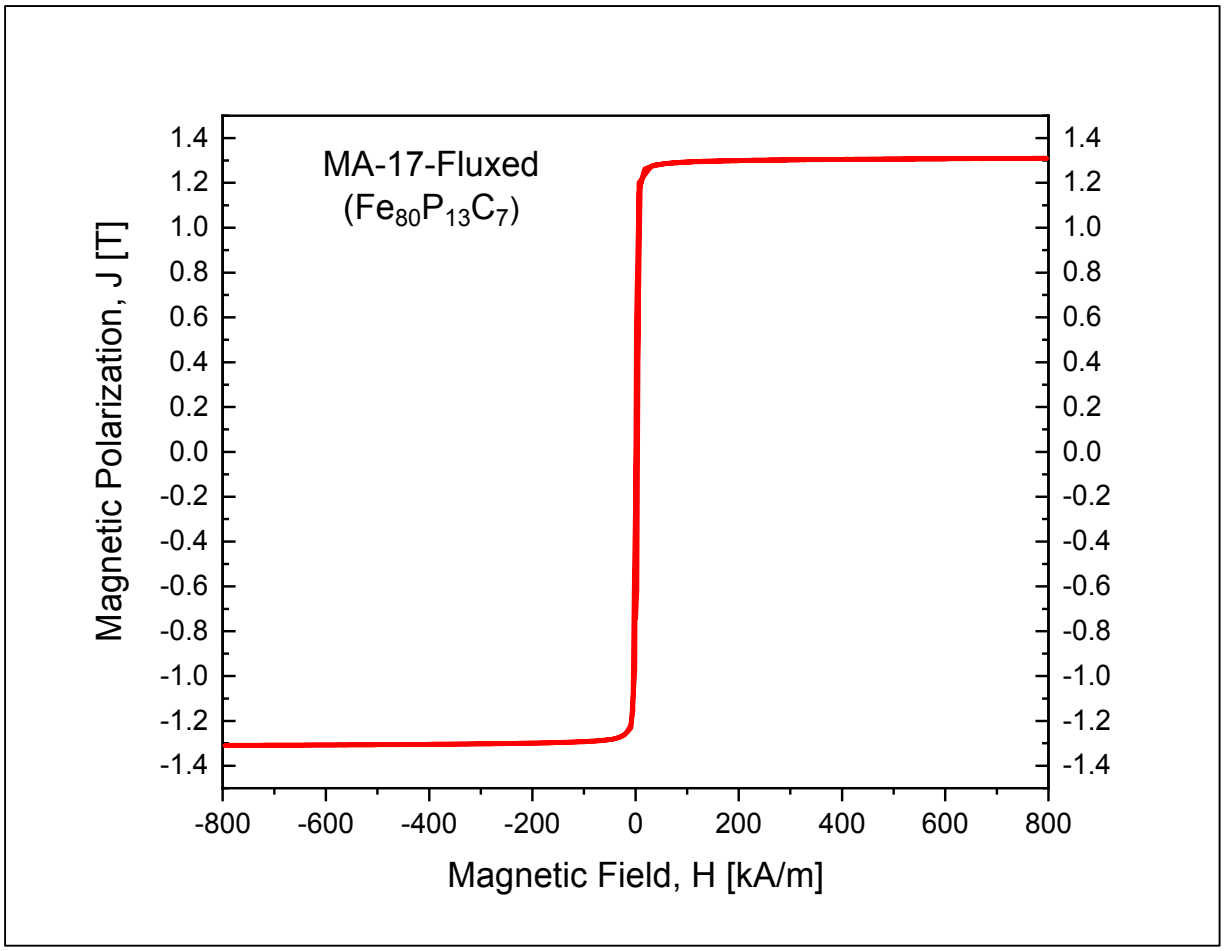

Figure 3.10: Hysteresis curve for as-cast MA-17 ($Fe_{80}P_{13}C_7$) glassy ribbon.

peaks of magnetic transformation, there is an additional peak, T_E, in the DSC curve of the as cast sample. The onset of this largest endothermic peak is at 1058 K and it may correspond to the allotropic transformation of saturated α-Fe(C) in γ-Fe at the equilibrium phase boundary between α and γ + α. Another possible explanation of this peak may be the magnetic transformation of the unsaturated α-Fe(P) solid solution, whose Curie temperature lies between 1185 K and 1018K. Since it saturates in P at 1.65 at.%, one might expect that, upon heating there should not be enough free P atoms in alloy to saturate all of the α-Fe crystals, because most of the P atoms should have been precipitated already in Fe_3P phase, which is stable at this temperature.

In other words, the fraction of the almost saturated α-Fe(P) should be relatively less than unsaturated α-Fe(P) in the crystallized sample. This can also be seen from the difference in intensities of the endothermic peaks. The first peak whose onset corresponds to 1018 K is the smallest one. This should be related to T_c of the almost saturated α-Fe(P) phase. The onset of the second endothermic peak is at 1043 K and this should be T_c of the unsaturated α-Fe(C). The third peak is then either γ-transition of the unsaturated α-Fe(C) or T_c of the unsaturated α-Fe(P) solid solution.

3.3 MA-18 ($Fe_{60}Ni_{20}P_{13}C_7$)

This ribbon belongs to the composition of $Fe_{60}Ni_{20}P_{13}C_7$ was cast at 1473 K, and the details of its master alloy (MA-18) and other casting parameters can be found in Table 2.2. It is important here to note that, the author has already tried to synthesize amorphous ribbons from this composition (MA-11). However, all the casting attempts using MA-11 has failed, except the last small piece of it, which was subjected to fluxing treatment. That ribbon was cast at 1273 K and the angular frequency of the copper wheel was only 30 Hz. With this new master alloy (MA-18) we have tried to repeat the casting parameters of previously mentioned ribbons (MA-17 and MA-17-Fluxed) but in the vicinity of 1273 K the results were not successful. It was clear that this new master alloy needed either a faster rate of cooling (accelerated wheel speed) or a higher casting temperature.

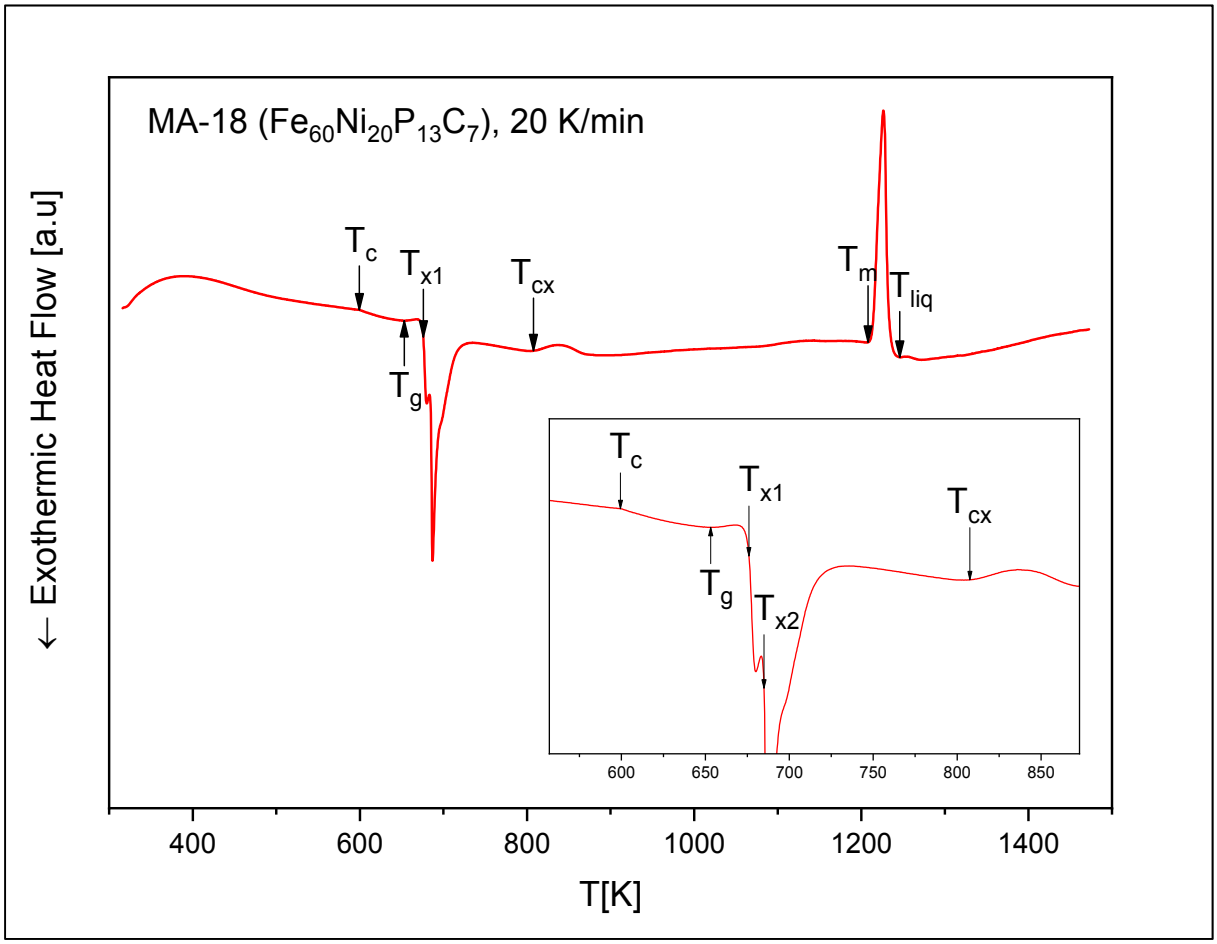

Figure 3.11: DSC trace of as-cast MA-18 ($Fe_{60}Ni_{20}P_{13}C_7$) glassy ribbon. The inset shows the enlarged region of the same curve.

Master Alloy	Composition	T_c [K]	T_g [K]	T_{x1} [K]	T_{x2} [K]	T_{liq} [K]	ΔT_x [K]	T_{rg}
MA-18	$Fe_{60}Ni_{20}P_{13}C_7$	599	653	676	685	1245	23	0.524

Table 3.3: Curie temperature, T_c, glass transition, T_g, crystallization temperatures T_{x1} and T_{x2}, liquidus temperature, T_{liq}, extension of the supercooled liquid region, ΔT_x, and reduced glass transition temperature, T_{rg} of the MA-18 ($Fe_{60}Ni_{20}P_{13}C_7$) metallic glass ribbon.

The partial substitution of Ni for Fe has been studied by many researchers [5, 6, 8, 10, 12-14, 17, 18, 63]. The main goal of this substitution was to improve the compressive plasticity of the Fe-based ($Fe_{80}P_{13}C_7$) BMGs and to investigate the effects of this substitution on thermal stability, mechanical properties and magnetic properties. Since the enthalpy of mixing of Ni-C (−39 kJ/mol) and Ni-P (−34.5 kJ/mol) are much smaller than Fe-C (−50 kJ/mol) and Fe-P (−39.5 kJ/mol), one can expect that the same SRO of the C-centered prism-like and P-centered antiprism-like clusters are embedded in $Fe_{80-x}Ni_xP_{13}C_7$ system.

As these solute-centered atomic clusters share Fe atoms in common faces, edges or vertices, so that adjacent P or C-centered clusters overlap in the first coordination shell, increasing Ni content fills the empty regions between the clusters and they begin to not to overlap anymore [5, 8, 13]. As a result, Ni substitution increases the metal-metal bonds which are linking the clusters, and this results in an enhancement on the ductility of the BMGs because of the good mobility of the metal-metal bonds with non-directional *s* character.

In Figure 3.11, the high temperature DSC trace of the $Fe_{60}Ni_{20}P_{13}C_7$ ribbon is depicted. As seen from the DSC curve, this composition also exhibits Curie temperatures in both states, a glass transition temperature, T_g, followed by an almost singe-staged crystallization event, which further confirms the glassy state of the ribbon. Thus, its melting behavior indicates that [1, 3] this composition is either eutectic or very close to it. Thermal properties of the sample, ΔT_x and T_{rg} values are presented in Table 3.3.

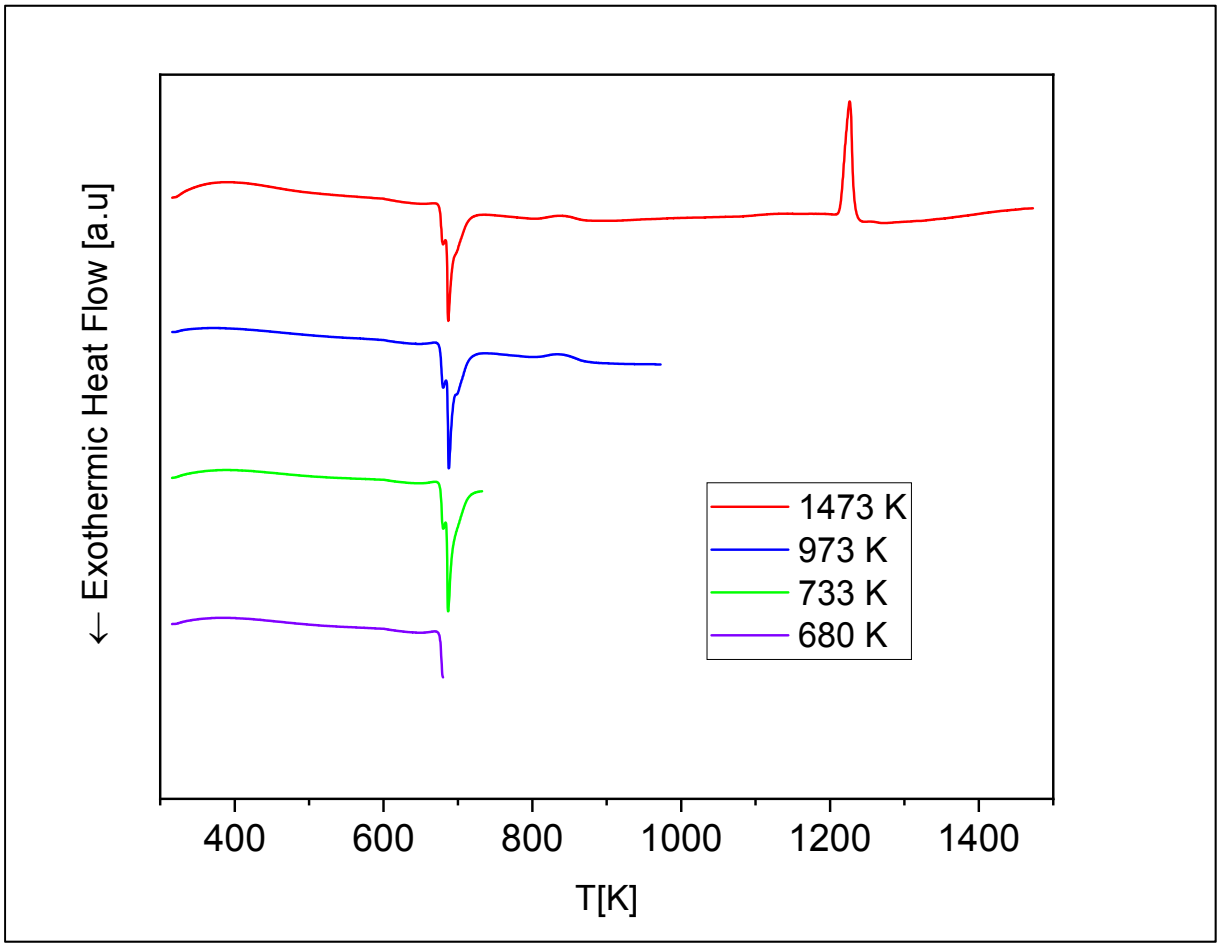

Figure 3.12: DSC traces of MA-18 ($Fe_{60}Ni_{20}P_{13}C_7$) metallic glass ribbon, subjected to non-isothermal crystallization annealing at 20 K/min.

Gradual decrease in the glass transition temperature and the onset temperature of crystallization upon Ni addition has been reported before [5, 6, 12, 13, 63]. It is well known that T_g and T_x is related to the average bonding strength between the atoms of the constituent elements [2, 12, 75]. As mentioned before, smaller negative mixing enthalpy of Ni with the other atoms in the alloy may cause a decrease of T_g and T_x as a result of weakened average atomic bonding strength. Considering the small differences in ΔT_x and T_{rg} values of the present ribbon and those of the unfluxed $Fe_{80}P_{13}C_7$ ribbon, it can be stated that this amount of Ni substitution slightly deteriorates the GFA of the alloy. This can be explained in two different aspects: (1) Ni atoms depress T_g more than they depress T_{liq}, and this leads to a decrease in GFA. (2) Ni atoms reduce T_x more than they reduce T_g, and this results in a narrower SCLR. This is not surprising when the properties of Ni are taken into account. First, there is only a minor difference between the metallic radii of Ni and Fe, 124 pm and 126 pm, respectively [5]. This amount of atomic mismatch is very small compared to the necessity of 12% atomic size ratio for a good GFA proposed by Inoue [1]. When the elements having the negative enthalpy of mixing with the main constituents are added, their effects on glass formation are strongly dependent on their atomic sizes. Apparently, Ni atoms do not contribute to a densely packed atomic structure.

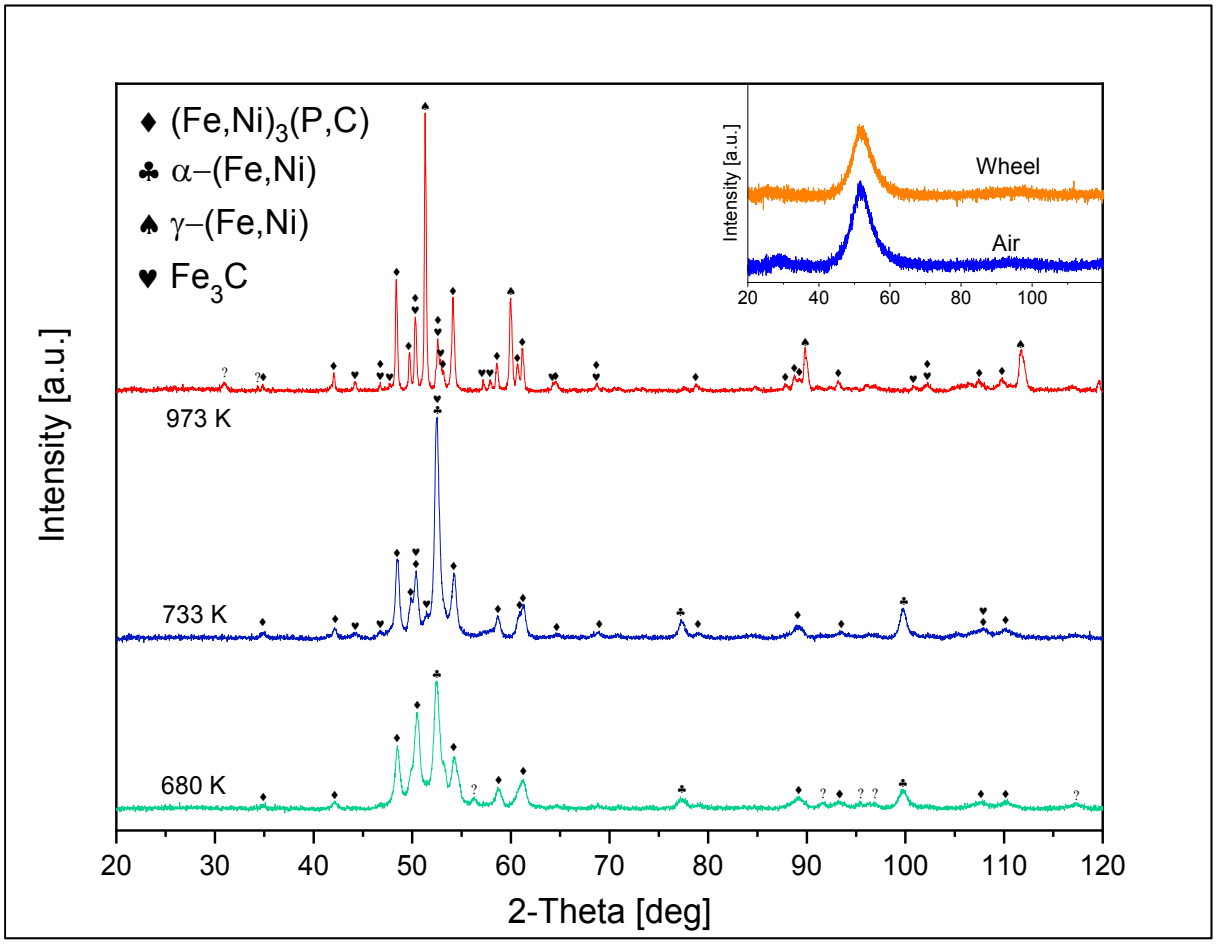

Figure 3.13: XRD patterns for MA-18 ($Fe_{60}Ni_{20}P_{13}C_7$) glassy ribbon annealed up to different temperatures at 20 K/min and matched crystallization products. The inset shows the XRD pattern of the as-cast ribbon.

However, considering the ΔT_x and T_{rg} values of the $Fe_{60}Ni_{20}P_{13}C_7$ BMG from the same work, the GFA should have been decreased in comparison to $Fe_{80}P_{13}C_7$ BMG with 2 mm D_{max}. Thus, it can be stated

that thermal properties are not always a good indicator to predict the GFA alone, which has been reported in many cases [1-3, 29]. In our case, ΔT_x and T_{rg} values are slightly smaller than those of MA-17 ($Fe_{80}P_{13}C_7$) ribbon, but in order to be able to correctly determine the GFA, new samples from the same master alloys of MA-17 and MA-18 must be cast in bulk form in the future, and the critical diameters of the rods must be compared.

In figure 3.12, DSC traces of the non-isothermal crystallization annealing and the initial high temperature DSC curve of the MA-18 ($Fe_{60}Ni_{20}P_{13}C_7$) metallic glass ribbon are shown. As the case in previous ribbons, these samples were subjected to XRD analysis and their diffraction patterns, along with the as-cast ribbons XRD patterns, are depicted in Figure 3.13.

The first sample heated up to 680 K (small left side shoulder of the large exothermic peak, purple curve in Figure 3.12) seems to crystallize in two different phases: $(Fe,Ni)_3(P,C)$ and α-(Fe,Ni) solid solution. Additionally, there are some unidentified diffraction peaks in the pattern. Since the first exothermic peak of the DSC trace is very small, most likely the crystallization products of the main large peak should have also been formed, considering the ~6 K temperature overshoot of the DSC device. The broad diffraction maximum of the amorphous matrix can also be seen. The second sample heated up to 733 K (green DSC trace in Figure 3.12) still presents this amorphous matrix along with the crystallization products of $(Fe,Ni)_3P$, α-(Fe,Ni) solid solution and Fe_3C.

The third sample heated up to 973 K (blue DSC curve in Figure 3.12) exhibits γ-(Fe,Ni), $(Fe,Ni)_3P$ and Fe_3C crystallization products. It can be seen that the sample is completely crystallized, and α-(Fe,Ni) solid solution peaks are disappeared. The total austenitic nature of the crystallized sample indicates that, upon heating, a martensitic (or diffusionless) α-(Fe,Ni) ↔ γ-(Fe,Ni) transformation took place, where the broad endothermic peak in the DSC curve [125] most probably corresponds to this event. This also explains the absence of an endothermic peak at higher temperatures, related to a magnetic or allotropic transition of α-Fe(P,C) solid solution without any Ni. On the other hand, the metalloids in the alloy most probably stabilized the fcc γ-(Fe,Ni) phase. That is, they reduced the M_s and M_f (martensite start and finish temperatures, respectively) below the room temperature [125]. As a result, the sample exhibits only fcc γ-(Fe,Ni) solid solution.

Considering the Fe-Ni binary phase diagram, it can be stated that at 20 at.% Ni, saturated α-(Fe,Ni) solid solution transforms in γ-(Fe,Ni) around 873 K [120]. However, if we assume that there were no metalloids in the composition, this should correspond to an alloy composition of 25 at.% Ni and 75 at.% Fe in the binary phase diagram [120], which in turn leads to a lower transition temperature for equilibrium phase boundary. Meanwhile, since Ni atoms were already crystallized in $(Fe,Ni)_3P$ phase, the overall Ni amount in a supersaturated α-(Fe,Ni) solid solution must be less than 25 at.%. At this composition range, martensitic transformation of bcc α-(Fe,Ni) solid solution in fcc γ-(Fe,Ni) takes place between those temperatures (A_s and A_f, austenite start and finish, respectively), which are significantly higher than the onset and offset temperatures of the broad endothermic peak in the DSC trace. However, the addition of metalloids should have lowered these temperatures, as they did to M_s and M_f upon cooling of the sample. Moreover, Curie temperature of α-(Fe,Ni) solid solution at 23 at.% Ni was measured to be around at 840 K [120]. This might also explain the broad endothermic peak, since two endothermic events are close to each other and their peaks might be overlapping.

Room temperature magnetic polarization of the as-cast MA-18 ($Fe_{60}Ni_{20}P_{13}C_7$) glassy ribbon under an applied field of 800 kA/m is depicted in Figure 3.14. The experiment reveals that the fluxed ribbon exhibits a J_s of 0.95 T. The gradual decrease in magnetic polarization upon Ni substitution for $Fe_{80-x}Ni_xP_{13}C_7$ system has been reported before [12, 13, 29, 63]. This can be attributed to the dilution effect of Ni atoms on the mean magnetic moment of the amorphous alloy. The magnetic moments of Fe and Ni are 2.2 μ_B and 0.6 μ_B, respectively.

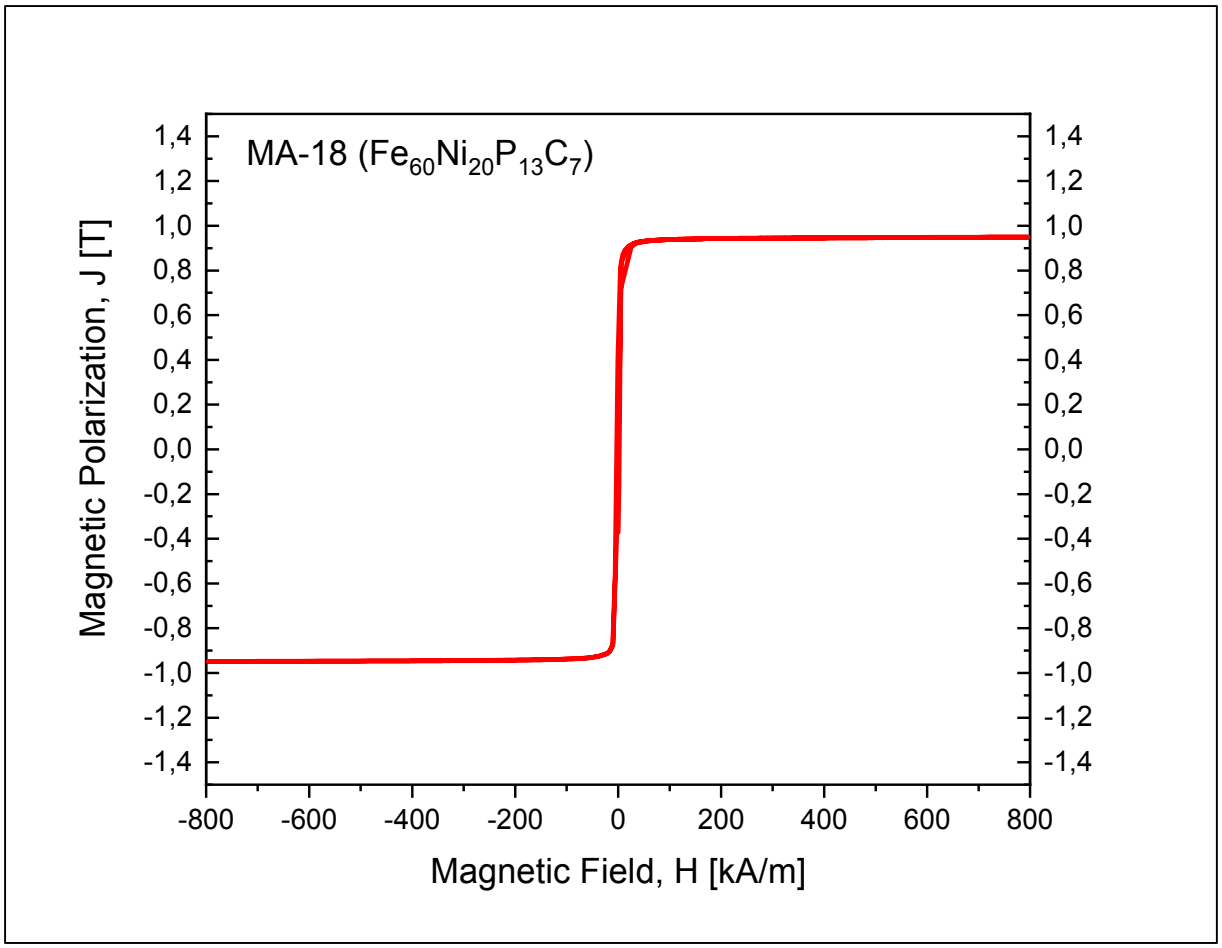

Figure 3.14: Hysteresis curve for as-cast MA-18 ($Fe_{60}Ni_{20}P_{13}C_7$) glassy ribbon.

Nickel resides on the right-hand side of the Slater-Pauling curve (see Figure 1.6), and thus, its local magnetic moment does not depend on the composition. In other words, its local magnetic moment remains same irrespective of its nearest neighbor atom is whether Fe or Ni. According to Luborsky [56], the number of electrons donated to the *d*-bands of transition metals can be listed as: $P_{13}C_7 > S_{15}B_{10} > P_{16}B_6Al_3 > P_{14}B_6 > Si_9B_{13} > B_{20}$. Resulting from the charge transfer phenomena, Ni behaves paramagnetic in our composition [62, 72], which in turns leads to a linear drop in average magnetic moment of the alloy.

Curie temperature of the glassy state is 9 K higher than that of the MA-17 ($Fe_{80}P_{13}C_7$) ribbon. This has been also reported before [12, 13, 63], and explained by means of exchange interactions between the magnetic atoms. Since iron and nickel lie on the opposite sides of the Bethe-Slater curve, exchange interaction between Fe-Ni atomic pair is stronger than that of Fe-Fe atomic pair. Which means, $J_{Fe\text{-}Ni} > J_{Fe\text{-}Fe} > J_{Ni\text{-}Ni}$ in FeNiPC glasses [62, 72]. As the nickel content increases, the number of Fe-Ni atomic pair rises, and this results in an increase in Curie temperature, following the left-hand side of the Bethe-Slater curve.

3.4 MA-11-Fluxed ($Fe_{60}Ni_{20}P_{13}C_7$)

This ribbon was synthesized prior to the unfluxed one, as mentioned in Chapter 3.3. The details regarding the casting process and the properties of its master alloy can be found in Table 2.2. The high temperature DSC trace of the as cast ribbon is shown in Figure 3.15.

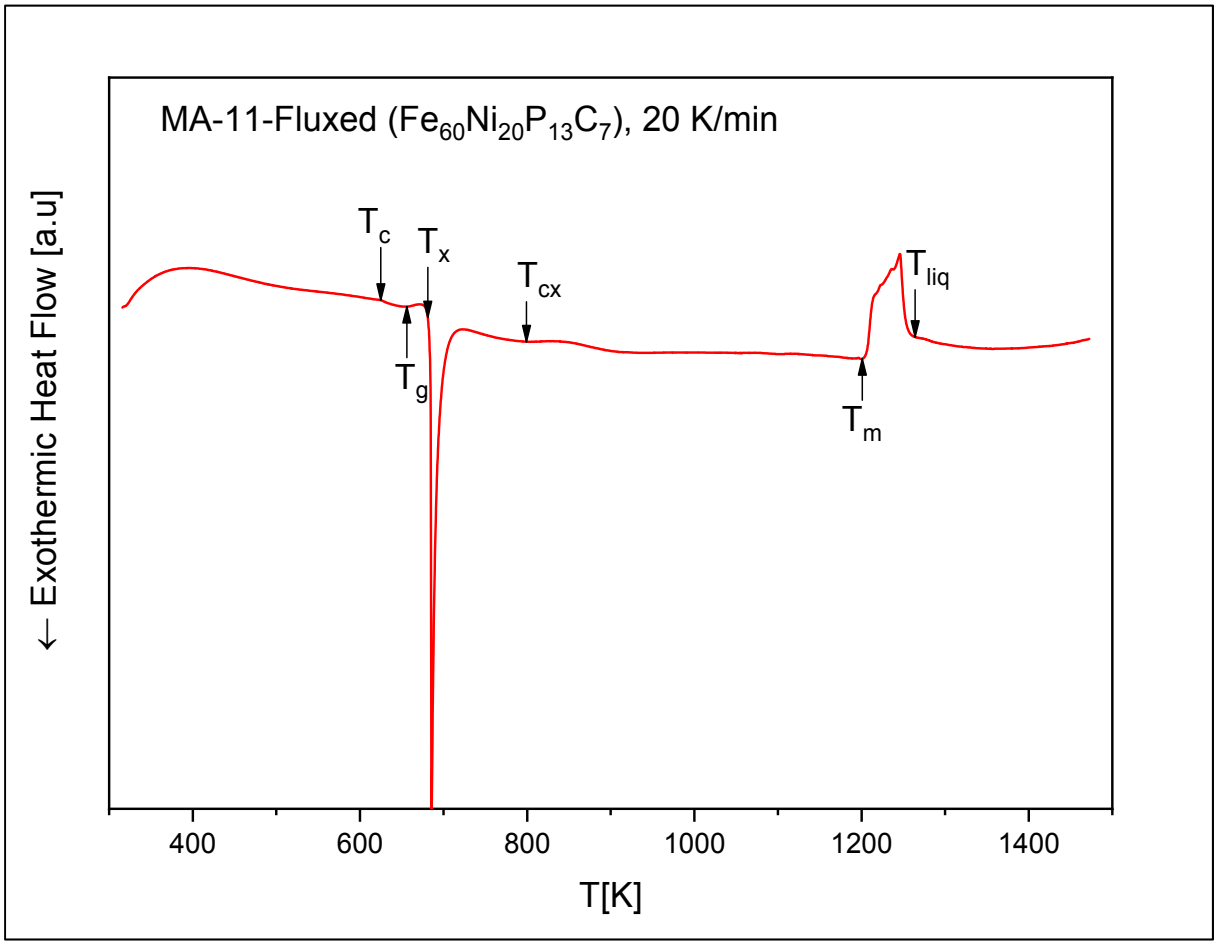

Figure 3.15: DSC trace of as-cast MA-11-Fluxed ($Fe_{60}Ni_{20}P_{13}C_7$) glassy ribbon.

Master Alloy	Composition	T_c [K]	T_g [K]	T_x [K]	T_{liq} [K]	ΔT_x [K]	T_{rg}
MA-11-Fluxed	$Fe_{60}Ni_{20}P_{13}C_7$	625	657	680	1264	23	0.519

Table 3.4: Curie temperature, T_c, glass transition, T_g, crystallization temperature T_x, liquidus temperature, T_{liq}, extension of the supercooled liquid region, ΔT_x, and reduced glass transition temperature, T_{rg} of the MA-11-Fluxed ($Fe_{60}Ni_{20}P_{13}C_7$) metallic glass ribbon.

The heating curve of the fluxed ribbon exhibits some differences in crystallization and melting events compared to the unfluxed one. This ribbon exhibits a single-stage eutectic crystallization event; however, its melting peak has a peculiar shape and the melting behavior is definitely not eutectic. It can be stated that fluxing treatment has changed the crystallization and melting behaviors in the

opposite directions compared to the unfluxed ribbon. Thermal properties of the sample, ΔT_x and T_{rg} values are presented in Table 3.4. As seen from the table, T_g and T_x were slightly increased (both 4 K) in respect to the unfluxed ribbon. Furthermore, because of the higher T_{liq}, reduced glass transition temperature of the alloy is decreased. Extent of the supercooled liquid region is unchanged. Regarding only the T_{rg} parameter, it can be stated that GFA of the alloy was slightly decreased. Apparently, fluxing treatment has changed the metalloid contents and possibly a small amount of boron has incorporated into the alloy. Another possible factor might be the utilization of Fe_3C precursor instead of graphite as carbon source.

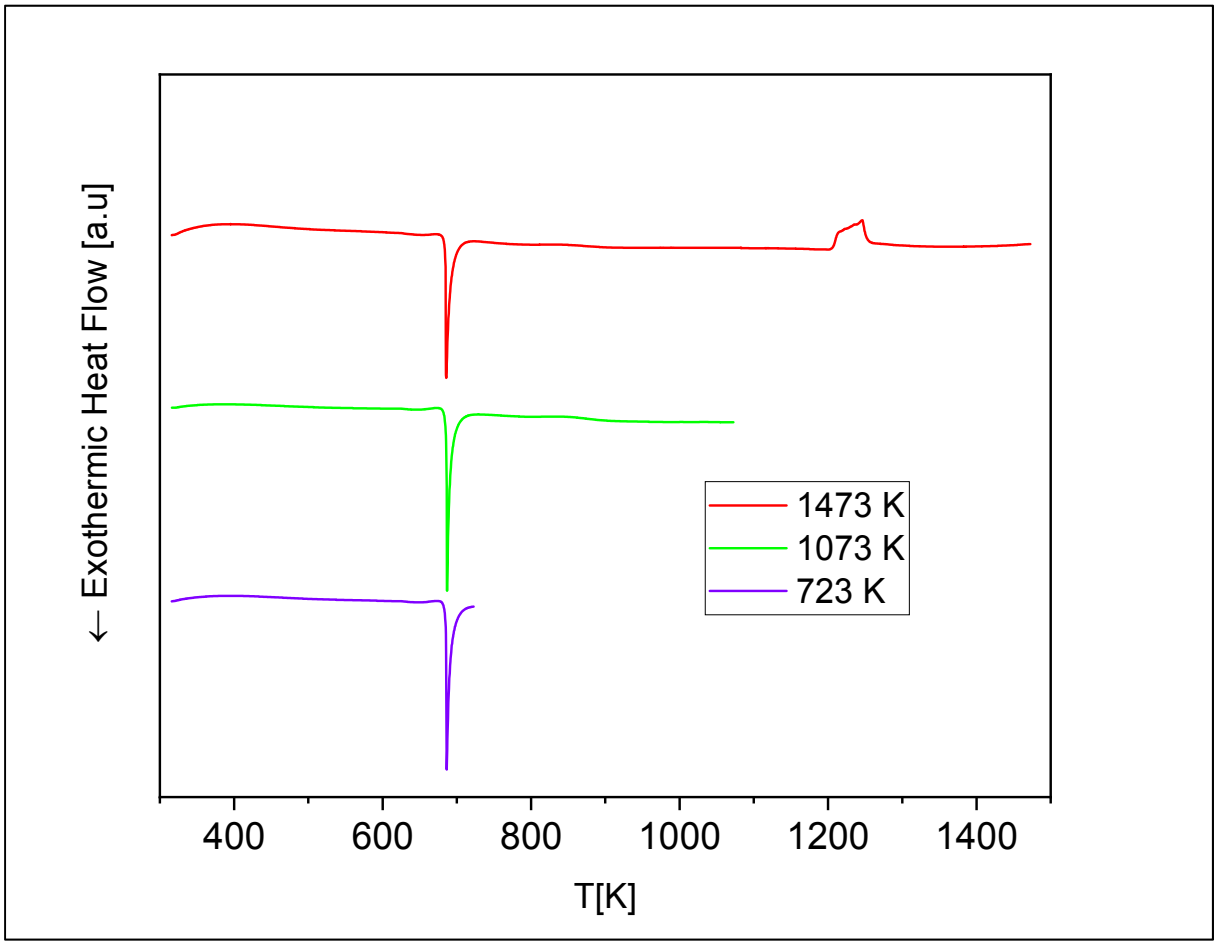

Figure 3.16: DSC traces of MA-11-Fluxed ($Fe_{60}Ni_{20}P_{13}C_7$) metallic glass ribbon, subjected to non-isothermal crystallization annealing at 20 K/min.

If the difference in the casting parameters are considered, this ribbon was cast at a temperature which was 200 K lower than the unfluxed one, and the wheel speed was 30 Hz instead of 40 Hz. Thus, it can be expected that the viscosity of the melt was higher, and the rate of cooling was slower, in comparison to the unfluxed ribbon. Higher viscosity might have resulted in a difference in the distribution of the atoms, because of the increased difficulty of atomic mobility. On the other hand, slower rate of cooling might have promoted the nanocrystallization, which in turn effects the SRO of the amorphous matrix.

The DSC traces of the non-isothermal crystallization annealing and the initial high temperature DSC curve of the MA-11-Fluxed ($Fe_{60}Ni_{20}P_{13}C_7$) metallic glass ribbon are depicted in Figure 3.16. Similar

to the unfluxed ribbon, these samples were subjected to XRD analysis and their diffraction patterns, along with the as-cast ribbons XRD pattern are shown in Figure 3.17.

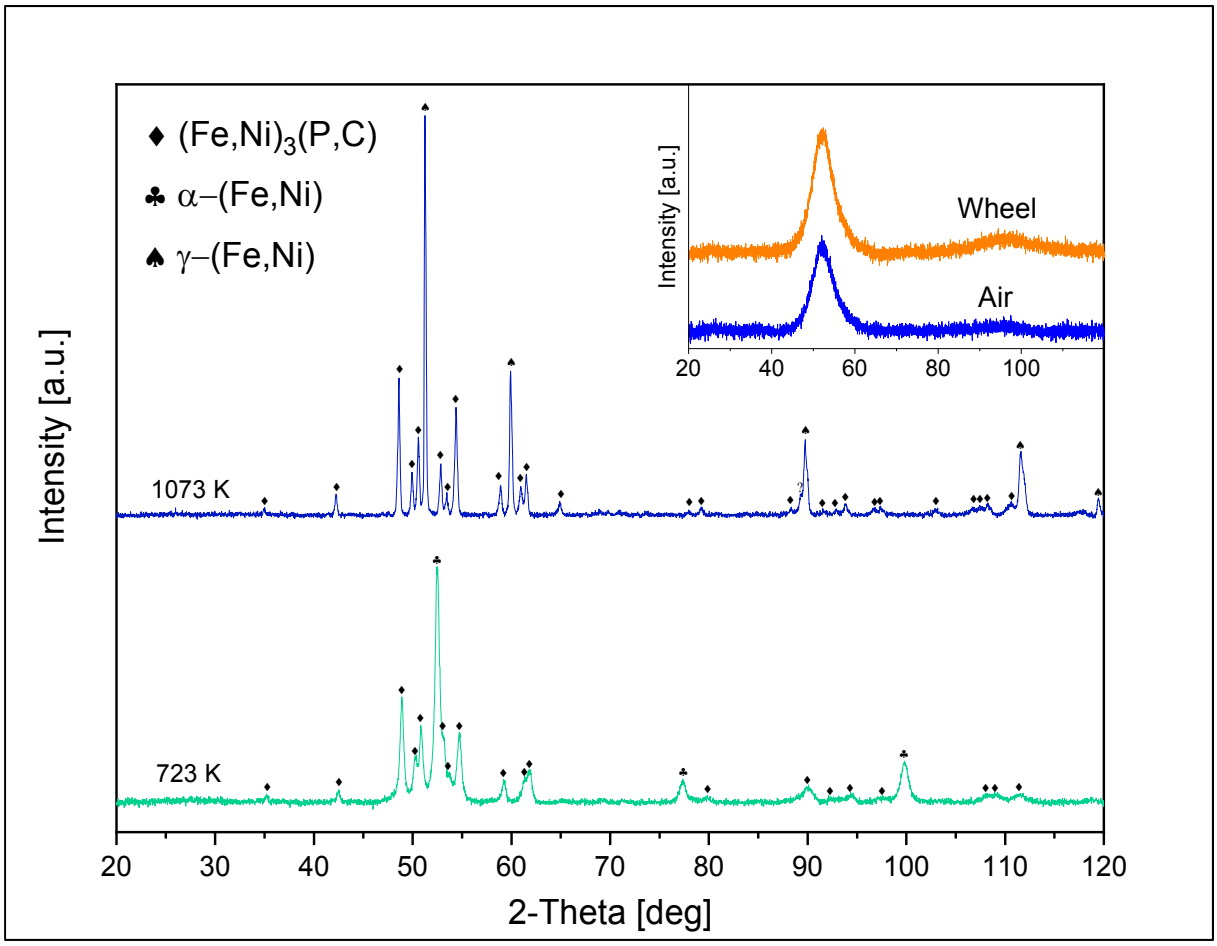

Figure 3.17: XRD patterns for MA-11-Fluxed ($Fe_{60}Ni_{20}P_{13}C_7$) glassy ribbon annealed up to different temperatures at 20 K/min and identified crystallization products. The inset shows the XRD pattern of the as-cast ribbon.

As seen from the figure, the sample heated up to 723 K (purple curve in Figure 3.16) crystallized single-staged (eutectic) to stable bcc α-(Fe,Ni) and stable body centered tetragonal $(Fe,Ni)_3(P,C)$ phases. Unlike the unfluxed ribbon, at this temperature no separate Fe_3C phase could be identified. Thus, the sample did not completely crystallize at this temperature since the broad diffraction maximum still can be seen.

The second sample heated up to 1073 K (green curve in Figure 3.16) exhibits γ-(Fe,Ni) and $(Fe,Ni)_3P$ phases and there are no Fe_3C, which is also different from the unfluxed sample. Because of the fluxing treatment, carbon content might have been decreased and thus, Fe_3C phase might have been destabilized. Moreover, the sample is fully crystallized at this temperature. Like the case in the unfluxed ribbon, the sample remains completely austenitic after it is cooled down to room temperature, following a martensitic α-(Fe,Ni) ↔ γ-(Fe,Ni) transformation. This indicates that the presence of metalloids greatly stabilizes γ-(Fe,Ni) phase, and the possible deviations from the nominal metalloid content and/or the potential B incorporation does not change this behavior.

Accordingly, the very broad endothermic peak after the crystallization event might correspond to this martensitic transformation and/or magnetic transformation of α-(Fe,Ni) phase, like the case in the unfluxed alloy. Considering the DSC traces of MA-18 ($Fe_{60}Ni_{20}P_{13}C_7$) and the present fluxed alloy, it

can be stated that all the Fe atoms definitely form a solid solution with Ni, since in the both DSC curves there are no endothermic peaks at higher temperatures, which may correspond to allotropic or magnetic transformation of α-Fe(P,C) solid solution without any Ni.

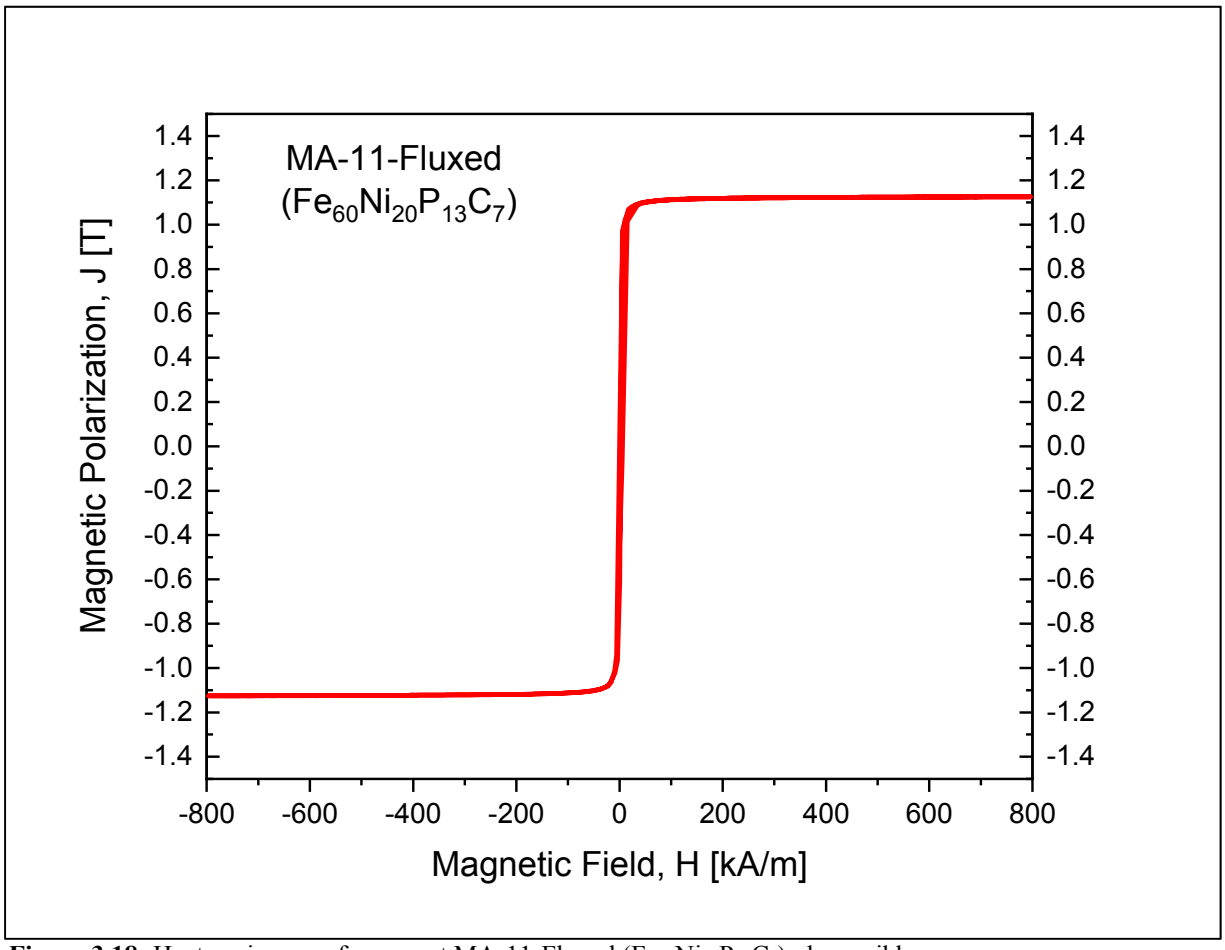

Figure 3.18: Hysteresis curve for as-cast MA-11-Fluxed ($Fe_{60}Ni_{20}P_{13}C_7$) glassy ribbon.

In Figure 3.18, the room temperature magnetic polarization of the as-cast MA-11-Fluxed ($Fe_{60}Ni_{20}P_{13}C_7$) glassy ribbon under an applied field of 800 kA/m is shown. The fluxed sample exhibits a J_s of 1.12 T, which is significantly larger than the unfluxed ribbon. Apparently, possible deviations from the nominal metalloid content have a strong effect on the saturation polarization.

If we assume that overall metalloid content was decreased, one can expect that the magnetic polarization would increase, because of the less charge transfer from metalloids to the magnetic elements. However, the difference in J_s seems to be too much for this kind of an interpretation. Therefore, this increase might have been occurred most likely as a result of nanoscale α-Fe precipitation, promoted by the slower rate of cooling.

On the other hand, Curie temperature of the glassy phase, T_c, seems to be increased dramatically (25 K) after the fluxing treatment in comparison to the unfluxed ribbon. It is difficult to ascertain this difference between two samples from our experimental data, since they belong to different master alloys and their casting parameters are quite different. Nevertheless, some crude assumptions can be made: It is well known that in Fe-based metallic glasses, Curie temperature decreases as the Fe-Fe interatomic distance decreases [60-62, 78]. It means that, if the metalloid content decreases, exchange interaction between magnetic Fe atoms decreases, approaching to the paramagnetic γ-Fe structure in Bethe-Slater curve. This has also been reported for FePC system [29]. Accordingly, if we assume that

overall metalloid content drops down because of the fluxing treatment, it is expected that T_c should also decrease. However, in our case T_c has increased. This might be explained as follows: Even though $J_{Fe\text{-}Fe}$ weakens with decreasing interatomic spacing of iron, $J_{Fe\text{-}Ni}$ should increase at the same time, since they lie at the opposite sides of the Bethe-Slater curve and they also get close to each other. Apparently, this increase in exchange interaction between Fe-Ni atoms overwhelms (remember $J_{Fe\text{-}Ni} > J_{Fe\text{-}Fe} > J_{Ni\text{-}Ni}$ in FeNiPC glasses) the decreasing Fe-Fe exchange forces and thus, T_c increases with decreasing metalloid content.

Further, Graham et al. [79] has reported that, amorphous alloys containing two or more transition metal elements tend to have spread-out Curie temperatures rather than a well-defined T_c of the single transition-metal based amorphous alloys. He suggests that the spread in T_c results from chemical inhomogeneities, such as clustering and phase separation. Since the T_c is very sensitive to small variations in SRO, it is not surprising that there exists a significant difference between the fluxed and unfluxed ribbon, considering the difference in their crystallization events and products.

Finally, it is known that T_c is sensitive to the degree of relaxation and increases upon annealing [11]. Considering the lower casting temperature and the slower cooling rate of the fluxed ribbon, it can be expected that the fluxed ribbon is in a more relaxed state in comparison to the unfluxed one and thus, exhibits a higher Curie temperature.

3.5 MA-16 ($Fe_{60}Co_{20}P_{13}C_7$)

This amorphous ribbon was cast at 1423 K, the details of its master alloy and other casting parameters can be found in Table 2.2. The partial substitution of Co for Fe in Fe-based metallic glasses has been extensively studied [29, 56, 62, 65, 67, 68, 72, 78, 111, 121-123] because of the unique effect of cobalt on saturation magnetization, as the case in Fe-rich Fe-Co crystalline alloys. Additionally, $Fe_{80-x}Co_xP_{13}C_7$ alloy has been reported before [7, 109, 112, 124]. In Figure 3.19, high temperature DSC curve of the as-cast MA-16 ($Fe_{60}Co_{20}P_{13}C_7$) glassy ribbon is depicted.

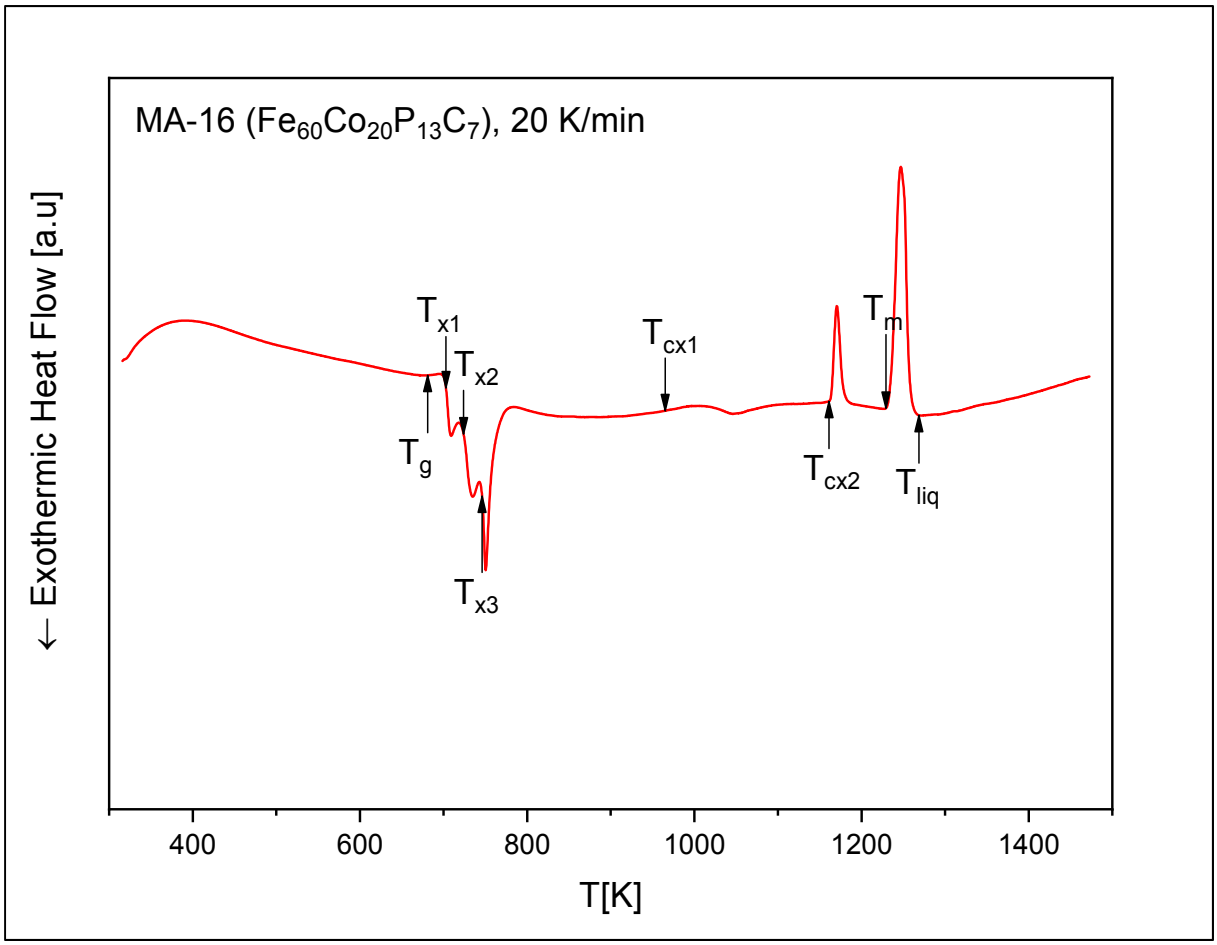

Figure 3.19: DSC trace of as-cast MA-16 ($Fe_{60}Co_{20}P_{13}C_7$) glassy ribbon.

Master Alloy	Composition	T_g [K]	T_{x1} [K]	T_{x2} [K]	T_{x3} [K]	T_{liq} [K]	ΔT_x [K]	T_{rg}
MA-16	$Fe_{60}Co_{20}P_{13}C_7$	679	702	724	746	1268	23	0.535

Table 3.5: Glass transition, T_g, crystallization temperatures T_{x1}, T_{x2} and T_{x3} liquidus temperature, T_{liq}, extension of the supercooled liquid region, ΔT_x, and reduced glass transition temperature, T_{rg} of the MA-16 ($Fe_{60}Co_{20}P_{13}C_7$) metallic glass ribbon.

As seen from the DSC trace, this alloy does not exhibit a Curie temperature in the amorphous state, and a clear glass transition temperature, T_g. Interestingly, it shows a three-staged crystallization event, which has not been reported before in the literature. After the multi-staged crystallization event, it presents a very broad endothermic peak, and then, again, a very sharp endothermic peak. This sharp endothermic peak is peculiar, and it will be discussed later. The melting behavior of the alloy seems eutectic, since it exhibits a relatively narrow endothermic peak for this event.

Thermal properties of the as-cast ribbon, ΔT_x and T_{rg} values are presented in Table 3.5. One can see that 20 at.% cobalt substitution has resulted in a slight increase in T_g (1 K) and also a slight decrease in T_{x1} (1 K) in comparison to the MA-17 ($Fe_{80}P_{13}C_7$) glassy ribbon, which in turn leads to a slightly narrower extent of the supercooled liquid region, ΔT_x. However, because of the depressed liquidus temperature, T_{liq}, reduced glass transition temperature, T_{rg} of the ribbon is higher than that of $Fe_{80}P_{13}C_7$ amorphous alloy. Therefore, it is not easy to predict the GFA of the alloy considering only these two parameters. Furthermore, our high temperature DSC device has an error limit of ∓ 2 K.

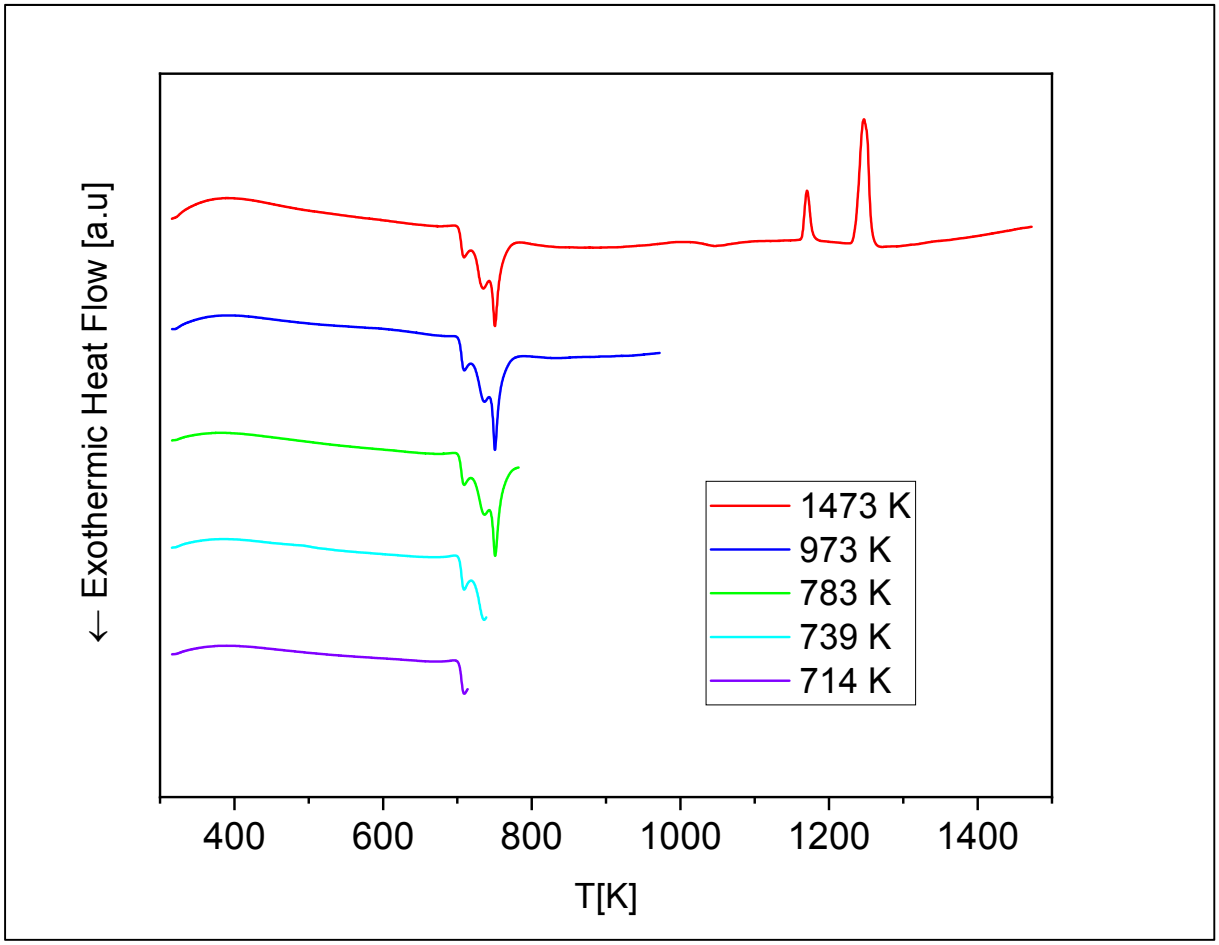

Figure 3.20: DSC traces of MA-16 ($Fe_{60}Co_{20}P_{13}C_7$) metallic glass ribbon, subjected to non-isothermal crystallization annealing at 20 K/min.

Xu et al. [7] has reported that in the case of $Fe_{80-x}Co_xP_{13}C_7$ BMGs, partial substitution of Co has initially increased the GFA of the alloy, that is, when x = 5 and x = 10, D_{max} has increased from 2 mm to 2.3 mm and 2.5 mm, respectively. However, with further increase in Co (x = 15 and x = 20) content, D_{max} has decreased to 2 mm and 1.8 mm respectively. Thus, it can be stated that 20 at.% Co substitution for Fe is expected to deteriorate the GFA of the system. In our case, slightly narrower ΔT_x value confirms this, however, T_{rg} value is the highest among the unfluxed ribbons. If we consider only the ΔT_x value and assume that the GFA is decreased, this can be explained by means of very small difference in the atomic size between Fe and Co, and the smaller negative heat of mixing of Co with P (−35.5 kJ/mol) and C (−42 kJ/mol), since both of which violate the principles of Inoue [1-4, 29] for a high GFA. It is also interesting that T_g and T_{x1} values are relatively close to that of MA-17 ($Fe_{80}P_{13}C_7$) glassy ribbon (T_g = 678 K and T_{x1} = 703 K).

Since the these two temperatures are mainly related to the atomic bonding strength between the alloy constituents, it should be expected that partial replacement of Fe by Co should have weakened the overall bonding strength and thus, T_g and T_{x1} should have been lower than that of MA-17 ($Fe_{80}P_{13}C_7$) glassy ribbon, just like the case in MA-18 ($Fe_{60}Ni_{20}P_{13}C_7$) ribbon. This anomalous behavior was explained by Xu et al. [7] through the possible existence of a special SRO of Fe_3Co type clusters, when the atomic ratio of Fe and Co is 3:1 in the alloy.

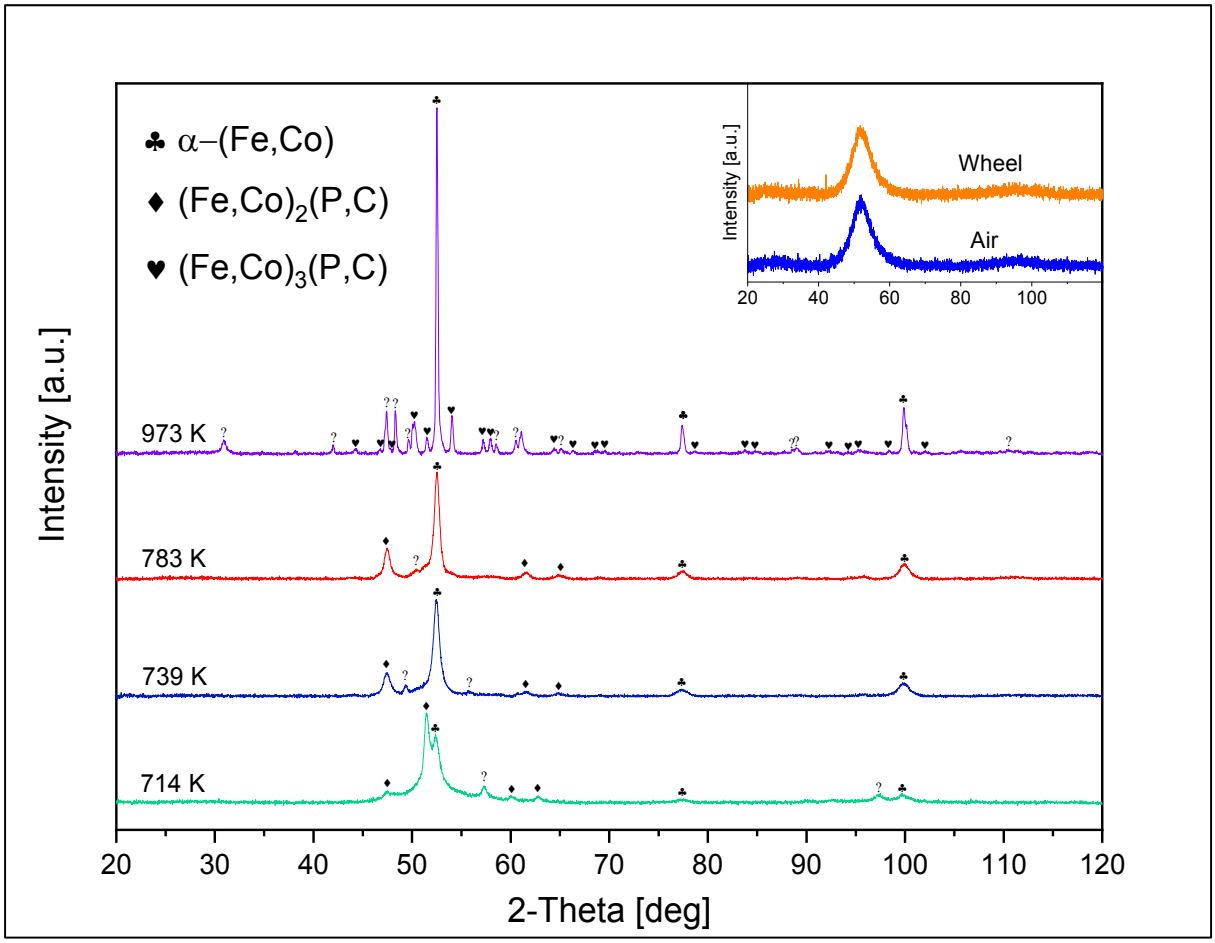

Figure 3.21: XRD patterns for MA-16 ($Fe_{60}Co_{20}P_{13}C_7$) glassy ribbon annealed up to different temperatures at 20 K/min and identified crystallization products. The inset shows the XRD pattern of the as-cast ribbon.

In figure 3.20, DSC traces of the non-isothermal crystallization annealing and the initial high temperature DSC curve of the MA-18 ($Fe_{60}Co_{20}P_{13}C_7$) metallic glass ribbon are shown. Within the case of the previous ribbons, these samples were subjected to XRD analysis and the resulting diffraction patterns, along with the as-cast ribbons XRD pattern are depicted in Figure 3.21.

As seen from the figure, identification of the crystalline products was difficult with this ribbon, and initial phases do not coincide with the previous findings [7, 112]. Further, some phases could not be identified at all. This most likely results from the unique three-staged crystallization event of the sample, which has not been observed before for this alloy composition. The sample heated up to 714 K (purple curve in Figure 3.20) exhibits $(Fe,Co)_2(P,C)$ metastable phase as primary crystallization product, and α-Fe,Co) solid solution, most likely with solute C, besides an unidentified metastable phase.

The second sample heated up to 739 K (turquoise curve in Figure 3.20) shows the same phases as the previous one, but this time the peaks of unidentified metastable phase appear at different angles. This might be the resulted from the second crystallization peak in the DSC trace.

The third sample heated up to 783 K (green curve in Figure 3.20) presents surprisingly the same metastable phases, and interestingly seems to still preserve a large fraction of amorphous matrix. At this temperature range, one usually expects more and prominent diffraction peaks in the XRD pattern, as the case in previously investigated ribbons. However, the pattern looks almost identical to the pattern below, with an exception of diminished peaks correspond to the unidentified metastable phase or phases.

Therefore, it can be deduced that the kinetics of crystallizations are definitely slower in comparison to the other unfluxed ribbons. The sample heated up to 973 K (blue curve in Figure 3.20) looks like completely crystallized, and presents stable α-(Fe,Co) solid solution and stable $(Fe,Co)_3(P,C)$ phases. Unfortunately, there still exist some unidentified peaks with high intensities.

Nevertheless, the findings of the XRD analysis at this temperature are not different than that of previously reported [7, 112] phases, but with an important difference. At those works, α-(Fe,Co) solid solution and $(Fe,Co)_3(P,C)$ phases were identified at a temperature which was slightly higher than the peak temperature of the first exothermic peak, and there are no further detailed structural investigations at higher temperatures present in the literature. In order to be sure about the crystallization sequence and the identities of the precipitated phases, TEM experiments must be conducted.

Meanwhile, the onset temperature of the broad endothermic peak, T_{cx1} (965 K) in Figure 3.19 might actually be the end of the final crystallization event, since at 783 K the sample was still significantly amorphous. If T_{cx1} is a Curie or allotropic transition temperature, it should be related to pure α-Fe or α-Fe with very few Co as solute. Then, the onset temperature of the sharp endothermic peak, T_{cx2} (1161 K) might correspond to α-(Fe,Co) ↔ γ-(Fe,Co) allotropic transition, even though it is ~100 K lower than that of 25 at.% Co in the binary Fe-Co phase diagram [118]. However, as the case in FeNiPC system, the presence of metalloids might have lowered the solid equilibrium temperature.

Moreover, at this alloy composition (1:3 atomic ratio of Co and Fe, respectively), magnetic Curie transition and the allotropic phase transition of bcc α-(Fe,Co) occurs simultaneously, and these two overlapping events might have resulted in a very sharp endothermic peak in the DSC trace. However, it is also unlikely that all the Co atoms form a bcc α-(Fe,Co) solid solution, considering the stable $(Fe,Co)_3(P,C)$ crystallization product. Thus, it might only be T_c of α-(Fe,Co) with lesser (~ 10 at.%) Co amount. On the other hand, this sharp peak might have been observed because of the melting event of

an unidentified phase (maybe an intermetallic) with a low melting point, since it looks very sharp in order to be interpreted as a result of a magnetic transition event.

In Figure 3.22, the room temperature magnetic polarization of the as-cast MA-16 ($Fe_{60}Co_{20}P_{13}C_7$) glassy ribbon under an applied field of 800 kA/m is depicted. This glassy ribbon exhibits a J_s of 1.28 T, which is very close to the $Fe_{80}P_{13}C_7$ ribbons.

There is discrepancy in the literature about Co replacement for Fe in the $Fe_{80-x}Co_xP_{13}C_7$ system (whether increases the saturation magnetization of the alloy or decreases it). Fujimori et al. [124] has reported in his early work that saturation magnetization decreases monotonically with Co substitution. On the other hand, Xu et al. [7] has postulated that the saturation magnetization first increases upon Co replacement up to 5 at.%, and then starts to decrease monotonically with increasing Co content. However, upon 20 at.% Co addition, the saturation magnetization was still slightly higher than that of the basic composition ($Fe_{80}P_{13}C_7$). Further, Meng et al. [109] has reported that saturation magnetization was increased up to 8 at.% Co addition, then decreased to a value which was slightly lower than the initial M_s of the basic composition upon 12 at.% Co replacement for Fe.

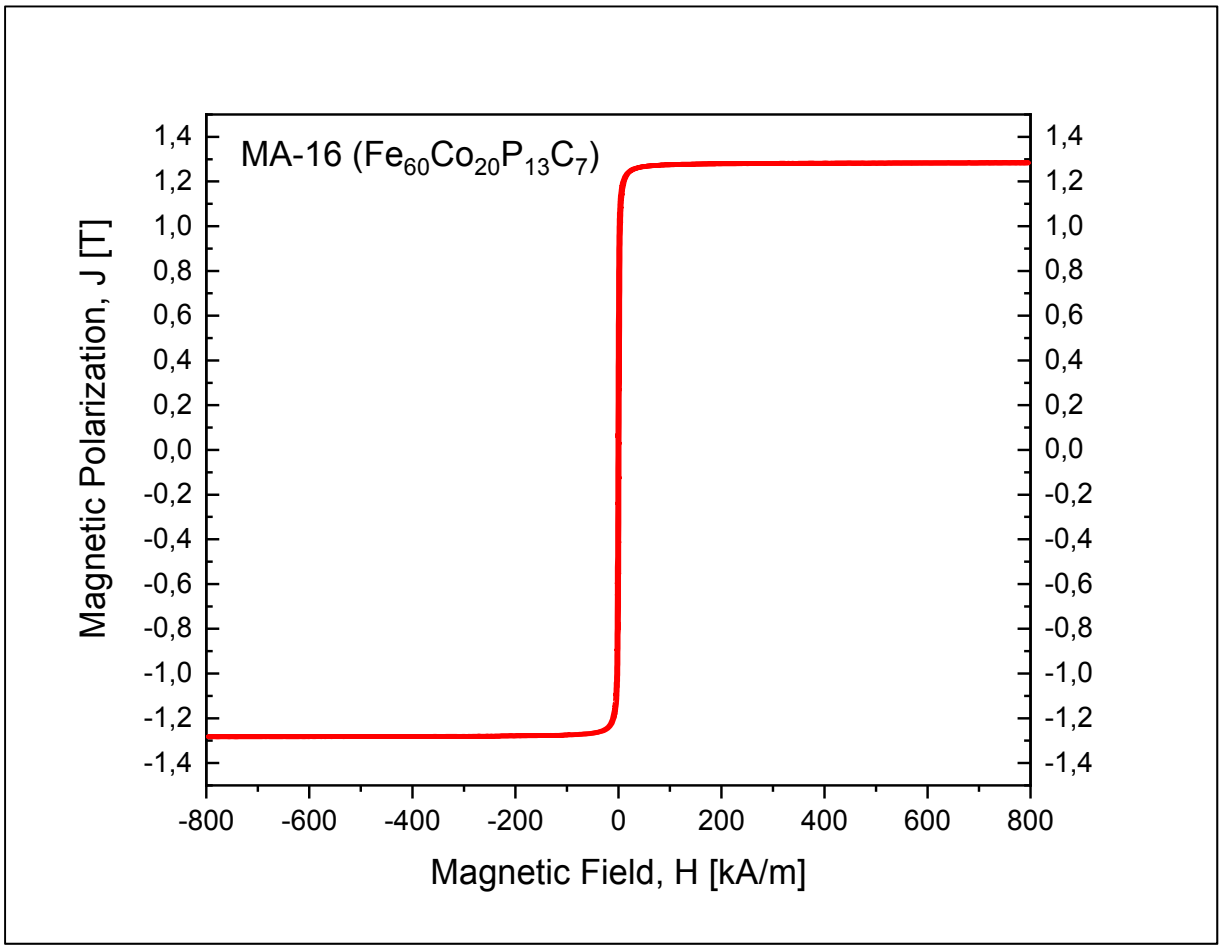

Figure 3.22: Hysteresis curve for as-cast MA-16 ($Fe_{60}Co_{20}P_{13}C_7$) glassy ribbon.

In our case, the saturation polarization is almost same with the basic composition. That means, transition from weak to strong ferromagnetism has already occurred. In the basic composition, Fe sites are weakly ferromagnetic, which means, the holes in the *3d* band are distributed over both spin-down and spin-up bands [72, 109].

In weak ferromagnetism, exchange splitting of the *3d* sub-bands, Δ, is smaller than E_0-E_F. In strong ferromagnetism, contrarily, $\Delta > E_0-E_F$, because all the iron site holes are present only in minority-spin (spin-down) band. With the addition of cobalt, a redistribution of the *3d* charge between the spin-up and spin-down bands occurs, because of the strong exchange interaction between Fe and Co atoms.

As the Co content rises, more and more Fe-Co pairs are generated, and eventually exchange splitting Δ becomes greater than E_0-E_F. In this state, the alloy is now strongly ferromagnetic, which means that mean magnetic moment of iron achieves its maximum value. Once $\Delta > E_0-E_F$ occurs, the magnetic moment of Fe becomes insensitive to its nearest neighbor type and number [72]. Thus, upon further increase in cobalt content, the average magnetic moment of the alloy decreases (remember Co is strongly ferromagnetic and thus its magnetic moment is constant), because of the lower magnetic moment of cobalt in respect to iron. Therefore, it can be stated that MA-16 ($Fe_{60}Co_{20}P_{13}C_7$) glassy ribbon is strongly ferromagnetic, as in the case of the MA-18 ($Fe_{60}Ni_{20}P_{13}C_7$) ribbon.

The increase in T_c upon Co addition has been previously reported for $Fe_{80-x}Co_xP_{13}C_7$ system [7, 109, 124], as well as for other Fe-based metallic glasses [56, 62, 65, 67, 68, 72, 78, 111, 121-123]. Similarly, because of the strong exchange interaction between Fe and Co atoms, partial substitution of Co for Fe results in an increase in the Curie temperature of the alloy. As the number of Fe-Co and atomic pairs increases, average exchange interaction between magnetic atoms in the alloy increases, since the Fe-Fe exchange interaction is weaker than that of Fe-Co and Co-Co atomic pairs. Similar to the crystalline Fe-Co alloys (see Figure 1.9), the extend of this increment is relatively large, and this results in a disappearance of the endothermic peak in the DSC trace, which corresponds to the Curie temperature in the amorphous state. That is, the magnetic transition temperature of these amorphous alloys exceeds their crystallization temperatures [7, 109, 124], which explains the absence of T_c in Figure 3.19.

3.6 MA-19 ($Fe_{60}Ni_{10}Co_{10}P_{13}C_7$)

This glassy ribbon was cast at 1458 K, the details of its master alloy and other casting parameters can be found in Table 2.2. It is important here to note that, this alloy has been synthesized for the first time. In Figure 3.23, high temperature DSC curve of the as-cast MA-19 ($Fe_{60}Ni_{10}Co_{10}P_{13}C_7$) glassy ribbon is depicted.

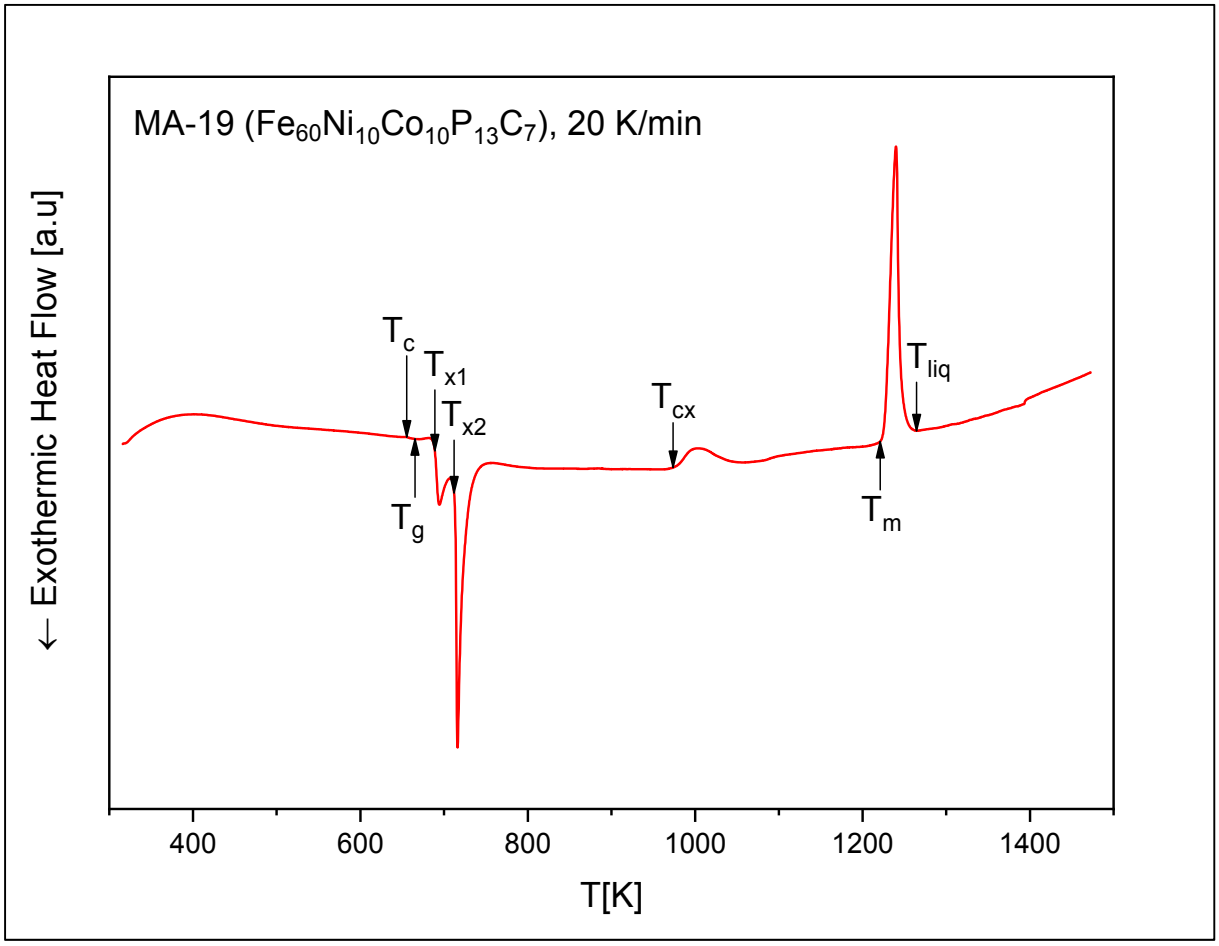

Figure 3.23: DSC trace of as-cast MA-19 ($Fe_{60}Ni_{10}Co_{10}P_{13}C_7$) glassy ribbon.

Master Alloy	Composition	T_c [K]	T_g [K]	T_{x1} [K]	T_{x2} [K]	T_{liq} [K]	ΔT_x [K]	T_{rg}

MA-19	$Fe_{60}Ni_{10}Co_{10}P_{13}C_7$	655	665	689	712	1264	24	0.526

Table 3.6: Curie temperature, T_c, glass transition, T_g, crystallization temperatures T_{x1} and T_{x2}, liquidus temperature, T_{liq}, extension of the supercooled liquid region, ΔT_x, and reduced glass transition temperature, T_{rg} of the MA-19 ($Fe_{60}Ni_{10}Co_{10}P_{13}C_7$) metallic glass ribbon.

As seen from the figure, high temperature DSC trace of this novel alloy is interestingly similar to that of the MA-17 ($Fe_{80}P_{13}C_7$) glassy ribbon. It exhibits a clear glass transition event, a two-staged crystallization event, and Curie temperatures in both states. Its melting event seems eutectic. In Table 3.6, thermal properties of the sample, ΔT_x and T_{rg} values are presented.

From Table 3.6 one can see that the simultaneous substitution of Ni and Co for Fe has resulted in a decrease (13 K) in T_g in comparison to $Fe_{80}P_{13}C_7$ alloy (T_g = 678 K). The extent of this decrease in glass transition temperature is smaller than that of $Fe_{60}Ni_{20}P_{13}C_7$ alloy (T_g = 653 K). Considering the T_g (679 K) of the $Fe_{60}Co_{20}P_{13}C_7$ alloy, the replacement of 10 at.% Ni for Co also causes a decrease in glass transition temperature of the novel alloy.

Since there is a significant discrepancy [7, 109, 124] in the literature about the effect of Co addition on T_g for $Fe_{80}P_{13}C_7$ alloy, it can only be stated that addition of Ni strongly depresses T_g, but this effect is less prominent when it is added simultaneously with Co. The onset of crystallization temperature, T_x, is reduced 14 K in comparison to $Fe_{80}P_{13}C_7$ alloy (T_{x1} = 703 K). The extent of this reduction is smaller than that of $Fe_{60}Ni_{20}P_{13}C_7$ alloy (T_{x1} = 676 K) and larger than that of $Fe_{60}Co_{20}P_{13}C_7$ alloy (T_{x1} = 702 K). Interestingly, T_x of the new alloy resides at the arithmetic average (689 K) of $Fe_{60}Ni_{20}P_{13}C_7$ and $Fe_{60}Co_{20}P_{13}C_7$ alloys' crystallization temperatures.

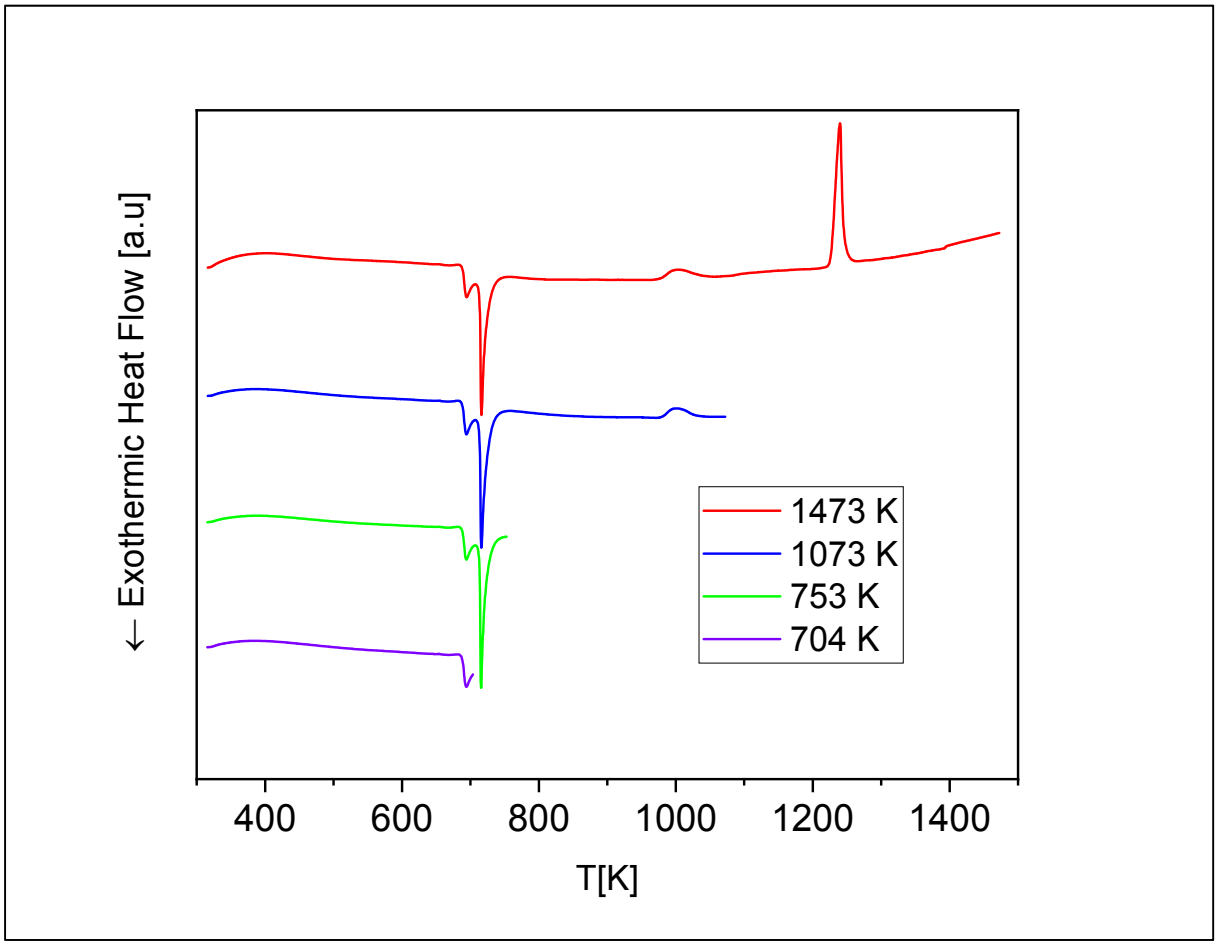

Figure 3.24: DSC traces of MA-19 ($Fe_{60}Ni_{10}Co_{10}P_{13}C_7$) metallic glass ribbon, subjected to non-isothermal crystallization annealing at 20 K/min.

Apparently, the simultaneous substitution of same amount of Ni and Co, cancels out each other's effect on T_x for $Fe_{80}P_{13}C_7$ system. On the other hand, depression of the liquidus temperature is almost same with the $Fe_{60}Co_{20}P_{13}C_7$ alloy. According to these temperatures, the extend of the SCLR is 24 K, which is wider than those of $Fe_{60}Co_{20}P_{13}C_7$ and $Fe_{60}Ni_{20}P_{13}C_7$ alloys, but narrower than that of $Fe_{80}P_{13}C_7$ alloy. However, reduced glass transition temperature of the alloy is 0.526 and this value is lower than that of $Fe_{60}Co_{20}P_{13}C_7$ alloy. As a result, considering only the ΔT_x and T_{rg} values, it is not possible to predict the GFA of this new alloy. However, this is not surprising and rises from the fact that Fe, Co, Ni elements are neighbors in the periodic system, and they exhibit no big differences in their atomic sizes and electronegativities. Moreover, the mixing enthalpies of these elements with the metalloids in the system are also close to each other's.

Nevertheless, as can be seen from the Table 2.2, it was possible to obtain glassy ribbons from this alloy in a large temperature window. The casting temperatures were between 1298 K and 1458 K and all casting attempts were successful. Since the rate of cooling was held constant in all of these attempts, this indicates that this novel alloy does not necessarily need a high cooling rate to form a glassy structure.

Therefore, it can be stated that the GFA of the alloy is higher in respect to FePC, FeNiPC and FeCoPC alloys. This prediction is in agreement with the first principle of Inoue: The formation of glass becomes easier with an increasing number of components in the alloy system. This can be basically

explained with the increased entropy of the alloy and the increased number of competing crystalline phases.

In Figure 3.24, DSC traces of the non-isothermal crystallization annealing and the initial high temperature DSC curve of the MA-19 ($Fe_{60}Ni_{10}Co_{10}P_{13}C_7$) metallic glass ribbon are depicted. Like the previous ribbons, these samples were subjected to XRD analysis and the resulting diffraction patterns, along with the as-cast ribbons XRD pattern are depicted in Figure 3.25.

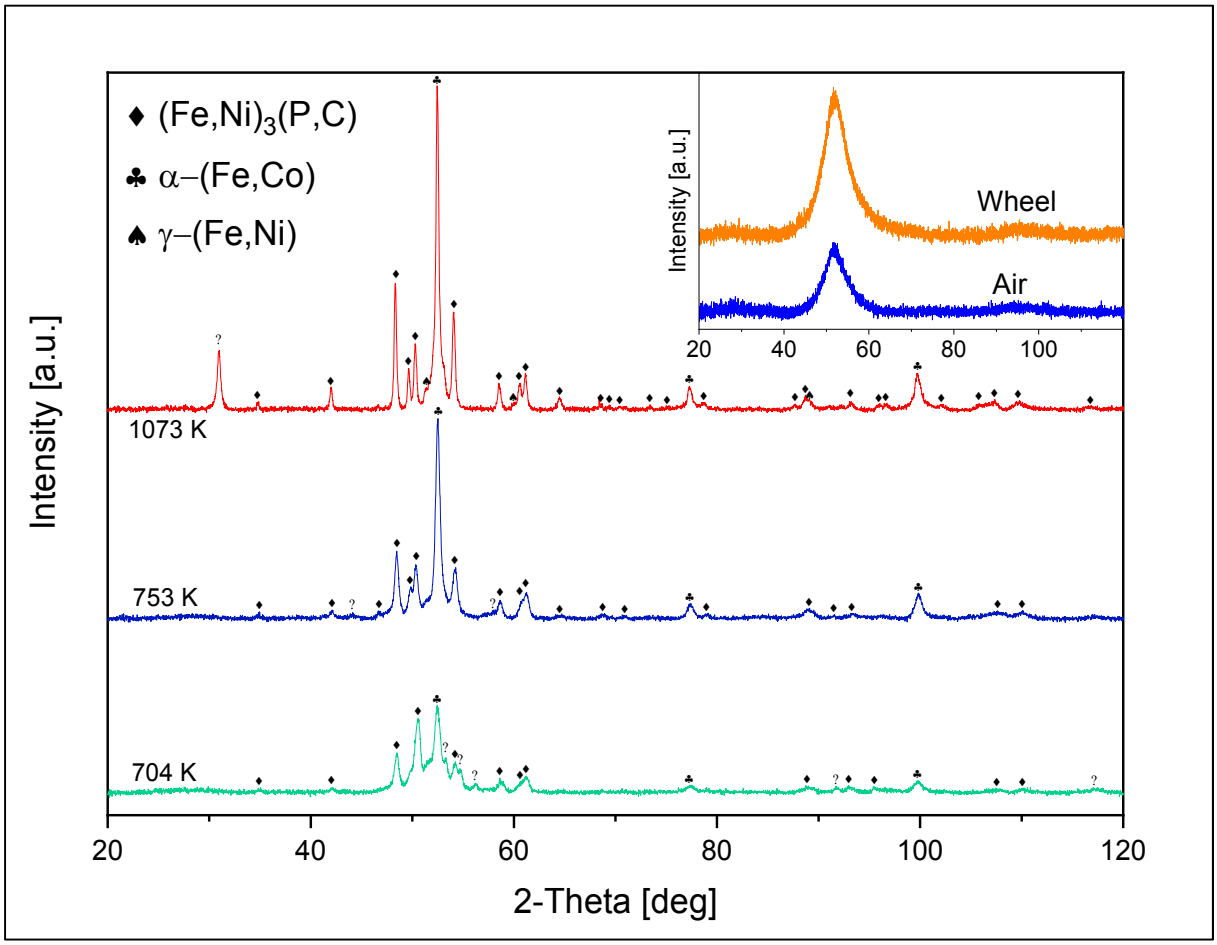

Figure 3.25: XRD patterns for MA-19 ($Fe_{60}Ni_{10}Co_{10}P_{13}C_7$) glassy ribbon annealed up to different temperatures at 20 K/min and identified crystallization products. The inset shows the XRD pattern of the as-cast ribbon.

As seen from Figure 3.25, the sample heated up to 704 K (purple DSC curve in Figure 3.24) exhibits as primary crystallization product of $(Fe,Ni)_3(P,C)$ phase. Further, α-(Fe,Co) solid solution with solute (C,P) has also started to precipitate. At this temperature, the sample seems to preserve its amorphous matrix.

The next sample which was heated up to 753 K (green DSC trace in Figure 3.24) exhibits the same crystalline phases, but some unidentified diffraction peaks from the first exothermic event have disappeared. Since there exists no new crystalline phase, bcc α-(Fe,Co) with solute (P,C) should have precipitated as a product of second large exothermic event. But probably because of the temperature overshoot of the DCS device, it has also been found in previous stage of crystallization.

The last sample was heated up to 1073 K (blue DSC curve in Figure 3.24) also exhibits the same phases and surprisingly, fcc γ-(Fe,Ni) solid solution as well. Terminal crystallization products do not include any separate Fe_3C, Co_3C or Ni_3C phases, as in the case of MA-16 ($Fe_{60}Co_{20}P_{13}C_7$) glassy ribbon. This implies that C atoms have to reside mostly in $(Fe,Ni)_3(P,C)$ phase, because C has a very limited solubility in bcc α-(Fe,Co) solid solution. As the room temperature iron phase is bcc α-(Fe,Co), it is clear that there are no Co atoms in $(Fe,Ni)_3(P,C)$ phase and all the Co atoms reside in bcc α-(Fe,Co) crystallization product.

Meanwhile, 10 at.% Ni content in the alloy is probably too much to be completely consumed in $(Fe,Ni)_3(P,C)$ phase. That means, the remaining Ni atoms should first form a bcc α-(Fe,Ni) solid solution. Later, upon heating, first martensitic α-(Fe,Ni) ↔ γ-(Fe,Ni) transformation must have occurred, and then during cooling down to room temperature, γ-(Fe,Ni) phase must have undergone a martensitic transformation again in α-(Fe,Ni) solid solution. However, because of the low Ni amount in composition, M_f temperature should be lower than the room temperature, and this should give rise to a mixed phase region, namely, α-(Fe,Ni) and γ-(Fe,Ni) solid solutions. The coexistence of these phases at room temperature might explain the relatively broad bottom part of the main diffraction peak corresponding to α-(Fe,Co) phase.

Further, onset temperature of the endothermic peak (973 K) could be explained as following. Considering the atomic ratio of Fe and Co (1:6) in the alloy, this temperature is way too low to be predicted as Curie temperature of α-(Fe,Co) or α-(Fe,Co) ↔ γ-(Fe,Co) allotropic transformation temperature. Moreover, there is not a sharp peak to see around 1160 K in as the case of MA-16 ($Fe_{60}Co_{20}P_{13}C_7$) glassy ribbon.

Thus, this peak might correspond to α ↔ γ martensitic transformation of α-(Fe,Ni) solid solution. That is, because of the lower Ni amount in the alloy in comparison to the MA-18 ($Fe_{60}Ni_{20}P_{13}C_7$) and MA-11-Fluxed ($Fe_{60}Ni_{20}P_{13}C_7$) ribbons, A_s and A_f temperatures of the present ribbon should have been shifted to higher temperatures. Definitely, more detailed structural investigations with the help of TEM studies must be made in order to correctly identify this novel alloy crystallization products and their sequence.

In Figure 3.26, the room temperature magnetic polarization of the as-cast MA-19 ($Fe_{60}Ni_{10}Co_{10}P_{13}C_7$) glassy ribbon under an applied field of 800 kA/m is depicted. As seen from the figure, this new alloy exhibits a J_s of 1.11 T.

This value is lower than that of $Fe_{80}P_{13}C_7$ and $Fe_{60}Co_{20}P_{13}C_7$ alloys, but higher than the J_s value of $Fe_{60}Ni_{20}P_{13}C_7$ alloy. Apparently, the simultaneous substitution of Ni and Co has greatly reduced the average magnetic moment of the alloy. Even though 10 at.% Co addition should have initially increased

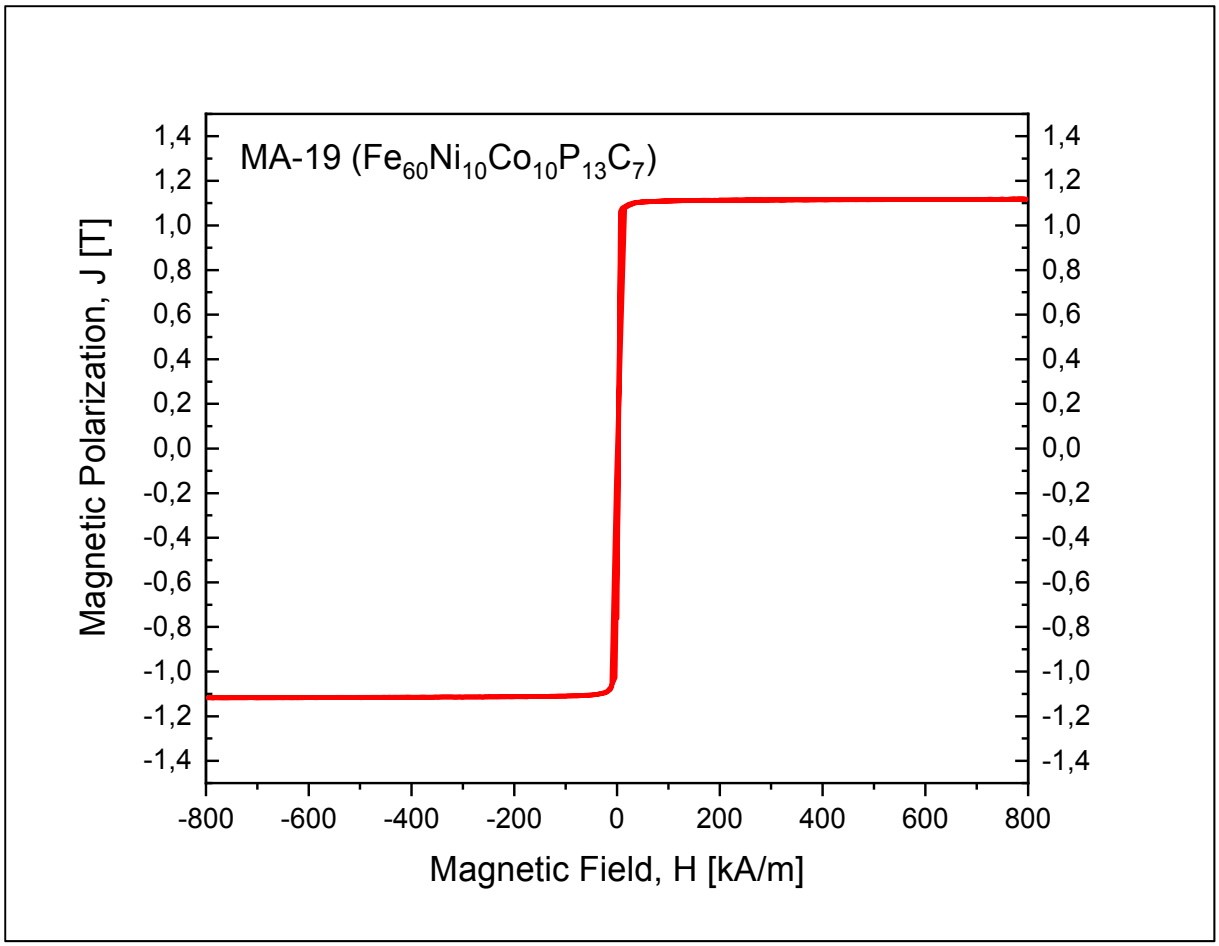

Figure 3.26: Hysteresis curve for as-cast MA-19 ($Fe_{60}Ni_{10}Co_{10}P_{13}C_7$) glassy ribbon.

the mean magnetic moment of Fe because of the strong exchange interaction between Co and Fe, the lower magnetic moment of Co and the Ni has suppressed this increase in mean magnetic moment of Fe atoms. Meanwhile, Curie temperature of the new alloy (655 K) is greatly increased in comparison to the $Fe_{80}P_{13}C_7$ (591 K) and $Fe_{60}Ni_{20}P_{13}C_7$ (599 K) alloys. This again results from the stronger exchange interaction between Fe and Co atoms. Further, Fe-Ni atomic pairs also contribute to this increment. However, because of the smaller exchange interaction of Fe-Ni in comparison to Fe-Co, T_c of the new alloy is lower than that of $Fe_{60}Co_{20}P_{13}C_7$ alloy, which exceeds its crystallization temperature.

3.7 MA-15 ($Fe_{60}Co_{15}Ni_5P_{13}C_7$)

This novel glassy alloy was cast at 1323 K, the details of its master alloy and other casting parameters can be found in Table 2.2. In Figure 3.27, high temperature DSC curve of the as-cast MA-15 ($Fe_{60}Co_{15}Ni_5P_{13}C_7$) glassy ribbon is depicted. As seen from the figure, this new alloy exhibits a clear glass transition temperature, T_g, a three-staged crystallization event and four endothermic events after its crystallization. Its melting behavior indicates that the alloy composition is close to eutectic point, like $Fe_{60}Ni_{10}Co_{10}P_{13}C_7$ glassy ribbon. This ribbon shows no Curie temperature in amorphous state.

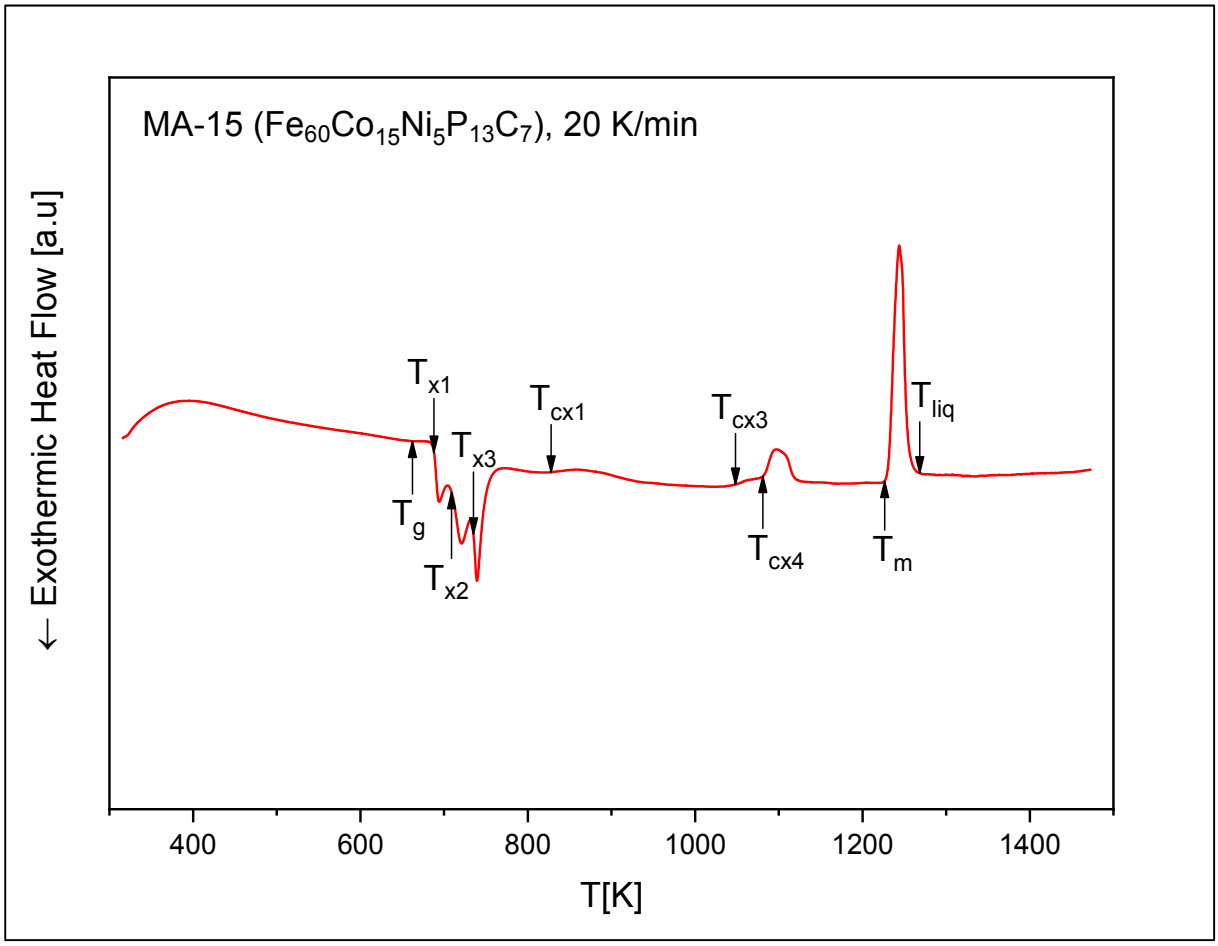

Figure 3.27: DSC trace of as-cast MA-15 ($Fe_{60}Co_{15}Ni_5P_{13}C_7$) glassy ribbon.

Master Alloy	Composition	T_g [K]	T_{x1} [K]	T_{x2} [K]	T_{x3} [K]	T_{liq} [K]	ΔT_x [K]	T_{rg}
MA-15	$Fe_{60}Co_{15}Ni_5P_{13}C_7$	662	688	709	735	1268	26	0.522

In Table 3.7, thermal properties of the sample, ΔT_x and T_{rg} parameters are shown. This new alloy

Table 3.7: Glass transition, T_g, crystallization temperatures T_{x1}, T_{x2} and T_{x3} liquidus temperature, T_{liq}, extension of the supercooled liquid region, ΔT_x, and reduced glass transition temperature, T_{rg} of the MA-15 ($Fe_{60}Co_{15}Ni_5P_{13}C_7$) metallic glass ribbon.

exhibits a slightly lower glass transition temperature compared to that of $Fe_{60}Ni_{10}Co_{10}P_{13}C_7$ alloy (665 K). This result is surprising, since it can be expected that T_g of the new alloy should be higher than that of $Fe_{60}Ni_{10}Co_{10}P_{13}C_7$ alloy, because $Fe_{60}Co_{15}Ni_5P_{13}C_7$ alloy possesses less Ni and more Co amount. (Remember that $Fe_{60}Co_{20}P_{13}C_7$ alloy exhibits the highest T_g of 679 K and $Fe_{60}Ni_{20}P_{13}C_7$ alloy the lowest of 653 K)

However, it can be still deduced that even 5 at.% Ni addition strongly decreases T_g, regardless of the Co amount in the $Fe_{60}Co_{20-x}Ni_xP_{13}C_7$ system. Additionally, the depression of the T_{liq} is slightly lower (4 K) than $Fe_{60}Ni_{10}Co_{10}P_{13}C_7$ alloy. This should be related to lesser Ni amount in the composition, since $Fe_{60}Ni_{20}P_{13}C_7$ alloy has the lowest T_{liq} among the unfluxed ribbons.

On the other hand, the crystallization temperature is very close to that of $Fe_{60}Ni_{10}Co_{10}P_{13}C_7$ alloy (689 K). It can be seen that, T_x of the new alloy does not follow the same trend mentioned in Chapter 3.6 and it is insensitive to Ni amount, as long as 10 at.% Co present in the alloy. In summary, considering the $Fe_{60}Co_{20}P_{13}C_7$ alloy, 5 at.% Ni substitution for Co has reduced T_x and T_g of the new alloy by 13 K and 14 K, respectively. Accordingly, 10 at.% Ni addition has decreased T_x and T_g of the new alloy by 14 K and 17 K, respectively.

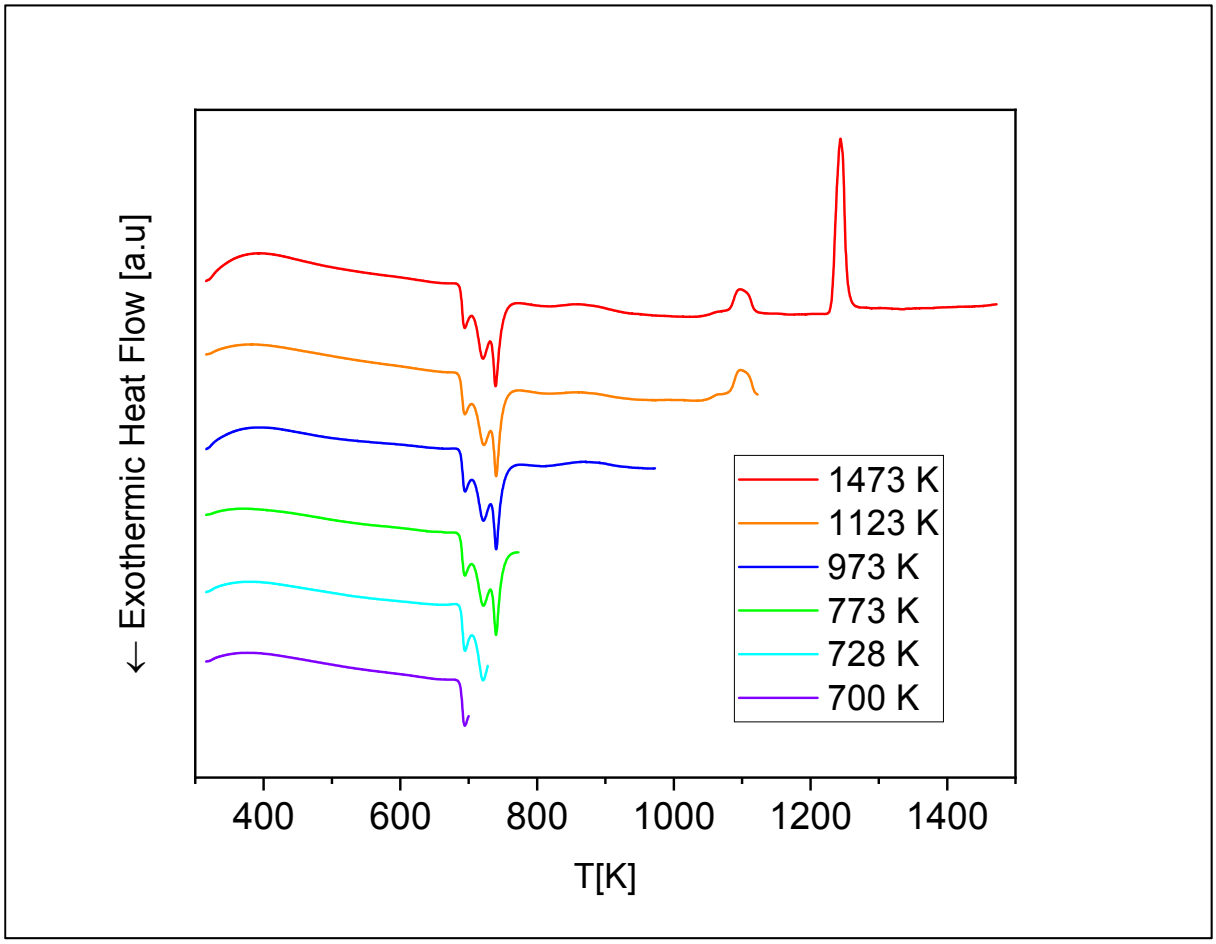

Figure 3.28: DSC traces of MA-15 ($Fe_{60}Co_{15}Ni_5P_{13}C_7$) metallic glass ribbon, subjected to non-isothermal crystallization annealing at 20 K/min.

These temperatures lead to a SCLR value of 26 K, which is very close to that of $Fe_{80}P_{13}C_7$ basic alloy (25 K). On the other hand, T_{rg} value of the new alloy is lower than those of $Fe_{80}P_{13}C_7$, $Fe_{60}Ni_{20}P_{13}C_7$,

$Fe_{60}Co_{20}P_{13}C_7$ and $Fe_{60}Ni_{10}Co_{10}P_{13}C_7$ alloys. Clearly, contradicting thermal properties do not give a good insight about the GFA of this novel alloy. However, the casting trials of this composition were mostly resulted in amorphous ribbons, as can be seen from Table 2.2. It was possible to synthesize glassy ribbons in a temperature range between 1298 K to 1373 K. Further, as it is going to be shown in next chapter, casting operation using the fluxed master alloy was also resulted in an amorphous ribbon. Therefore, it can be deduced that GFA of the new alloy was at least not low. This is not surprising if one considers the high number components in the alloy, like the case in $Fe_{60}Ni_{10}Co_{10}P_{13}C_7$ glassy ribbon.

In figure 3.28, DSC traces of the non-isothermal crystallization annealing and the initial high temperature DSC curve of the MA-15 ($Fe_{60}Co_{15}Ni_5P_{13}C_7$) metallic glass ribbon are depicted. Like the previous ribbons, these samples were subjected to XRD analysis and their diffraction patterns (except the sample heated up to 973 K), along with the as-cast ribbons XRD pattern are depicted in Figure 3.29.

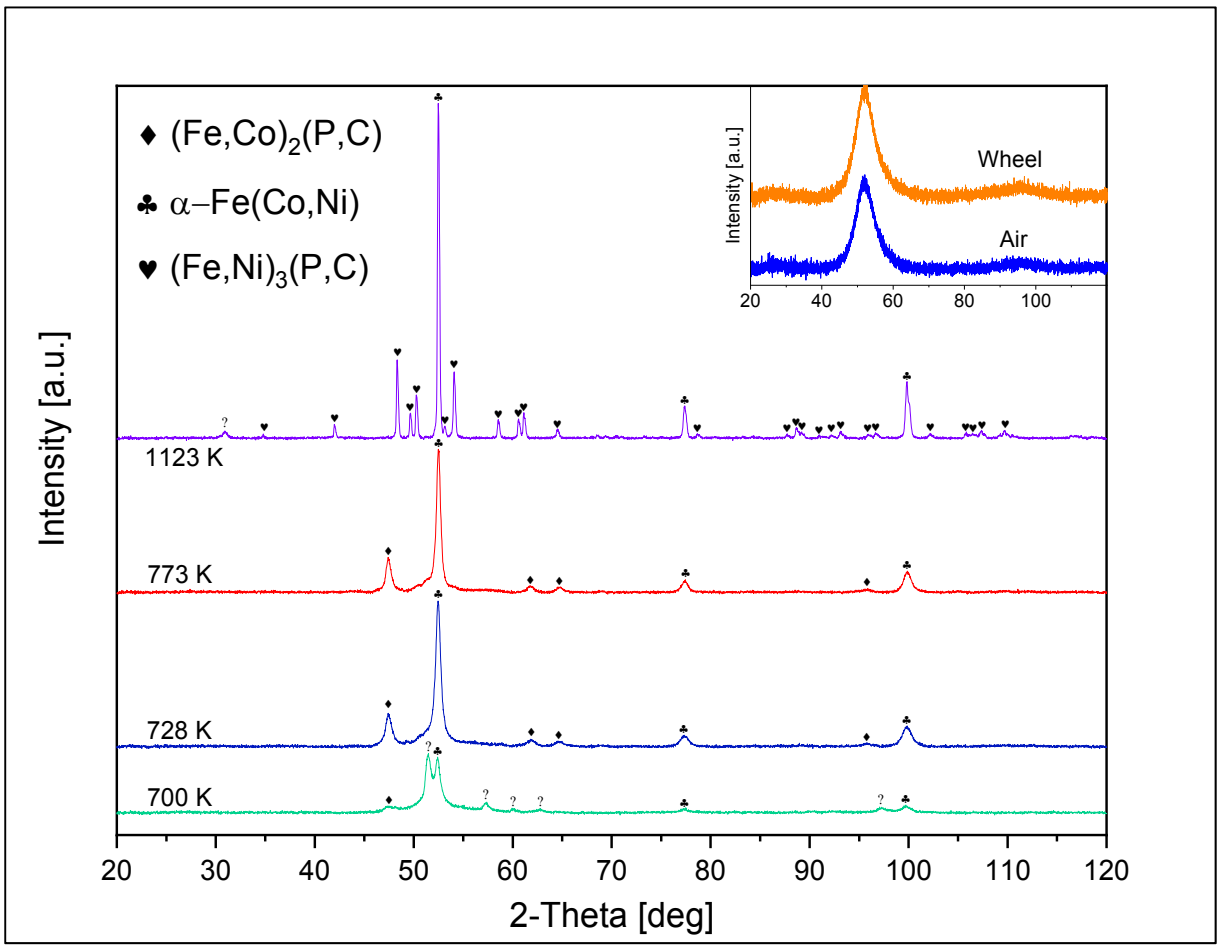

Figure 3.29: XRD patterns for MA-15 ($Fe_{60}Co_{15}Ni_5P_{13}C_7$) glassy ribbon annealed up to different temperatures at 20 K/min and identified crystallization products. The inset shows the XRD pattern of the as-cast ribbon.

As seen from Figure 3.29, the first sample heated up to 700 K (purple DSC curve in Figure 3.28) exhibits metastable $(Fe,Co)_2(P,C)$, stable α-Fe solid solution and some metastable unidentified phases. Since none of the identified crystallization products include Ni, α-Fe solid solution may be actually a bcc α-(Fe,Ni) phase with solutes P and C.

The second sample heated up to 728 K (turquoise DSC trace in Figure 3.28) shows no other crystallization product and identified phases are same as the previous sample. However, metastable phases disappeared at this temperature. This might be the reason of the presence of second exothermic peak in the crystallization event.

The third sample heated up to 773 K (green DSC curve in Figure 3.28) presents a diffraction pattern which is very similar to the previous sample, and it shows the same phases as well. Moreover, the broad diffraction maximum is still present, and this indicates that the sample has not been completely crystallized yet at this temperature. Then, the crystallization event might be actually lasted at onset temperature (865 K) of the first endothermic peak in Figure 3.27. Indeed, the next sample heated up to 973 K (blue DSC trace in Figure 3.27) was completely crystallized and it has showed exactly the same diffraction pattern as the sample heated up to 1123 K, thus it was not shown in Figure 3.29.

The last sample heated up to 1123 K (orange DSC curve in Figure 3.28) exhibits stable $(Fe,Ni)_3(P,C)$ phase and stable α-Fe solid solution. Since there is not a crystalline phase in the pattern which includes any cobalt, Co atoms should reside in bcc α-Fe solid solution, with solutes P and C. In order to form these phases, all the Ni atoms should be diffused off from the bcc α-(Fe,Ni) solid solution and crystallize along Fe, P and C atoms.

On the other hand, all of the Co atoms should diffuse into Fe to form bcc α-(Fe,Co) phase. Since the atomic radii of Fe, Co and Ni are close to each other, the rate of diffusion is expected to be sluggish. Further, it is well-known [73, 120] that the diffusivity of Fe and Ni in α is very low below 1073 K.

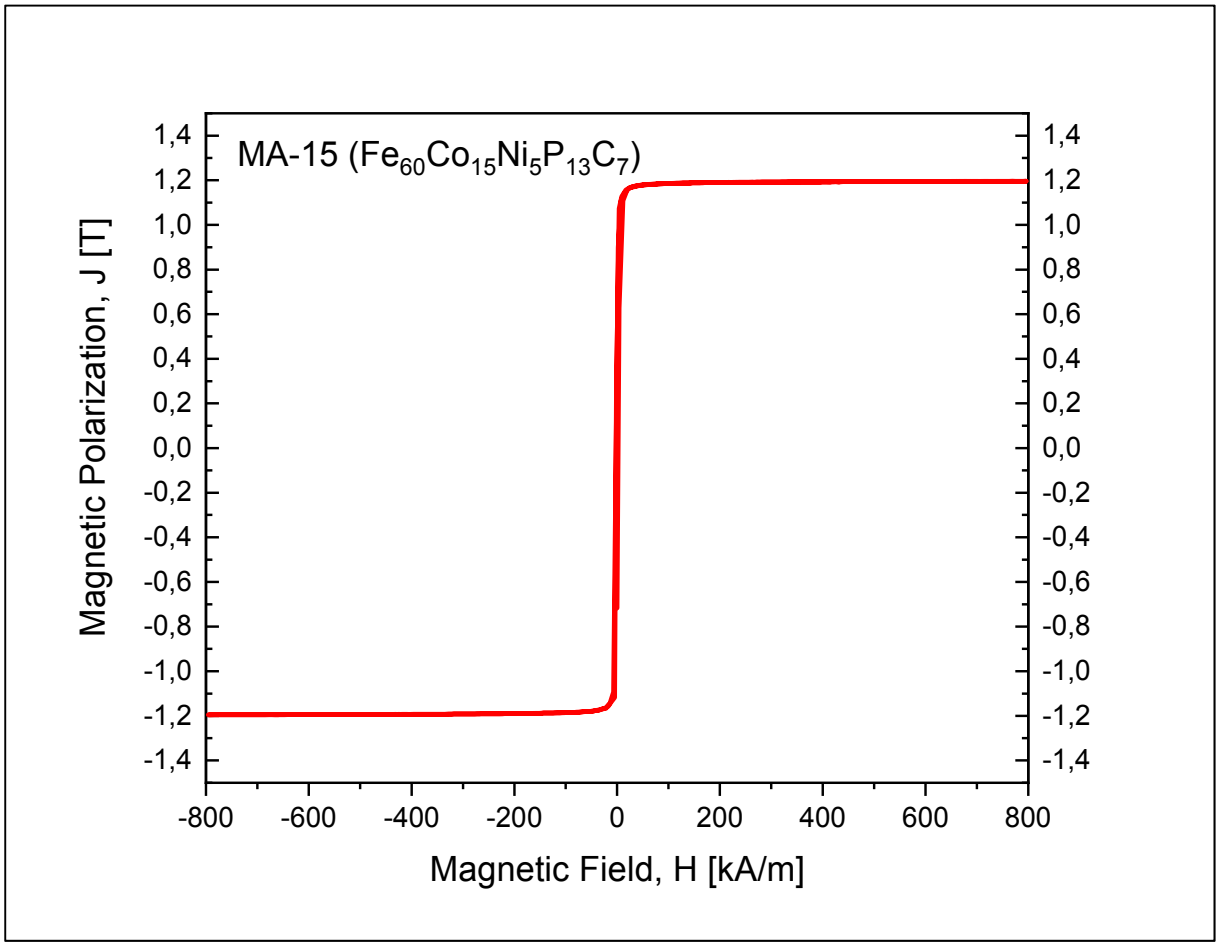

Figure 3.30: Hysteresis curve for as-cast MA-15 ($Fe_{60}Co_{15}Ni_5P_{13}C_7$) glassy ribbon.

This might be the explanation of the very broad crystallization event, which lasts at 865 K. However, considering the binary Fe-Co phase diagram at 20 at.% Co (1:4 atomic ratio of Co and Fe in the alloy), two endothermic peaks prior to melting event are too low to be either Curie temperature, or $\alpha \leftrightarrow \gamma$ transition of bcc α-(Fe,Co) solid solution. Nevertheless, it can be stated that they correspond to allotropic and/or magnetic transformation of the Fe-rich crystalline phases. The final crystallization products of this novel alloy also do not include any separate Fe_3C or Fe_3P phases like the case with $Fe_{60}Co_{20}P_{13}C_7$ and $Fe_{60}Ni_{10}Co_{10}P_{13}C_7$ glassy alloys. For a clear insight of the precipitated phases and their crystallization sequence, detailed TEM investigations are mandatory.

In Figure 3.30, the room temperature magnetic polarization of the as-cast MA-15 ($Fe_{60}Co_{15}Ni_5P_{13}C_7$) glassy ribbon under an applied field of 800 kA/m is depicted. This glassy ribbon exhibits a J_s of 1.19 T, which is significantly higher than that of $Fe_{60}Ni_{10}Co_{10}P_{13}C_7$ alloy. Apparently, this results from lower Ni content as well as from higher Co content of the new alloy.

As mentioned before, with $P_{13}C_7$ fixed amount of metalloid, Ni behaves paramagnetic because of the charge transfer from the metalloid atoms to its 3*d* band. Thus, upon any amount of Ni addition, mean magnetic moment of the alloy decreases as a result of decreasing total number of magnetic atoms in the alloy. On the other hand, 15 at.% Co replacement for Fe should have already made the alloy strongly ferromagnetic, which means that local magnetic moment at the Fe sites should be saturated and gained their maximum value. Once the alloy is magnetically strong, any ferromagnetic atom addition other than Fe causes a linear decrease in mean magnetic moment of the alloy, following the right-hand side of the well-known Slater-Pauling curve.

Meanwhile, charge transfer from metalloid atoms does not cause Co to behave paramagnetic, only lowers its magnetic moment (as they do to iron). Since Co is already a strongly ferromagnetic element, its lowered magnetic moment is insensitive to alloying with Fe and Ni. As a result, 15 at.% Co addition lowers the average magnetic moment of the alloy in a way which is smoother than Ni does.

Accordingly, J_s of the present alloy is higher than that of $Fe_{60}Ni_{10}Co_{10}P_{13}C_7$, but lower than that of $Fe_{80}P_{13}C_7$ and $Fe_{60}Co_{20}P_{13}C_7$ alloys. In addition, because of the higher Co content of the alloy, Curie temperature of the amorphous state seems to increase strongly and exceed the crystallization temperature, like the case in the $Fe_{60}Co_{20}P_{13}C_7$ glassy ribbon. This is an expected result considering the very high T_c of the $Fe_{60}Ni_{10}Co_{10}P_{13}C_7$ alloy (655 K).

3.8 MA-15-Fluxed ($Fe_{60}Co_{15}Ni_5P_{13}C_7$)

This ribbon was also cast at 1323 K as the unfluxed one. Even though they have been synthesized from the same master alloy and all other casting parameters are same, the fluxed ribbon exhibits some important differences not only in its thermal properties, but also in its crystallization behavior. In Figure 3.31, high temperature DSC trace of the as-cast MA-15-Fluxed ($Fe_{60}Co_{15}Ni_5P_{13}C_7$) glassy ribbon is shown.

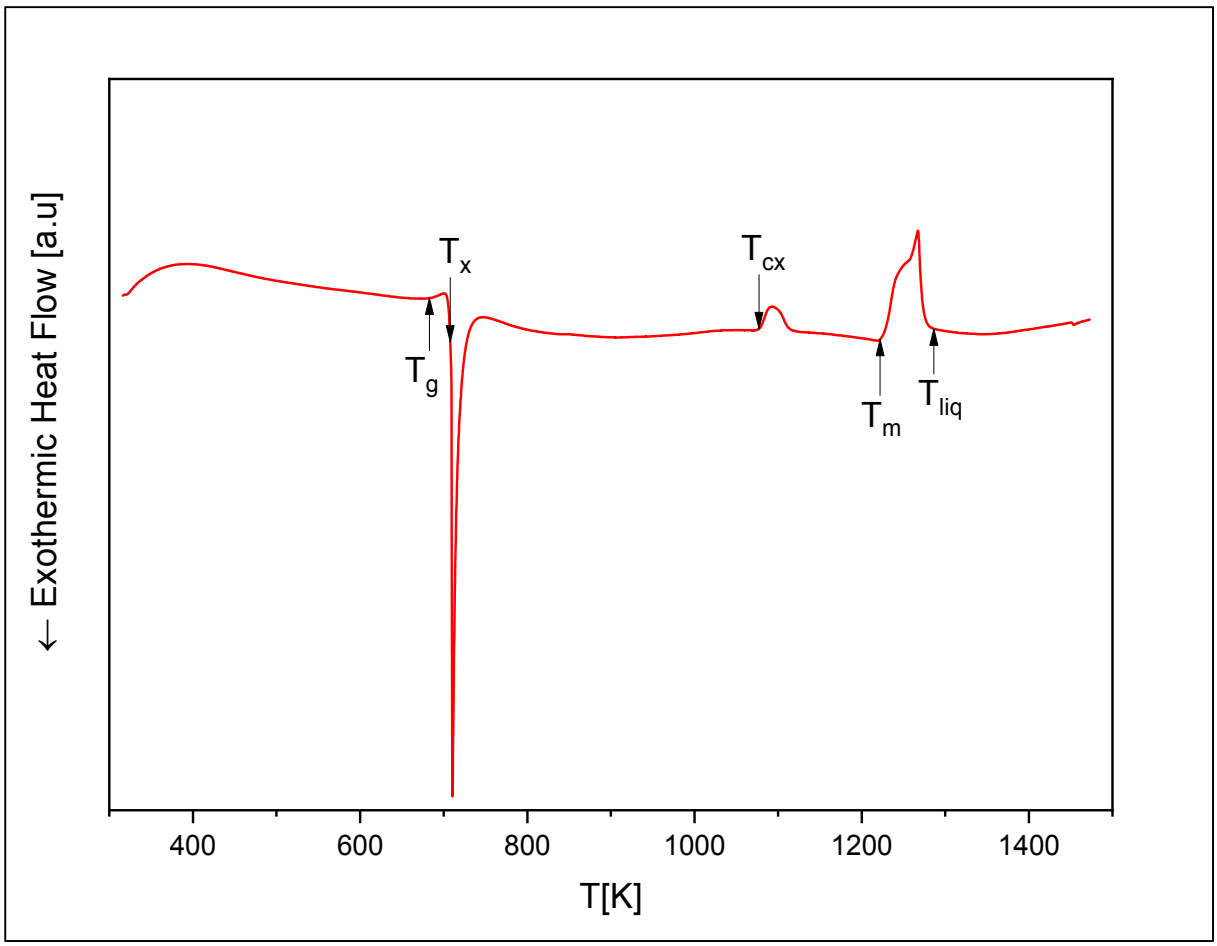

Figure 3.31: DSC trace of as-cast MA-15-Fluxed ($Fe_{60}Co_{15}Ni_5P_{13}C_7$) glassy ribbon.

Master Alloy	Composition	T_g [K]	T_x [K]	T_{liq} [K]	ΔT_x [K]	T_{rg} [K]
MA-15-Fluxed	$Fe_{60}Co_{15}Ni_5P_{13}C_7$	683	709	1286	26	0.531

Table 3.8: Glass transition, T_g, crystallization temperature T_x, liquidus temperature, T_{liq}, extension of the supercooled liquid region, ΔT_x, and reduced glass transition temperature, T_{rg} of the MA-15-Fluxed ($Fe_{60}Co_{15}Ni_5P_{13}C_7$) metallic glass ribbon.

As seen from the figure, this new alloy exhibits a clear glass transition temperature, a very sharp single exothermic peak, which indicates eutectic crystallization behavior of the alloy, and a Curie

temperature in the crystalline state. The melting behavior of the fluxed alloy seems to take place in a wider temperature range in comparison to the unfluxed alloy, and it is clearly off-eutectic, which is contrary to the unfluxed ribbon. Like the unfluxed alloy, this ribbon also shows no Curie temperature in the amorphous state.

Thermal properties of the sample, ΔT_x and T_{rg} parameters are presented in Table 3.8. One can see that after the fluxing treatment, in comparison to the unfluxed ribbon, the glass transition and the crystallization temperatures of the alloy are significantly increased. This is very unexpected, since in the case with unfluxed and fluxed $Fe_{80}P_{13}C_7$ ribbons (both were cast from same master alloy, MA-17), the magnitude of change in T_g was only 1 K and they have exhibited the same T_x of 703 K. However, this fluxed ribbon presents T_g and T_x values, which are both 21 K higher than those of unfluxed alloy. Further, T_{liq} of the present ribbon is also 18 K higher than that of unfluxed ribbon, and the magnitude of this difference was only 10 K between MA-17 ($Fe_{80}P_{13}C_7$) ribbons, and no change was observed in their crystallization behaviors.

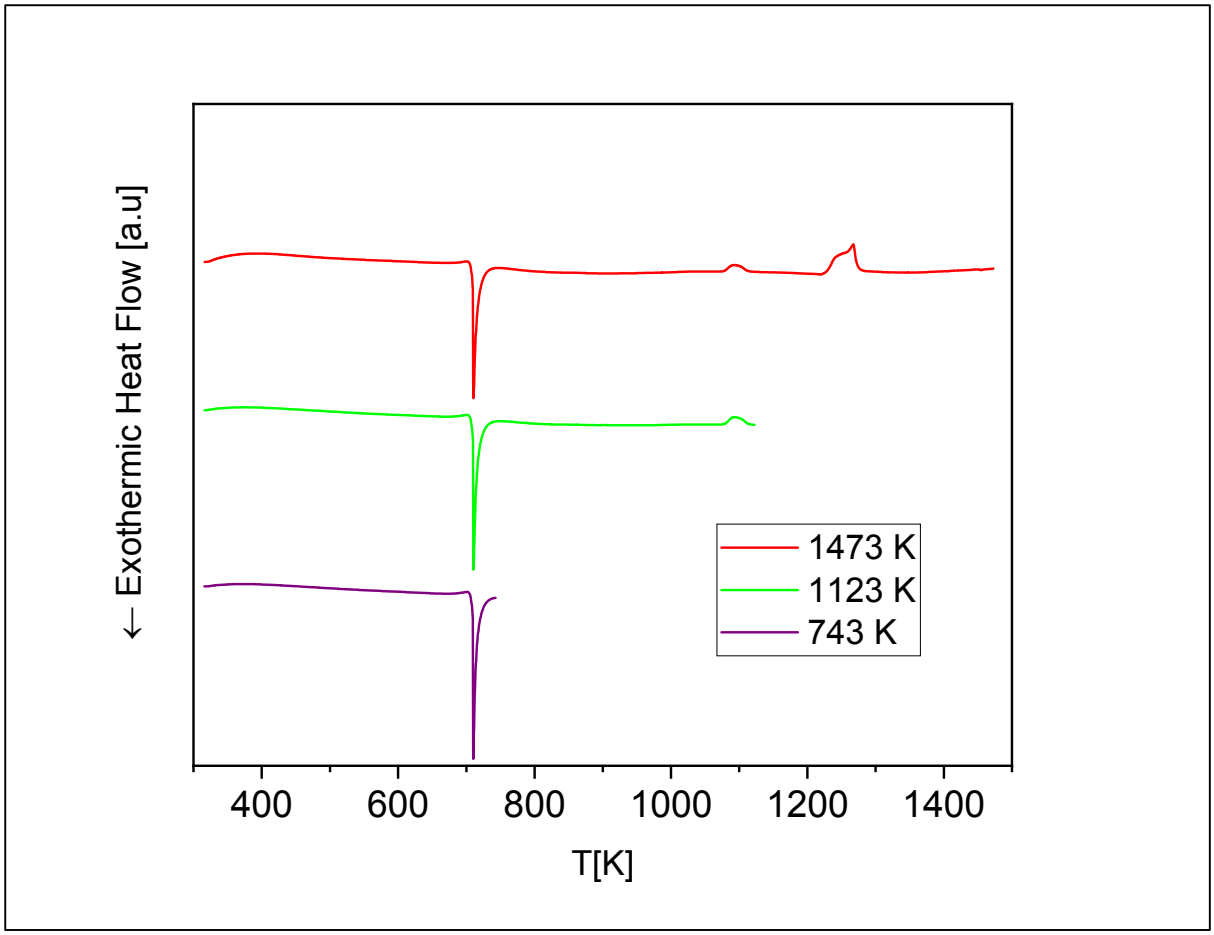

Figure 3.32: DSC traces of MA-15-Fluxed ($Fe_{60}Co_{15}Ni_5P_{13}C_7$) metallic glass ribbon, subjected to non-isothermal crystallization annealing at 20 K/min.

The reason of these major differences in T_g, T_x, T_{liq} and the different crystallization behavior of the fluxed sample has not been understood. It can only be concluded that, upon simultaneous substitution of Co and Ni for Fe, fluxing treatment may lead to major differences in crystallization behavior and characteristic temperatures, most likely resulting from the increased diversity in the formation of

possible SRO's in amorphous structure. On the other hand, ΔT_x parameter of the fluxed alloy is same as the unfluxed ribbon (26 K, widest of all ribbons), but T_{rg} is higher because of the strongly increased T_g. This fluxed ribbon exhibits the second highest T_{rg} value after MA-16 ($Fe_{60}Co_{20}P_{13}C_7$) ribbon and highest T_g among all ribbons. Considering these values (T_{rg} and ΔT_x), it can be stated that the fluxed ribbon has a high GFA in general, as the unfluxed ribbon of the same composition.

DSC traces of the non-isothermal crystallization annealing and the initial high temperature DSC curve of the MA-15-Fluxed ($Fe_{60}Co_{15}Ni_5P_{13}C_7$) metallic glass ribbon are shown in Figure 3.32. As the case with previous ribbons, these samples were subjected to XRD analysis and the resulting diffraction patterns along with the as-cast ribbons XRD pattern are depicted in Figure 3.33.

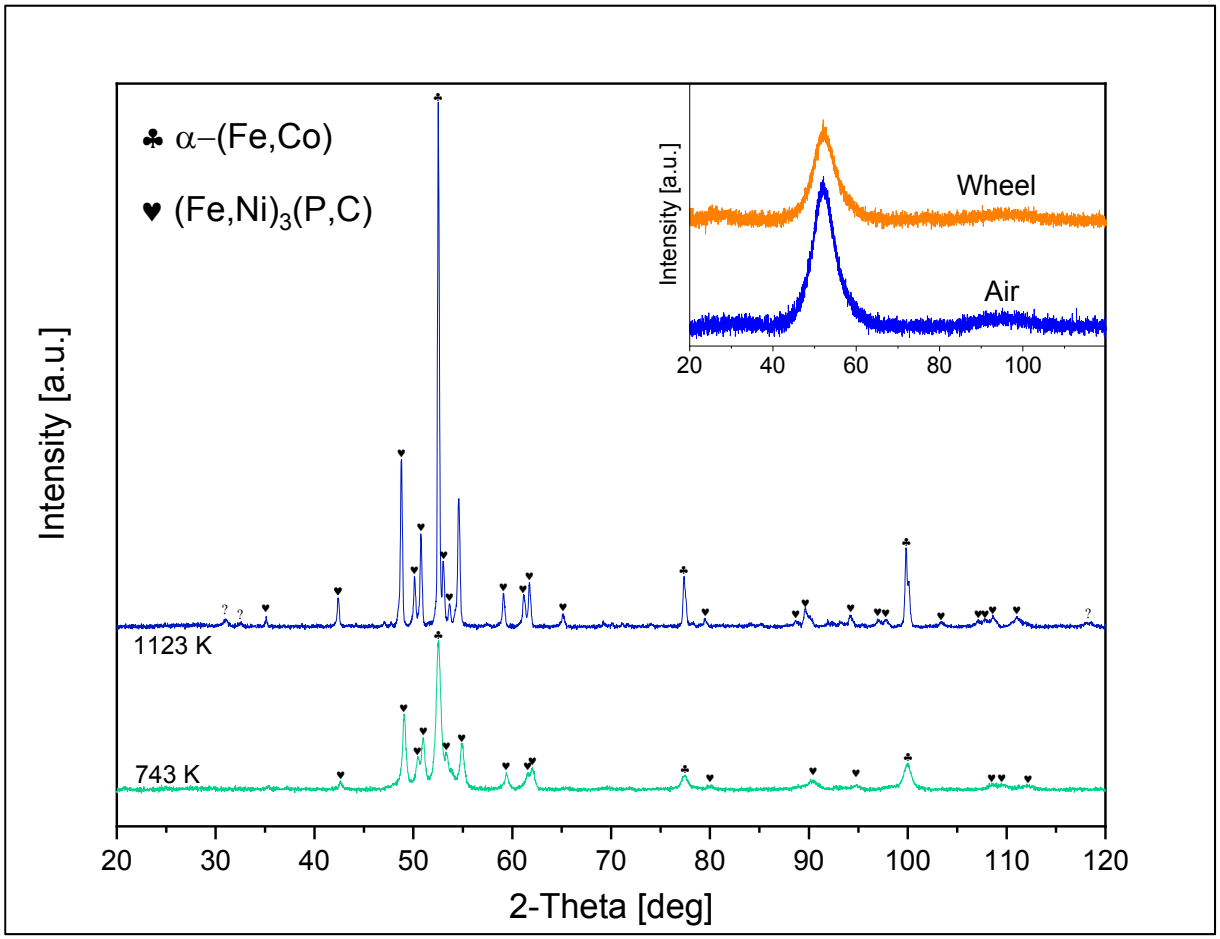

Figure 3.33: XRD patterns for MA-15-Fluxed ($Fe_{60}Co_{15}Ni_5P_{13}C_7$) glassy ribbon annealed up to different temperatures at 20 K/min and identified crystallization products. The inset shows the XRD pattern of the as-cast ribbon.

The sample heated up to 743 K (purple curve in Figure 3.32) exhibits $(Fe,Ni)_3(P,C)$ and α-(Fe,Co) crystalline phases. These phases are the same with those of the unfluxed alloy, which were crystallized at higher temperatures and first detected in sample heated up to 973 K. Apparently, fluxed alloy crystallizes in equilibrium phases faster and at lower temperatures. However, it can be seen that the fluxed alloy still presents some amount of amorphous matrix. It is important here to note that, even though the identified crystallization products are identical to those of the unfluxed ribbon, it has been found that the position of the diffraction peaks were shifted to higher 2-Theta angles about 0.7 degree.

This kind of a minor shift of the diffraction peaks between fluxed and unfluxed samples of $Fe_{50}Ni_{30}P_{13}C_7$ BMGs has been observed before [6], and it has been interpreted in terms of boron incorporation into the alloy during the fluxing treatment. Since the atomic radius of B is smaller than that of P and C, the authors concluded that the crystalline phases in the fluxed sample possess a more densely packed microstructure with a smaller mean atomic distance and larger coordination number, which in turn leads to higher 2-Theta angles according to well-known Bragg equation. Thus, this might also be the case with our fluxed samples, even though any B contribution could not be detected in the peak analysis of the diffraction patterns.

The next sample which was heated up to 1123 K (green DSC-trace in Figure 3.32) exhibits the same phases and seems to be completely crystallized. The onset temperature (1077 K) of the endothermic peak prior to melting event might correspond to the α ↔ γ transition of bcc α-(Fe,Co) solid solution and/or magnetic Curie transition temperature of this phase, even though this temperature is too low considering the binary Fe-Co phase diagram. However, the other alloy constituents (Ni, P, C) might have lowered the solid equilibrium temperature of α ↔ γ transition as well. Complimentary TEM experiments must be conducted in order to be able to correctly determine the crystallization products.

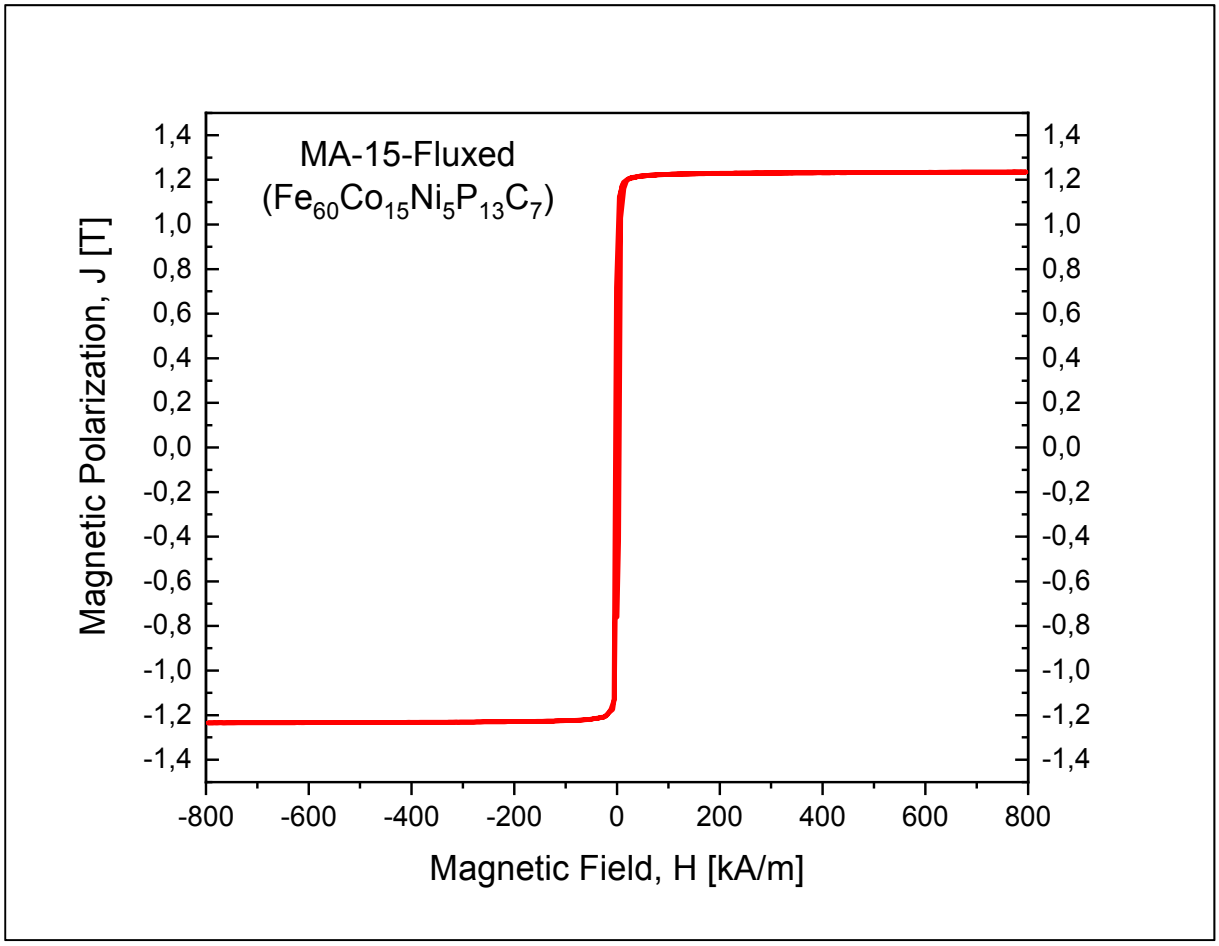

Figure 3.34: Hysteresis curve for as-cast MA-15-Fluxed ($Fe_{60}Co_{15}Ni_5P_{13}C_7$) glassy ribbon.

In Figure 3.34, the room temperature magnetic polarization of the as-cast MA-15-Fluxed ($Fe_{60}Co_{15}Ni_5P_{13}C_7$) glassy ribbon under an applied field of 800 kA/m is depicted. This glassy ribbon exhibits a J_s of 1.23 T, which is slightly higher than that of unfluxed alloy, and the highest J_s among

the new alloys. Apparently, for this alloy, fluxing treatment resulted in larger change on the room temperature saturation polarization, unlike the case in fluxed/unfluxed MA-17 ($Fe_{80}P_{13}C_7$) amorphous alloy. Further, Curie temperature in the amorphous state exceeds the crystallization temperature, irrespective of whether $Fe_{60}Co_{15}Ni_5P_{13}C_7$ alloy system is subjected to fluxing treatment or not.

Considering the $Fe_{60}Co_{15}Ni_5P_{13}C_7$ glassy alloy, it can be stated that fluxing purification changes mostly the thermal properties, rather than its room temperature saturation polarization. In the present alloy, fluxing treatment changes the crystallization behavior of the system and increases T_g (21 K), T_x (21 K) and T_{liq} (18 K) significantly. However, it increases the saturation ($J_{s\text{-Fluxed}}$ = 1.23 T, $J_{s\text{-Unfluxed}}$ = 1.19 T) of the system only slightly. On the other hand, in $Fe_{80}P_{13}C_7$ alloy, fluxing treatment changes neither the crystallization behavior nor T_g (the difference is only 1 K) and T_x of the system, but only increases T_{liq} (11 K). Moreover, J_s of the system exhibits almost no change ($J_{s\text{-Fluxed}}$ = 1.31 T, $J_{s\text{-Unfluxed}}$ = 1.30 T).

Therefore, it can be deduced that if the fluxing treatment results in a change in crystallization behavior of the system (i.e.; $Fe_{60}Co_{15}Ni_5P_{13}C_7$ and $Fe_{60}Ni_{20}P_{13}C_7$ amorphous alloys), its effect on J_s is also more prominent. This might be resulting from a stronger deviation in metalloid contents and an increased amount of B incorporation into the system. In both fluxed systems ($Fe_{60}Co_{15}Ni_5P_{13}C_7$ and $Fe_{60}Ni_{20}P_{13}C_7$), diffraction peaks of the crystalline phases have shifted to higher angles, however the magnitude of this shift is larger in $Fe_{60}Co_{15}Ni_5P_{13}C_7$ alloy. On the other hand, a significant increase in J_s (from 0.95 T to 1.12 T) has been observed in MA-11-Fluxed ($Fe_{60}Ni_{20}P_{13}C_7$) alloy. Since for the $Fe_{60}Ni_{20}P_{13}C_7$ system fluxed and unfluxed ribbons belong to different master alloys (MA-11 and MA-18), and also their casting parameters differ from each other, the sole effect of fluxing on J_s is not clear. However, for $Fe_{80}P_{13}C_7$ and $Fe_{60}Co_{15}Ni_5P_{13}C_7$ systems, it can be stated that if the fluxing purification has resulted in a change in the crystallization behavior and also a shift to higher angles in diffraction peaks (both of which the case with fluxed $Fe_{60}Co_{15}Ni_5P_{13}C_7$ alloy), a stronger increase in J_s can be observed.

3.9 MA-14 ($Fe_{60}Ni_{15}Co_5P_{13}C_7$)

This novel amorphous ribbon was cast at 1298 K. The details of its master alloy and other casting parameters can be found in Table 2.2. In Figure 3.35, high temperature DSC trace of the as-cast MA-14 ($Fe_{60}Ni_{15}Co_5P_{13}C_7$) glassy ribbon is presented.

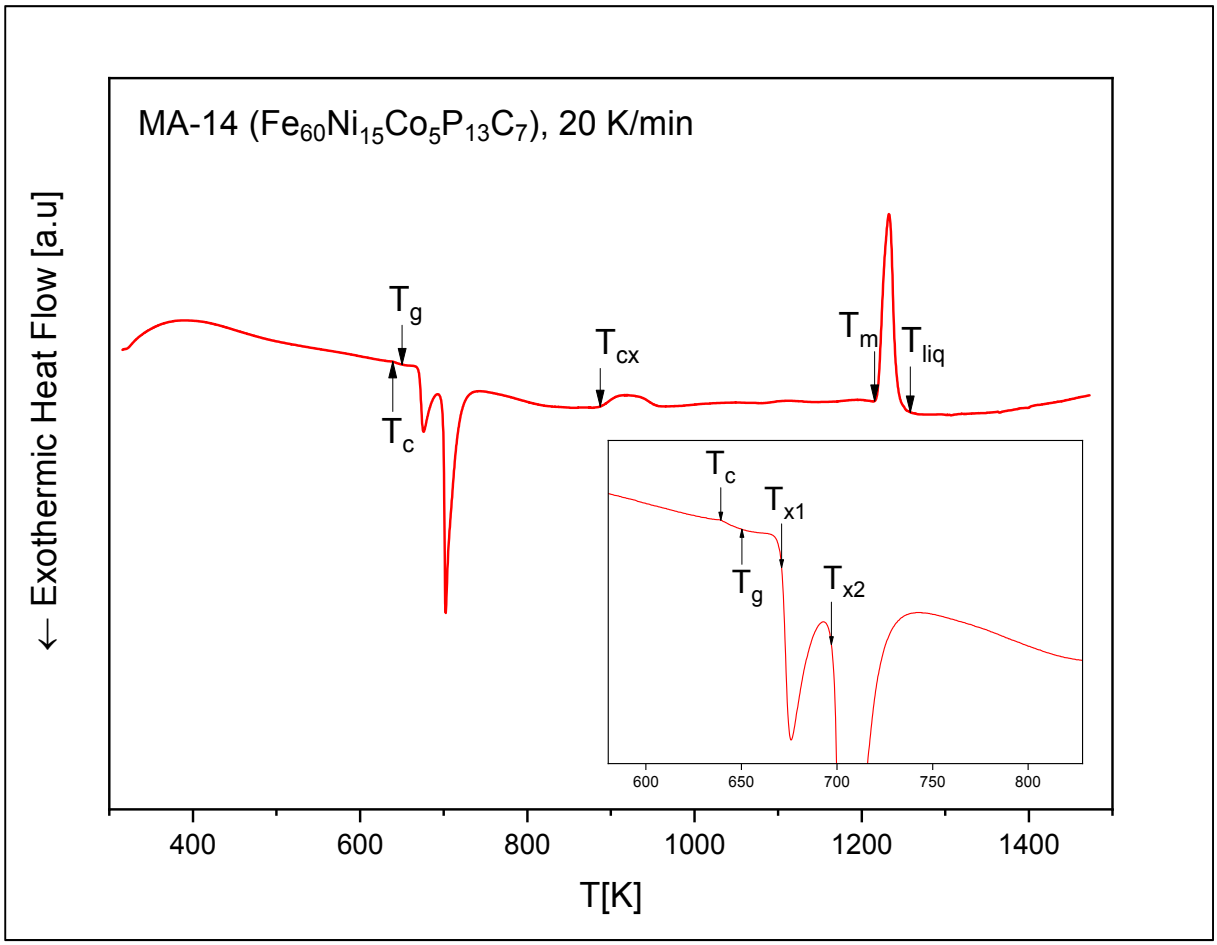

Figure 3.35: DSC trace of as-cast MA-14 ($Fe_{60}Ni_{15}Co_5P_{13}C_7$). The inset shows the enlarged region of the same curve.

Master Alloy	Composition	T_c [K]	T_g [K]	T_{x1} [K]	T_{x2} [K]	T_{liq} [K]	ΔT_x [K]	T_{rg}
MA-14	$Fe_{60}Ni_{15}Co_5P_{13}C_7$	639	650	671	697	1258	21	0.516

Table 3.9: Curie temperature, T_c, glass transition, T_g, crystallization temperatures T_{x1} and T_{x2}, liquidus temperature, T_{liq}, extension of the supercooled liquid region, ΔT_x, and reduced glass transition temperature, T_{rg} of the MA-14 ($Fe_{60}Ni_{15}Co_5P_{13}C_7$) metallic glass ribbon.

As seen from the figure, this new alloy shows a Curie temperature in its amorphous state, T_c, a glass transition temperature, T_g, a two-staged crystallization event, T_{x1} and T_{x2}, and a Curie temperature in the crystalline state, T_{cx}. Its melting behavior indicates that the alloy composition is close to the

eutectic point, like the other unfluxed alloys in which Ni and Co were substituted for Fe simultaneously (i.e.; $Fe_{60}Ni_{10}Co_{10}P_{13}C_7$ and $Fe_{60}Co_{15}Ni_5P_{13}C_7$).

In Table 3.9, thermal properties of the ribbon, ΔT_x and T_{rg} parameters are depicted. This new alloy exhibits the lowest T_g (650 K) and T_x (671 K) among all the fluxed/unfluxed ribbons. Considering the high Ni content of the alloy, strong depression of T_g and T_x was expected. Apparently, 5 at.% Co addition further decreases T_g and T_x. Meanwhile, T_{liq} of the new alloy is the lowest among those which Ni and Co were simultaneously replaced for Fe. Because of the stronger depression of T_{liq} in respect to T_g, the T_{rg} parameter of the present alloy is 0.516, which is also the lowest value among all the fluxed/unfluxed ribbons. Further, ΔT_x is determined as 21 K, that is, this new alloy exhibits the narrowest *SCLR* of all ribbons in this work.

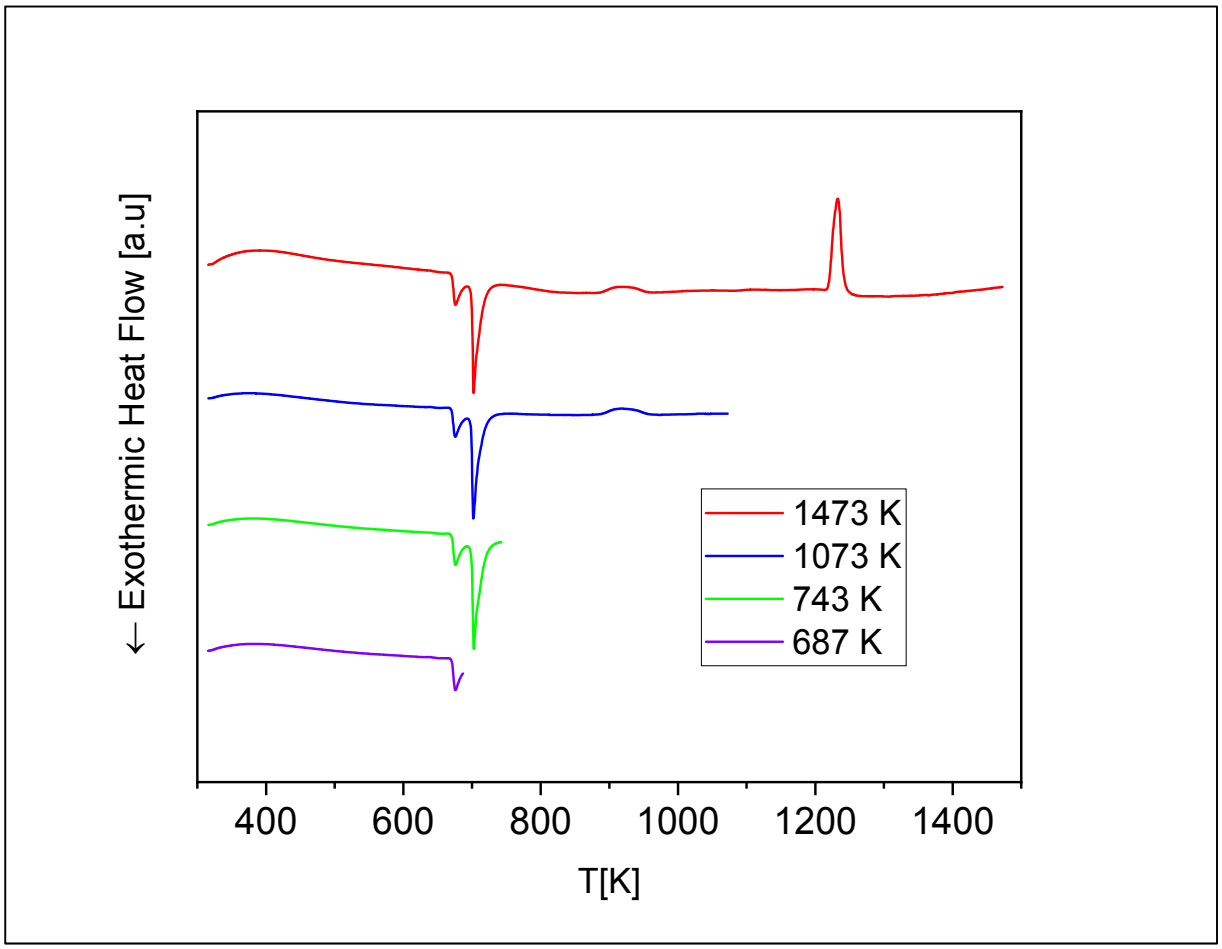

Figure 3.36: DSC traces of MA-14 ($Fe_{60}Ni_{15}Co_5P_{13}C_7$) metallic glass ribbon, subjected to non-isothermal crystallization annealing at 20 K/min.

Taking into account the ΔT_x and T_{rg} parameters, it can be stated that $Fe_{60}Ni_{15}Co_5P_{13}C_7$ amorphous alloy has the lowest GFA of all ribbons. However, it is important here to note that, the very first casting operation using this master alloy was successful, and no more attempts were made in order to see whether this alloy could be synthesized at higher casting temperatures or not. After this ribbon was successfully produced, a small piece (~5 g) of the master alloy was subjected to fluxing treatment.

Unfortunately, the casting operation using the fluxed master alloy has failed, and the remaining master alloy was not used any further, with the intention of preserving it for BMG casting trials in the future. Thus, it is not clear yet, whether this new alloy can easily be amorphized or not. DSC traces of the non-isothermal crystallization annealing and the initial high temperature DSC curve of the MA-14 ($Fe_{60}Ni_{15}Co_5P_{13}C_7$) metallic glass ribbon are shown in Figure 3.36. Like the other ribbons, these samples were subjected to XRD analysis and the obtained diffraction patterns along with the as-cast ribbons XRD pattern are presented in Figure 3.37.

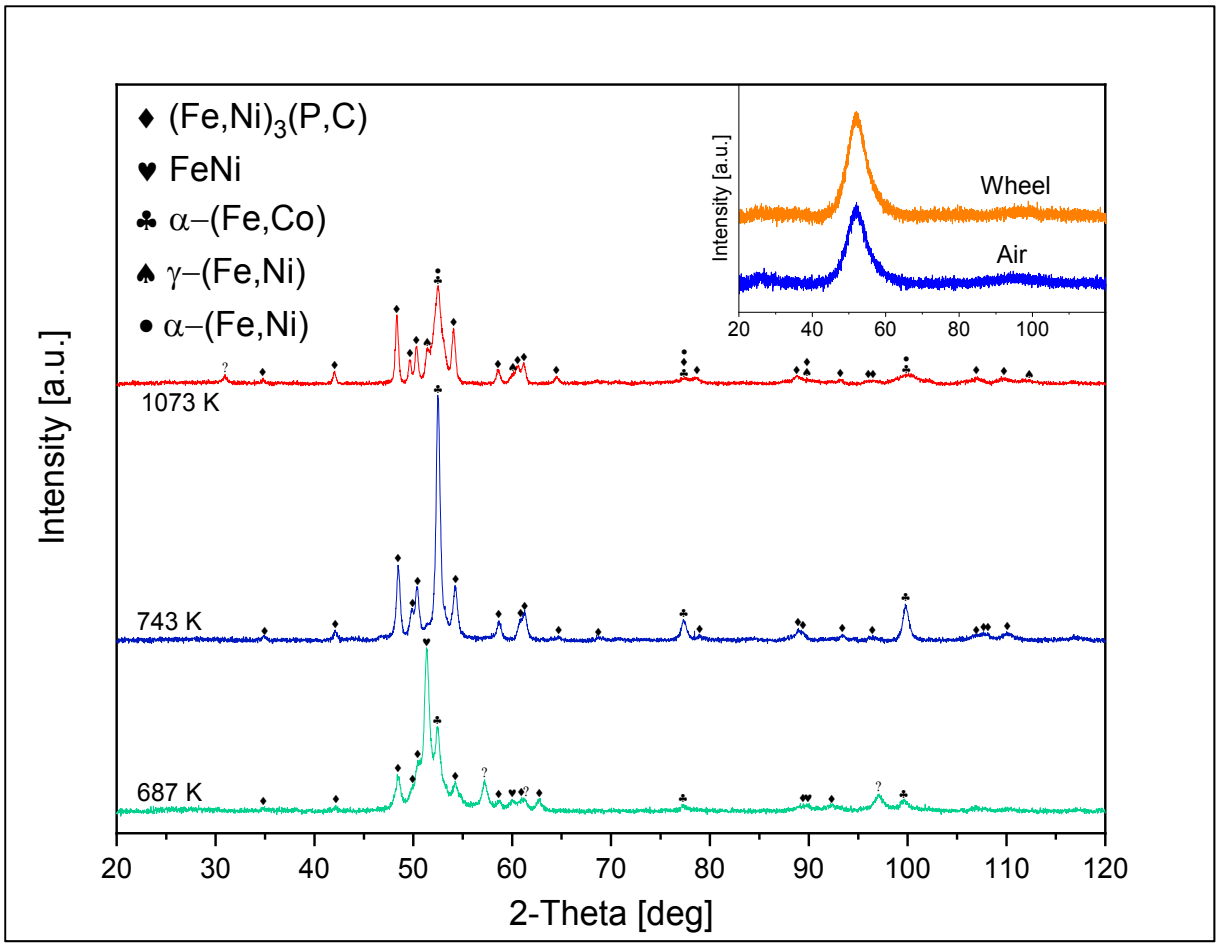

Figure 3.37: XRD patterns for MA-14 ($Fe_{60}Ni_{15}Co_5P_{13}C_7$) glassy ribbon annealed up to different temperatures at 20 K/min and identified crystallization products. The inset shows the XRD pattern of the as-cast ribbon.

As seen from the figure, the sample hated up to 687 K (purple DSC trace in Figure 3.36) exhibits stable tetragonal $(Fe,Ni)_3(P,C)$, stable bcc α-(Fe,Co) and metastable primitive tetragonal FeNi crystallization products. Additionally, there are two unidentified peaks which probably correspond to an unknown metastable phase. It seems like after the primary crystallization of FeNi, other phases have participated and the sample is still mostly amorphous.

The second sample was heated up to 743 K (green DSC curve in Figure 3.36) presents the same phases of $(Fe,Ni)_3(P,C)$ and α-(Fe,Co) as the previous sample. The metastable FeNi and unidentified metastable phase from the previous pattern disappeared at this temperature, and the sample looks almost fully crystallized. This is not surprising if one pays attention to the same level of the baselines in the DSC curve, before and after the crystallization events. In the XRD pattern of the sample all the

diffraction peaks are identified. At this temperature, it seems like all the Ni atoms reside in $(Fe,Ni)_3(P,C)$ phase and Co atoms are in bcc α-(Fe,Co) solid solution, since no Co atoms could be found in any other crystallization products according to peak analysis. Further, there are no separate Fe_3C, Fe_3P, Ni_3C or Co_3C phases to see, like the case with other new glassy alloys of FeNiCoPC system.

The last sample that was heated up to 1073 K (blue DSC trace in Figure 3.36), on the other hand, presents some unexpected phases while its XRD pattern looks peculiar. The intensity of the peaks which correspond to stable $(Fe,Ni)_3(P,C)$ phase remains mostly unchanged, but the intensities of α-(Fe,Co) peaks are greatly reduced and they are significantly broadened. This indicates that there should be two different α-Fe solid solutions at the room temperature, namely; α-(Fe,Co) and α-(Fe,Ni).

Similar to the case in MA-19 ($Fe_{60}Ni_{10}Co_{10}P_{13}C_7$) glassy ribbon, the remaining Ni atoms initially form α-(Fe,Ni) phase upon heating, and α-(Fe,Ni) ↔ γ-(Fe,Ni) martensitic transformation takes place at those temperatures which correspond to the onset and offset temperatures of the endothermic peak in the DSC trace. Later, upon cooling down to room temperature, γ-(Fe,Ni) phase undergoes a partial γ-(Fe,Ni) ↔ α-(Fe,Ni) martensitic transformation. As a result, two different α-(Fe,Co) and α-(Fe,Ni) phases with different lattice parameters might have given rise to broadened diffraction peaks in the XRD pattern of the sample.

In Figure 3.37, the room temperature magnetic polarization of the as-cast MA-14 ($Fe_{60}Ni_{15}Co_5P_{13}C_7$) glassy ribbon under an applied field of 800 kA/m is depicted. This glassy ribbon exhibits a J_s of 1.04 T.

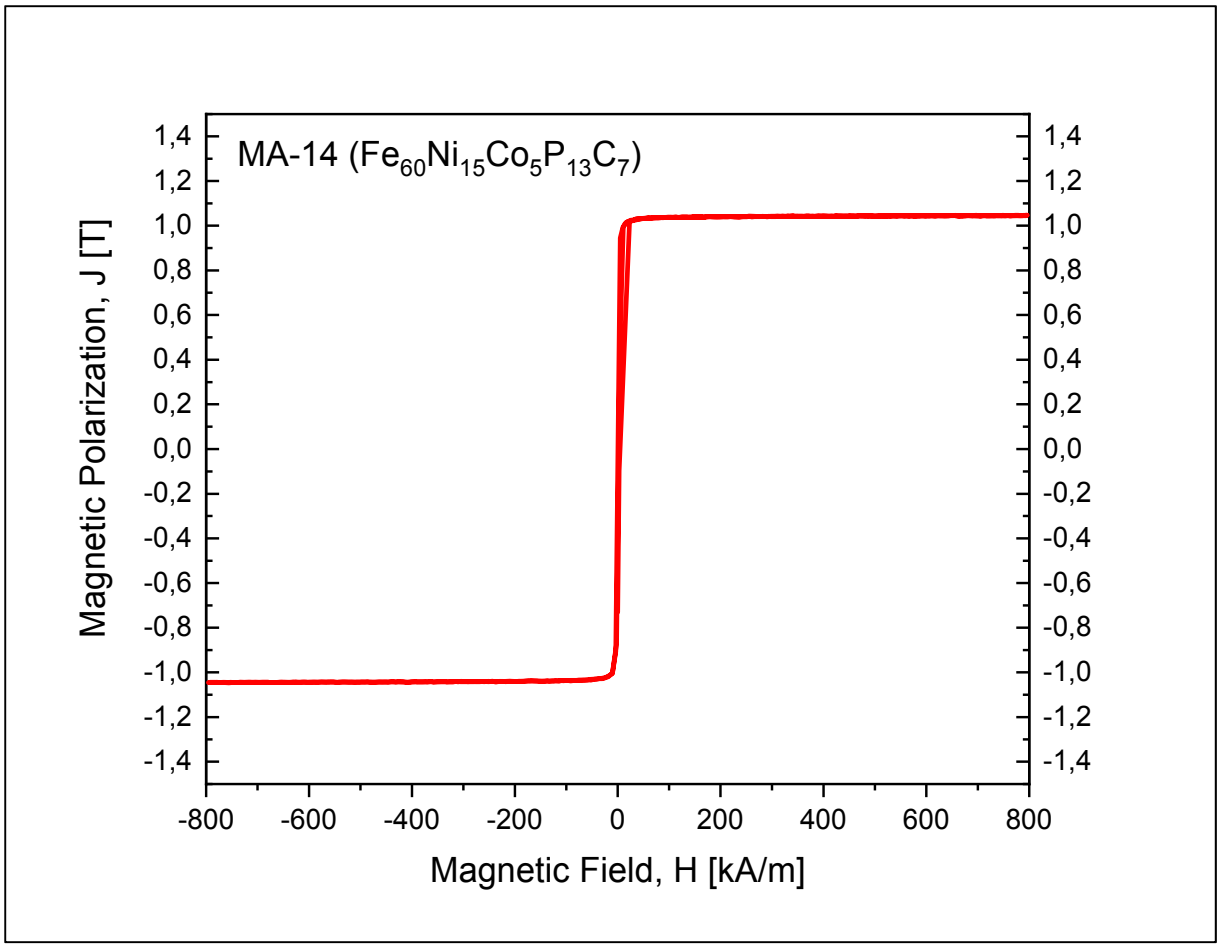

Figure 3.37: Hysteresis curve for as-cast MA-14 ($Fe_{60}Ni_{15}Co_5P_{13}C_7$) glassy ribbon.

Apparently, the simultaneous substitution of Ni and Co for Fe at 1:3 atomic ratio strongly reduces the J_s of the alloy in comparison to those of $Fe_{80}P_{13}C_7$, $Fe_{60}Co_{20}P_{13}C_7$, $Fe_{60}Co_{15}Ni_5P_{13}C_7$ and $Fe_{60}Co_{10}Ni_{10}P_{13}C_7$ unfluxed ribbons.

Actually, this new ribbon possesses the second lowest J_s value after the unfluxed $Fe_{60}Ni_{20}P_{13}C_7$ ribbon. This is not surprising, if one considers the second highest Ni amount in the alloy. It seems like the diluting effect of paramagnetic Ni overwhelms the positive effect of Co on J_s. This can be stated when the J_s values of unfluxed $Fe_{60}Ni_{20}P_{13}C_7$ (0.95 T) glassy ribbon and the present alloy are compared. Upon 5 at.% Co substitution for Ni gives rise to a significant increase in J_s of the new alloy.

However, it cannot be concluded the present alloy is strongly ferromagnetic, since 5 at.% Co addition seems to be too less to cause the exchange splitting, Δ, to become larger than E_0-E_F. Further, unlike Co, alloying with Ni continues to increase (even though it behaves like paramagnetic in $P_{13}C_7$ fixed metalloid content) the mean magnetic moment of Fe, until the equiatomic composition has been reached [72]. This results from the smaller exchange force of Fe-Ni atomic pair in comparison to the Fe-Co atomic pair. Considering the limited Co and Ni substitution, it is possible that the alloy is still weakly ferromagnetic.

Meanwhile, Curie temperature of the novel alloy in glassy state is 639 K. This is the second highest ascertained Curie temperature of the alloys in this work, following the T_c (655 K) of MA-19 ($Fe_{60}Ni_{10}Co_{10}P_{13}C_7$) amorphous ribbon. This is an expected result, if one again considers the lower exchange force of Fe-Ni atomic pair in comparison to the Fe-Co atomic pair. Since 5 at.% Ni

replacement for Co results in a decrease in total number of the Fe-Co pairs in the $Fe_{60}Ni_{10}Co_{10}P_{13}C_7$ alloy, T_c drops down accordingly. Moreover, it can be seen that, in the case of simultaneous substitution of Co and Ni for Fe, Co addition is more decisive than Ni addition. That is, if the Co amount in the alloy exceeds 10 at.% (i.e. fluxed/unfluxed $Fe_{60}Co_{15}Ni_5P_{13}C_7$ ribbons), it not possible to detect the T_c of the alloy from its DSC trace. On the other hand, for the present $Fe_{60}Ni_{15}Co_5P_{13}C_7$ and $Fe_{60}Ni_{10}Co_{10}P_{13}C_7$ alloys, T_c in the gassy state still can be detected, even though they are relatively close to the crystallization temperatures.

4. General Conclusion and Outlook

This study shows the changes in thermal, magnetic and structural properties of $Fe_{(80-x-y)}Ni_xCo_yP_{13}C_7$ (x = 0, 5, 10, 15, 20 at.%, y = 0, 5, 10, 15, 20 at.%, x + y = 20 or 0) melt-spun metallic glass ribbons upon alloying and implementing the fluxing purification technique. In the production of master alloys and the amorphous ribbons, low vacuum conditions were realized, and only commercial raw grade starting materials were used with the intention of reducing the long processing time of high vacuum conditions and the high production cost resulting from using high-purity starting materials. Main findings can be summarized below and in Table 4.1 as follows:

- In order to successfully produce ferromagnetic $Fe_{(80-x-y)}Ni_xCo_yP_{13}C_7$ glassy ribbons, the utilization of high purity starting materials is not obligatory, even under low vacuum conditions.

- Considering the thermal properties of fluxed and unfluxed melt-spun ribbons that have been synthesized from the same master alloys, fluxing treatment does not lead to a wider SCLR (ΔT_x), which is contrary to general expectation. Moreover, after fluxing treatment $Fe_{80}P_{13}C_7$ alloy exhibited a slightly narrower SCLR.

- Regarding the T_{rg} of the fluxed samples, an increase has been observed only for $Fe_{60}Co_{15}Ni_5P_{13}C_7$ glassy ribbon. But, because of the concurrent increase in T_g and T_x of the of the ribbon, SCLR value remained same as the unfluxed ribbon.

- The lack of any fluxing induced improvements on GFA of the samples might be related to the shortened fluxing time and/or to the difficulties of regulating the process temperature precisely.

- It has been found out that fluxing treatment resulted in a slight increase in J_s values of the samples. This finding confirms the assumption of phosphorus evaporation and/or decreasing carbon content and/or boron incorporation during the fluxing purification.

- If 20 at.% Ni is substituted for Fe, a strong depression of T_g, T_x and T_{liq} is observed for fluxed and unfluxed alloys. Moreover, upon Ni addition subsidiary crystallization peak diminished greatly and the melting behavior of the alloy became eutectic. Also, because of the paramagnetic behavior of Ni in $P_{13}C_7$ metalloid system, J_s of the ribbon decreases strongly. However, despite the lower T_c of Ni in the crystalline state, alloying it with Fe causes a clear increase in T_c in the amorphous state. This results from greater exchange force of Fe-Ni in comparison to Fe-Fe atomic pair and this effect is contrary to the crystalline bcc Fe-Ni alloys.

- Conversely, upon sole Co alloying, T_g and T_x are found to be very close to those of parent alloys, but a moderate decrease in T_{liq} is also observed. This gives rise to the highest T_{rg} of all ribbons for $Fe_{60}Co_{20}P_{13}C_7$ amorphous ribbon. The effect of 20 at.% Co addition on J_s is found to be detrimental, because of the weak to strong ferromagnetism transition. On the other hand, like the case in crystalline Fe-Co alloys, alloying Fe with Co increased the T_c of the glassy state significantly.

- Upon simultaneous addition of Co and Ni, the changes in T_g, T_x and ΔT_x do not follow any trend for $Fe_{60}Ni_{10}Co_{10}P_{13}C_7$ and $Fe_{60}Co_{15}Ni_5P_{13}C_7$ ribbons, but T_{rg} parameter decreases as the Ni content rises. On the other hand, $Fe_{60}Ni_{15}Co_5P_{13}C_7$ presents the lowest T_g, T_x, T_{rg} and ΔT_x of all ribbons. J_s and T_c of the alloys are found to be scaling according to the Co content in the alloys.

Master Alloy	T_c [K]	T_g [K]	T_x [K]	T_{rg}	ΔT_x [K]	T_{liq} [K]	J_s [T]
MA-17 ($Fe_{80}P_{13}C_7$)	591	678	703	0.527	25	1286	1.30
MA-18 ($Fe_{60}Ni_{20}P_{13}C_7$)	599	653	676	0.524	23	1245	0.95
MA-16 ($Fe_{60}Co_{20}P_{13}C_7$)	-	679	702	0.535	23	1268	1.29
MA-19 ($Fe_{60}Ni_{10}Co_{10}P_{13}C_7$)	655	665	689	0.526	24	1264	1.11
MA-15 ($Fe_{60}Co_{15}Ni_5P_{13}C_7$)	-	662	688	0.522	26	1268	1.19

MA-14 ($Fe_{60}Ni_{15}Co_5P_{13}C_7$)	639	650	671	0,516	21	1258	1.04
MA-15 ($Fe_{60}Co_{15}Ni_5P_{13}C_7$)	-	662	688	0.522	26	1268	1.19
MA-15-Fluxed ($Fe_{60}Co_{15}Ni_5P_{13}C_7$)	-	683	709	0,531	26	1286	1.23
MA-17 ($Fe_{80}P_{13}C_7$)	591	678	703	0.527	25	1286	1.30
MA-17-Fluxed ($Fe_{80}P_{13}C_7$)	590	679	703	0,523	24	1297	1.31
MA-18 ($Fe_{60}Ni_{20}P_{13}C_7$)	599	653	676	0.524	23	1245	0.95
MA-11-Fluxed ($Fe_{60}Ni_{20}P_{13}C_7$)	625	657	680	0,519	23	1264	1.12

Table 4.1: Thermal and magnetic properties of the investigated samples.

References

[1] C. Suryanayarana, A. Inoue, Bulk Metallic Glasses: Second Edition (2018)

[2] P. Ramasamy, Phd thesis: Soft Ferromagnetic Bulk Metallic Glasses with Enhanced Mechanical Properties (2017)

[3] M. Stoica, Fe-Based Bulk Metallic Glasses Understanding the Influence of Impurities on Glass Formation (2017)

[4] C. Suryanarayana, A. Inoue, Iron-based bulk metallic glasses, International Materials Reviews (2013)

[5] B. Sarac, Y.P. Ivanov, A. Chuvilin, Origin of large plasticity and multiscale effects in iron-based metallic glasses (2018)

[6] W. Yang, C. Wan, H. Liu, Fluxing induced boron alloying in Fe-based bulk metallic glasses (2017)

[7] K. Xu, H. Ling, Q. Li, Effects of Co substitution for Fe on the glass forming ability and properties of $Fe_{80}P_{13}C_7$ bulk metallic glasses (2014)

[8] C. Wan, W. Yang, H. Liu, Ductile Fe-based bulk metallic glasses at room temperature (2017)

[9] W. Yang, Q. Wang, H. Ling, Oxygen-driven impurities scavenging before solidification of Fe-based metallic glasses (2018)

[10] S.F. Guo, J.L. Qiu, P. Yu, Fe-based bulk metallic glasses: Brittle or ductile? (2014)

[11] Q. Li, J. Li, P. Gong, Formation of bulk magnetic ternary $Fe_{80}P_{13}C_7$ glassy alloy (2012)

[12] X. Ma, X. Yang, Q. Li, Quaternary magnetic FeNiPC bulk metallic glasses with large plasticity (2013)

[13] W. Yang, H. Liu, Y. Zhao, Mechanical properties and structural features of novel Fe-based bulk metallic glasses with unprecedented plasticity (2014)

[14] W. Yang, B. Sun, Y. Zhao, Non-repeatability of large plasticity for Fe-based bulk metallic glasses (2016)

[15] K. F. Yao, C. Q. Zhang, Fe-based bulk metallic glass with high plasticity (2007)

[16] T. Sato, T. Ichiyama, Crystallization of $Fe_{80}P_{13}C_7$ amorphous alloy powder (1990)

[17] G. N. Yang, S. Q. Chen, J. L. Gu, Serration behaviours in metallic glasses with different plasticity (2016)

[18] J. Zhou, W. Yang, C. Yuan, Ductile FeNi-based bulk metallic glasses with high strength and excellent soft magnetic properties (2018)

[19] A. Takeuchi, A. Inoue, Calculations of Mixing Enthalpy and Mismatch Entropy for Ternary Amorphous Alloys (2000)

[20] A. Takeuchi, A. Inoue, Classification of Bulk Metallic Glasses by Atomic Size Difference, Heat of Mixing and Period of Constituent Elements and Its Application to Characterization of the Main Alloying Element (2005)

[21] Z. Lu, H. Li, Z. Lei, The Effects of Metalloid Elements on the Nanocrystallization Behavior and Soft Magnetic Properties of FeCBSiPCu Amorphous Alloys (2018)

[22] D. Turnbull, Under what conditions can a glass be formed (1969)

[23] J.E. Shelby, Introduction to Introduction to glass science and technology: Second Edition (2005)

[24] W. Klement, R.H. Willens, P. Duwez, Non-crystalline structure in solidified gold–silicon alloys (1960)

[25] T.R. Anantharaman, C. Suryanarayana, Rapidly Solidified Metals: A Technological Overview (1987)

[26] E.H. Strange, C.A. Pim, Process of manufacturing thin sheets, foil, strips, or ribbons of Zinc, lead, or other metal or alloy (1908).

[27] C.H. Smith: 'Applications of rapidly solidified soft magnetic alloys', in 'Rapidly solidified alloys: processes, structures, properties, applications', (ed. H. H. Liebermann) (1993)

[28] P. Duwez, S.C.H. Lin, Amorphous Ferromagnetic Phase in Iron< Carbon< Phosphorus Alloys (1967)

[29] H.X. Li, Z.C. Lu, S.L. Wang, Fe-based bulk metallic glasses: Glass formation, fabrication, properties and applications (2019)

[30] K. Yamauchi, Y. Nakagawa, Amorphous ferromagnetic Fe-P-B alloys prepared by a new technique of splat cooling (1971)

[31] M. Kikuchi, H. Fujimori, Y. Obi, T. Masumoto, New amorphous ferromagnets with low coercive force (1976)

[32] A. Inoue, K. Kobayashi, T. Masumoto, Mechanical properties and thermal stability of (Fe Co, Ni)-Mo-C quaternary amorphous alloys (1980)

[33] A. Inoue, K. Kobayashi, J. Kanehira, Mechanical properties and thermal stability of (Fe Co, Ni)-MB (M = IV, V and VI group transition metals) amorphous alloys with low boron concentration (1980)

[34] W.H. Wang, C. Dong, C.H. Shek, Bulk metallic glasses (2004)

[35] A. Inoue, Stabilization of metallic supercooled liquid and bulk amorphous alloys (2000)

[36] A. Inoue, N. Nishiyama, T. Matsuda, Preparation of bulk glassy Pd40Ni10Cu30P20 alloy of 40 mm in diameter by water quenching (1996)

[37] A. Inoue, N. Nishiyama. H. Kimura, Preparation and thermal stability of bulk amorphous Pd40Cu30Ni10P20 alloy cylinder of 72 mm in diameter (1997)

[38] B. Shen, A. Inoue, Bulk Glassy Fe–Ga–P–C–B–Si Alloys with High Glass-Forming Ability, High Saturation Magnetization and Good Soft Magnetic Properties (2002)

[39] A. Inoue, J.S. Gook, Fe-based ferromagnetic glassy alloys with wide supercooled liquid region (1995)

[40] A. Inoue, Y. Shinohara, J.S. Gook, Thermal and magnetic properties of bulk Fe-based glassy alloys prepared by copper mold casting (1995)

[41] T.D. Shen, R.B. Schwarz, Bulk ferromagnetic glasses prepared by flux melting and water quenching (1999)

[42] W. Kauzmann, The nature of the glassy state and the behavior of liquids at low temperatures (1948)

[42] W.L. Johnson, Thermodynamic and kinetic aspects of the crystal to glass transformation in metallic materials (1986)

[43] L. Leuzzi, T.M. Nieuwenhuizen, Thermodynamics of the Glassy State (2008)

[44] D. Turnbull, Phase changes (1956)

[45] D.R. Gaskell, Introduction to the Thermodynamics of Materials, 5th edition (2008)

[46] R. DeHoff, Thermodynamics in Materials Science, 2nd edition (2006)

[47] A.L. Greer, Confusion by design (1993)

[48] M.H. Cohen, D. Turnbull, Molecular transport in liquids and glasses (1959)

[49] G. Adam, J.H. Gibbs, On the temperature dependence of cooperative relaxation properties in glass-forming liquids (1965)

[50] A. Inoue, Amorphous, nanoquasicrystalline and nanocrystalline alloys in Al-based systems (1998)

[51] S. Guo, L. Liu, N. Li, Fe-based bulk metallic glass matrix composite with large plasticity (2010)

[52] M. Stoica, Phd thesis: Casting and characterization of Fe-(Cr, Mo, Ga)-(P, C, B) soft magnetic bulk metallic glasses (2005)

[53] M.E. McHenry, Amorphous and nanocrystalline materials for applications as soft magnets (1999)

[54] R. Schwarz, T. Shen, U. Harms, Soft ferromagnetism in amorphous and nanocrystalline alloys (2004)

[55] A.I. Gubanov, Fizika Tverdego Tela (1960)

[56] F.E. Luborsky, Handbook of Ferromagnetic Materials - Amorphous Ferromagnets (1980)

[57] R. Hasegawa, Amorphous magnetic materials – a history (1991)

[58] C.C. Tsuei, P. Duwez, Metastable amorphous ferromagnetic phases in palladium-base alloys (1965)

[59] R. Hasegawa, Glassy Metals: magnetic, chemical, and structural properties (1983)

[60] T. Kaneyoshi, Amorphous Magnetism (1984)

[61] B.D. Cullity, C.D. Graham, Introduction to Magnetic Materials – Second Edition (2009)

[62] F.E. Luborsky, R.C. O'Handley, Amorphous Metallic Alloys – Fundamental Magnetic Properties (1983)

[63] Q. Liu, H. Liu, M. Wang, Effects of Ni substitution for Fe on magnetic properties of $Fe_{80-x}Ni_xP_{13}C_7$ (x =0–30) glassy ribbons (2017)

[64] W.D. Callister, D.G. Rethwisch, Materials Science and Engineering: An Introduction, Magnetic Properties (2010)

[65] H.Y. Jung, M. Stoica, S.Yi, Electrical and magnetic properties of Fe-based bulk metallic glass with minor Co and Ni addition (2014)

[66] C.W. Chen, Magnetism and Metallurgy of Soft Magnetic Materials (1977)

[67] Z.B. Jiao, H.X. Li, J.E. Gao, Effects of alloying elements on glass formation, mechanical and soft-magnetic properties of Fe-based metallic glasses (2011)

[68] R.C. O'Handley, R. Hasegawa, R. Ray, Ferromagnetic properties of some new metallic glasses (1976)

[69] T. Mizoguchi, Magnetism in amorphous alloys (1976)

[70] Y. Kakehashi, Modern Theory of Magnetism in Metals and Alloys (2012)

[71] S. Chikazumi, Physics of Ferromagnetism – Magnetism of amorphous materials (1997)

[72] R.C. O'Handley, D.S. Boudreaux, Magnetic Properties of Transition Metal-Metalloid Glasses (1978)

[73] J. Crangle, G.C. Hallam, The magnetization of face-centred cubic and body-centred cubic iron + nickel alloys (1963)

[74] W. Heisenberg: " Zur Theorie des Ferromagnetismus" ,1928

[75] H.S. Chen, Glassy Metals (1980)

[76] H.S. Chen, R. Sherwood, E. Gyorgy, The influence of composition and aging on the Curie temperature of metallic glasses (1977)

[77] R. Hasegawa, R. Ray, Iron< boron metallic glasses (1978)

[78] R.C. O'Handley, Physics of ferromagnetic amorphous alloys (1987)

[79] C.D. Graham, T. Egami, Magnetic properties of amorphous alloys (1978)

[80] R. Alben, J.J. Becker, M.C. Chi, Random anisotropy in amorphous ferromagnets (1978)

[81] M.H. Cohen, D. Turnbull, Composition Requirements for Glass Formation in Metallic and Ionic Systems (1961)

[82] C.C. Tsuei, G. Longworth, S.C.H. Lin, Temperature Dependence of the Magnetization of an Amorphous Ferromagnet (1968)

[83] P. Duwez, Structure and Properties of Alloys Rapidly Quenched from the Liquid State (1967)

[84] T. Egami, Magnetic amorphous alloys: physics and technological applications (1984)

[85] K. Yamauchi, T. Mizoguchi, The magnetic moments of amorphous metal-metalloid alloys (1975)

[86] D.E. Polk, The structure of glassy metallic alloys (1972)

[87] H. Fujimori, T. Masumoto, Y. Obi, On the magnetization process in an iron-phosphorus-carbon amorphous ferromagnet (1974)

[88] H. Chen, Thermodynamic considerations on the formation and stability of metallic glasses (1974)

[89] A. Drehman, A. Greer, D. Turnbull, Bulk formation of a metallic glass: $Pd_{40}Ni_{40}P_{20}$ (1982)

[90] H. Kui, A.L. Greer, D. Turnbull, Formation of bulk metallic glass by fluxing (1984)

[91] M. Volmer, A. Weber, Keimbildung in übersättigten Gebilden (1926)

[92] R. Becker, W. Doring, Kinetic treatment of the nucleation in supersaturated vapors (1954)

[93] D. Turnbull, J.C. Fisher, Rate of nucleation in condensed systems (1949)

[94] W. Kurz, D.J. Fischer, Fundamentals of Solidification (1992)

[95] G.S. Fulcher, Analysis of recent measurements of the viscosity of glasses (1925)

[96] M.H. Cohen, D. Turnbull, Molecular transport in liquids and glasses (1959)

[97] R.W. Cahn, H.H. Liebermann, Rapidly solidified alloys (1993)

[98] U. Köster, U. Herold, Crystallization of metallic glasses (1981)

[99] F.E. Luborsky, Perspective on application of amorphous alloys in magnetic devices (1977)

[100] K. Lu, Nanocrystalline metals crystallized from amorphous solids: nanocrystallization, structure, and properties (1996)

[101] J. Pan, Q. Chen, N. Li, Formation of centimeter Fe-based bulk metallic glasses in low vacuum environment (2008)

[102] C. Chang, J. Zhang, B. Shen, Pronounced enhancement of glass-forming ability of Fe–Si–B–P bulk metallic glass in oxygen atmosphere (2014)

[103] H.X. Li, J.E. Gao, Z.B. Jiao, Glass-forming ability enhanced by proper additions of oxygen in a Fe-based bulk metallic glass (2009)

[104] W-M. Wang, J.T. Zhang, A. Gebert, Casting vacuum effects on the precipitates and magnetic properties of Fe-based glassy alloys (2011)

[105] L.L. Meng, X.Y. Li, L. Wang, Casting Atmosphere Effects on the Precipitates, Magnetism, and Corrosion Resistance of $Fe_{78}Si_9B_{13}$ Glassy Alloys (2013)

[106] Y. Wang, K. Xu, Q. Li, Comparative study of non-isothermal crystallization kinetics between $Fe_{80}P_{13}C_7$ bulk metallic glass and melt-spun glassy ribbon (2012)

[107] W. Yang, J. Huo, H. Liu, Extraordinary magnetocaloric effect of Fe-based bulk glassy rods by combining fluxing treatment and J-quenching technique (2016)

[108] T. Wang, X. Yang, Q. Li, Effect of Cu and Nb additions on crystallization kinetics of $Fe_{80}P_{13}C_7$ bulk metallic glasses (2014)

[109] S. Meng, H. Ling, Q. Li, Development of Fe-based bulk metallic glasses with high saturation magnetization (2014)

[110] X. Yang, X. Ma, Q. Li, The effect of Mo on the glass forming ability, mechanical and magnetic properties of FePC ternary bulk metallic glasses (2013)

[111] J-F. Li, X. Liu, S-F. Zhao, Fe-based bulk amorphous alloys with iron contents as high as 82 at% (2015)

[112] Y. Wang, H. Zhai, Q. Li, Effect of Co substitution for Fe on the non-isothermal crystallization kinetics of $Fe_{80}P_{13}C_7$ bulk metallic glasses (2019)

[113] D.B. Miracle, The efficient cluster packing model – An atomic structural model for metallic glasses (2006)

[114] S.X. Zhou, B.S. Dong, J.Y. Qin, The relationship between the stability of glass-forming Fe-based liquid alloys and the metalloid-centered clusters (2012)

[115] M.G. Scott, P. Ramachandrarao, The Kinetics of Crystallisation of an Fe-P-C Glass (1977)

[116] J. Pang, A. Wang, S. Yue, Fluxing purification and its effect on magnetic properties of high-B_s FeBPSiC amorphous alloy (2017)

[117] M. Takahashi, T. Miyazaki, Magnetic Anisotropy in an Amorphous $Fe_{80}P_{13}C_7$ Alloy (1979)

[118] O, Kubaschewski, IRON-Binary Phase Diagrams (1982)

[119] H. Okamoto, The Fe-P (Iron-Phosphorus) System (1990)

[120] L.J. Swartzendruber, V.P. Itkin, C.B. Alcock, The Fe-Ni (Iron-Nickel) System (1991)

[121] F. Wang, A. Inoue, Y. Han, Excellent soft magnetic Fe-Co-B-based amorphous alloys with extremely high saturation magnetization above 1.85 T and low coercivity below 3 A/m (2017)

[122] F. Wang, A. Inoue, Y. Han, Soft magnetic Fe-Co-based amorphous alloys with extremely high saturation magnetization exceeding 1.9 T and low coercivity of 2 A/m (2017)

[123] B. Huang, Y. Yang, A.D. Wang, Saturated magnetization and glass forming ability of soft magnetic Fe-based metallic glasses (2017)

[124] H. Fujimori, M. Kikuchi, Y. Obi, New Co-Fe Amorphous Alloys as Soft Magnetic Materials (1976)

[125] Y-H. Zhou, M. Harmelin, J. Bigot, Martensitic Transformation in Ultrafine Fe-Ni Powders (1990)